Ph.D. Thesis

Study for the measurement of ϕ_3 using $B^0 \to DK^{*0}$ followed by $D \to K_S\pi^+\pi^-$ with model-independent Dalitz analysis
(ϕ_3 測定に向けたモデル依存の無い Dalitz 解析を用いた $B^0 \to DK^{*0}$, $D \to K_S\pi^+\pi^-$ 崩壊の研究)

東北大学理学研究科物理学専攻

根岸 健太郎

平成 26 年

Abstract

We report on a measurement of the CP violating angle ϕ_3 with $B^0 \to DK^{*0}(892)$ decays following $K^{*0}(892) \to K^+\pi^-$ and $D \to K^0_S\pi^+\pi^-$. In this mode, B flavor is tagged uniquely by $K^{*0}(892)$ decay, and angle ϕ_3 can be extracted from Dalitz plot analysis with model independent way. We use the full data sample of 772×10^6 $B\bar{B}$ pairs collected at the Upsilon(4S) resonance with the Belle detector at KEKB accelerator.

We report study of the ratio of amplitude of $B^0 \to D^0K^{*0}$ and $B^0 \to \bar{D}^0K^{*0}$, r_S. The decay $B^0 \to D^0K^{*0}$ has $b \to u$ transition, so it has ϕ_3 information. ϕ_3 precision can be scaled as $1/r_S$. This study set upper limit on r_S.

$$r_S \ < \ 0.87 \quad (\text{at } 68\ \%\ \text{C.L.}). \tag{1}$$

A new method, model-independent Dalitz analysis which enable us to avoid the modeling uncertainty on Dalitz plane is performed. This is first measurement of r_S on neutral B with model-independent Dalitz analysis.

Acknowledgment

My first and deepest thanks go to Hitoshi Yamamoto. He has been a remarkable teacher and a true friend.

Although my name alone appears on this thesis, the work it describes was a group effort. At the core were Tomoyuki Sanuki, Akimasa Ishikawa, Yoshiyuki Onuki and Jim Libby. Important contributions were made by Yasuyuki Horii, Tomonori Kusano, Kennosuke Itagaki, Yutaro Sato, Zenmei Suzuki, Tomoyuki Saito and Hiroshi Nakano. Working with this group of people has been a great pleasure.

Finally, I thank my parents for their encouragement and moral support all along the way.

Contents

1 Introduction **1**
- 1.1 KM Mechanism . . . 1
  - 1.1.1 CKM Matrix . . . 1
  - 1.1.2 Unitarity Triangle . . . 3
- 1.2 CP Asymmetry . . . 5
  - 1.2.1 $B^0 - \bar{B}^0$ Mixing . . . 5
  - 1.2.2 Branching Fraction B^0 and $\bar{B}^0$ . . . 6
  - 1.2.3 Direct CP Violation . . . 6
- 1.3 ϕ_3 Measurements . . . 7
  - 1.3.1 GLW Method . . . 7
  - 1.3.2 ADS Method . . . 9
  - 1.3.3 GGSZ Method . . . 10
  - 1.3.4 Dalitz Analysis . . . 11
  - 1.3.5 Model-independent Binned Analysis of Three-body D^0 Decays . . . 12

2 Experimental Apparatus and Analysis Tools **16**
- 2.1 KEKB Accelerator . . . 16
- 2.2 Belle Detector . . . 18
  - 2.2.1 Silicon Vertex Detector (SVD) . . . 18
  - 2.2.2 Central Drift Chamber (CDC) . . . 21
  - 2.2.3 Aerogel Cherenkov Counter (ACC) . . . 24
  - 2.2.4 Time-of-Flight Counter (TOF) . . . 24
  - 2.2.5 Electromagnetic Calorimeter (ECL) . . . 27
  - 2.2.6 K_L and Muon Detector (KLM) . . . 28
  - 2.2.7 Extreme Forward Calorimeter (EFC) . . . 28
  - 2.2.8 Trigger and Data Acquisition . . . 29
- 2.3 Particle Identification (PID) for $K^{\pm}/\pi^{\pm}$ . . . 31

3 Analysis **34**
- 3.1 Analysis Procedure . . . 34
- 3.2 Event Selection . . . 34
  - 3.2.1 Reconstruction of K^0_S Meson . . . 34
  - 3.2.2 Reconstruction of D Meson . . . 36
  - 3.2.3 Reconstruction of K^{*0} Meson . . . 37

3.2.4 Reconstruction of B^0 Meson . . . 38
3.2.5 Rejection of Backgrounds . . . 39
3.3 Discrimination of $q\bar{q}$ Background . . . 41
3.3.1 Introduction of Variables . . . 41
3.3.2 NeuroBayes Method . . . 42
3.3.3 Contribution of Each Variable . . . 42
3.3.4 $\mathcal{NB}^{\mathrm{TRANS}}$ . . . 45
3.4 Probability Density Function (PDF) . . . 45
3.4.1 PDF . . . 45
3.5 Signal Extraction Projected for All Dalitz Region . . . 48
3.6 (x, y) Fit on $D\pi$ Mode . . . 50
3.6.1 Fit Procedure to Obtain $(x_{\pm}, y_{\pm})$ . . . 50
3.6.2 Correction on N_i . . . 52
3.6.3 (x, y) Fit on $D\pi$ Real Data . . . 55
3.7 (x, y) Fit on DK^{*0} Pseudo-Experiments Sample . . . 65
3.7.1 Separate Fit . . . 65
3.7.2 Combined Fit . . . 65
3.8 Statistical Uncertainty . . . 65
3.8.1 Feldman-Cousin Method . . . 68

4 Result **75**
4.1 (x, y) Fit on DK^{*0} Real Data . . . 75
4.2 Systematic Uncertainty . . . 75
4.3 Physical Parameter Extraction . . . 83

5 Discussion **87**

6 Conclusion **88**

A Details on NeuroBayes Training $\mathcal{A}-1$

List of Figures

1.1 Unitarity triangle . . . 3
1.2 $B^0 \to \tilde{D}^0 K^{*0}$, $\tilde{D}^0 \to K^+K^-$ diagrams. . . . 7
1.3 Relation the amplitudes fo (1.53) and (1.54) . . . 8
1.4 $\bar{B}^0 \to \tilde{D}^0 \bar{K}^{*0}$, $\tilde{D}^0 \to K^\pm\pi^\mp$ diagrams. . . . 9
1.5 One of example of binning on Dalitz plane, eight binning. Binning index sign is flipped $m_+^2 = m_-^2$ reflection. . . . 11
1.6 Image of ϕ_3 effect on ($x_\pm$, $y_\pm$) Dalitz analysis observables. . . . 13

2.1 KEKB accelerator . . . 17
2.2 Belle Detector . . . 19
2.3 SVD1 . . . 20
2.4 SVD impact parameter resolution . . . 20
2.5 SVD2 . . . 21
2.6 CDC configuration . . . 22
2.7 CDC resolution . . . 23
2.8 dE/dx . . . 23
2.9 ACC configuration . . . 25
2.10 ACC pid . . . 25
2.11 TOF configuration . . . 26
2.12 TOF resolution and mass distribution . . . 26
2.13 ECL configuration . . . 27
2.14 ECL counter configuration . . . 28
2.15 KLM configuration . . . 29
2.16 KLM component . . . 30
2.17 Trigger configuration . . . 31
2.18 DAQ . . . 32
2.19 PID coverage . . . 32
2.20 PID and momentum . . . 33

3.1 The distributions of $M(K\pi)$ for signal MC. The lines correspond to the requirement. Blue filled histogram is fake D events. . . . 37
3.2 Significance of x of D mass selection for MC in signal region. Here signal region is defined by $|\Delta E| < 0.03$, $|m_{B^0} - M_{bc}| < 0.008$, $\mathcal{NB}^{\rm TRANS} > 5$. ($\Delta E$, $m_{\rm bc}$, $\mathcal{NB}^{\rm TRANS}$) are described below, and they are parameters to distinguish signal and backgrounds. . . . 37

3.3 The distributions of $M(K\pi)$ for signal MC. The lines correspond to the requirement. Blue filled histogram is fake K^{*0} events. 38
3.4 The distribution of $m_{\rm bc}$ and ΔE for signal MC. Blue filled histogram is fake B self cross-feed events. 39
3.5 The lines correspond to the requirement. 40
3.6 The distributions of ΔM for the signal (red), the $q\bar{q}$ background (blue, $q = c$ is yellow dashed and $q = u, d, s$ is magenta dashed) and the $B\bar{B}$ background (black). The histograms are obtained from MC. 40
3.7 The distributions of the variables used for the discrimination. We use red curve for the signal MC and blue curve for the $q\bar{q}$ background MC, which is divided into two components shown with yellow ($q = c$) and magenta ($q = u, d, s$). All the requirements except for the one on $\mathcal{NB}$ are applied before showing the plots. 43
3.8 The output and the performance of the NeuroBayes based on 12 parameters. 44
3.9 The distribution of $\mathcal{NB}^{\rm TRANS}$ for signal MC (red) and $q\bar{q}$ MC (blue). . . . 45
3.10 3D distribution projected for 2D (ΔE, $\mathcal{NB}^{\rm TRANS}$) (upper) and ($\mathcal{NB}^{\rm TRANS}$, $m_{\rm bc}$) (lower) for signal (left), $q\bar{q}$ background (center) and $B\bar{B}$ background (right). The correlation factors are listed at Table 3.3. 46
3.11 Signal PDF, projected for each parameter on fit region and signal region. . 48
3.12 $B\bar{B}$ real D PDF, projected for each parameter on fit region and signal region. 49
3.13 $B\bar{B}$ fake D PDF, projected for each parameter on fit region and signal region. 50
3.14 $q\bar{q}$ PDF, projected for each parameter on fit region and signal region. . . . 51
3.15 $D^0\rho^0$ PDF, projected for each parameter on fit region and signal region. . . 52
3.16 $D^0a_1^+$ PDF, projected for each parameter on fit region and signal region. . 53
3.17 3D-fit all dalitz region for real data, projected for each parameter (ΔE left, $\mathcal{NB}^{\rm TRANS}$ middle, $m_{\rm bc}$ right) in signal region. Red is signal. Dark blue is $B\bar{B}$ real D. Light blue is $B\bar{B}$ fake D. Magenta is $q\bar{q}$. Yellow is $D^0\rho^0$. Green is $D^0a_1^+$. 53
3.18 Efficiency for each bin $\bar{\epsilon}_i$. Blue line means average of all Dalitz region. Vertical error bars mean statistical uncertainty of CM sample. 54
3.19 $D\pi$ 3D-fit all dalitz region for real data, projected for each parameter (ΔE left, $\mathcal{NB}^{\rm TRANS}$ middle, $m_{\rm bc}$ right) in signal region. 56
3.20 Legend of Dalitz binning. We use almost the same manner on $D\pi$ and DK^{*0} modes except for $B^0 \leftrightarrow B^+$ and $\bar{B}^0 \leftrightarrow B^-$. 57
3.21 $D\pi$ 3D-fit each Dalitz bin region, projection for ΔE in signal region on B^-. Red is signal. Magenta is $q\bar{q}$. Yellow is $D^{*0}\pi^{\pm}$. Green is $D^{*\pm}\pi^{\mp}$. Blue is $B\bar{B}$. 58
3.22 $D\pi$ 3D-fit each Dalitz bin region, projection for ΔE in signal region on B^+. Red is signal. Magenta is $q\bar{q}$. Yellow is $D^{*0}\pi^{\pm}$. Green is $D^{*\pm}\pi^{\mp}$. Blue is $B\bar{B}$. 59
3.23 $D\pi$ 3D-fit each Dalitz bin region, projection for $m_{\rm bc}$ in signal region on B^-. Red is signal. Magenta is $q\bar{q}$. Yellow is $D^{*0}\pi^{\pm}$. Green is $D^{*\pm}\pi^{\mp}$. Blue is $B\bar{B}$. 60

3.24 $D\pi$ 3D-fit each Dalitz bin region, projection for $m_{\rm bc}$ in signal region on B^+. Red is signal. Magenta is $q\bar{q}$. Yellow is $D^{*0}\pi^{\pm}$. Green is $D^{*\pm}\pi^{\mp}$. Blue is $B\bar{B}$. 61
3.25 $D\pi$ 3D-fit each Dalitz bin region, projection for $\mathcal{NB}^{\rm TRANS}$ in signal region on B^-. Red is signal. Magenta is $q\bar{q}$. Yellow is $D^{*0}\pi^{\pm}$. Green is $D^{*\pm}\pi^{\mp}$. Blue is $B\bar{B}$. 62
3.26 $D\pi$ 3D-fit each Dalitz bin region, projection for $\mathcal{NB}^{\rm TRANS}$ in signal region on B^+. Red is signal. Magenta is $q\bar{q}$. Yellow is $D^{*0}\pi^{\pm}$. Green is $D^{*\pm}\pi^{\mp}$. Blue is $B\bar{B}$. 63
3.27 (x, y) fit on $D\pi$ 10000 pesudo-experiments mean and pull distributions. Left column are mean and right is pull distributions. Up to down, x_+, y_+, x_- and y_-. 66
3.28 (x, y) result (mean value only). error region are previous (x, y) statistical errors (1, 2, 3 σ). 67
3.29 Separate Fit on pseudo-experiments results at $\sum_i (N_i + \bar{N}_i) = 44.2$. Left column is mean distributions. Right is pull distributions. Up to down are x_+, y_+, x_- and y_-. 68
3.30 Separate Fit on pseudo-experiments results at $\sum_i (N_i + \bar{N}_i) = 1176.5$. Left column is mean distributions. Right is pull distributions. Up to down are x_+, y_+, x_- and y_-. 69
3.31 Combine fit on pseudo-experiments results at $\sum_i (N_i + \bar{N}_i) = 44.2$. Left column is mean distributions. Right is pull distributions. Up to down are x_+, y_+, x_- and y_-. 70
3.32 Combine fit on pseudo-experiments results at $\sum_i (N_i + \bar{N}_i) = 1176.5$. Left column is mean distributions. Right is pull distributions. Up to down are x_+, y_+, x_- and y_-. 71
3.33 $(x, y)_{\rm obt.}$ distributions (dot) and smoothed histogram PDF(solid lines (red, orange, green, blue, magenta : $\rho = 1, 0.5, 0.25, 0.01, 0.001$)) projected for x (left) and y (right). However $\rho < 0.5$ lines are overlapping because in those distributions ρ value is enough small at 0.5. In this study, smoothing parameter is selected by $(x, y)_{\rm obt.}$ RMS. Upper(lower) are $(x, y)_{\rm true}$ = (-0.4, 0.0)(0.3, 0.3). 72

4.1 3D fit with Dalitz binning $\bar{B}^0$ ΔE 76
4.2 DK^{*0} 3D-fit each Dalitz bin region, projection for ΔE in signal region on $\bar{B}^0$. Red is signal. Dark blue is $B\bar{B}$ real D. Light blue is $B\bar{B}$ fake D. Magenta is $q\bar{q}$. Yellow is $D^0\rho^0$. Green is $D^0 a_1^+$. 76
4.3 DK^{*0} 3D-fit each Dalitz bin region, projection for ΔE in signal region on B^0. Red is signal. Dark blue is $B\bar{B}$ real D. Light blue is $B\bar{B}$ fake D. Magenta is $q\bar{q}$. Yellow is $D^0\rho^0$. Green is $D^0 a_1^+$. 77
4.4 DK^{*0} 3D-fit each Dalitz bin region, projection for $m_{\rm bc}$ in signal region on $\bar{B}^0$. Red is signal. Dark blue is $B\bar{B}$ real D. Light blue is $B\bar{B}$ fake D. Magenta is $q\bar{q}$. Yellow is $D^0\rho^0$. Green is $D^0 a_1^+$. 78

4.5 DK^{*0} 3D-fit each Dalitz bin region, projection for $m_{\rm bc}$ in signal region on B^0. Red is signal. Dark blue is $B\bar{B}$ real D. Light blue is $B\bar{B}$ fake D. Magenta is $q\bar{q}$. Yellow is $D^0\rho^0$. Green is $D^0a_1^+$. 79
4.6 DK^{*0} 3D-fit each Dalitz bin region, projection for $\mathcal{NB}^{\rm TRANS}$ in signal region on $\bar{B}^0$. Red is signal. Dark blue is $B\bar{B}$ real D. Light blue is $B\bar{B}$ fake D. Magenta is $q\bar{q}$. Yellow is $D^0\rho^0$. Green is $D^0a_1^+$. 80
4.7 DK^{*0} 3D-fit each Dalitz bin region, projection for $\mathcal{NB}^{\rm TRANS}$ in signal region on B^0. Red is signal. Dark blue is $B\bar{B}$ real D. Light blue is $B\bar{B}$ fake D. Magenta is $q\bar{q}$. Yellow is $D^0\rho^0$. Green is $D^0a_1^+$. 81
4.10 Confidence level value on r_S. Red plots are B^0 (x_+, y_+). Blue plots are $\bar{B}^0$ (x_-, y_-). Black plots are combined. Horizontal black lines mean 38 % (according to 0.5 standard deviation), 68 % (1.0 σ), 86 % (1.5 σ), 95 % (2.0 σ). 86

A.1 The distributions of network output for signal MC (red) and for $q\bar{q}$ MC (black) are shown (upper). The purity is plotted over the network output (lower). For both, the figures given behind correspond to the output before the iteration training. . . . . $\mathcal{A}-2$
A.2 The correlation matrix of input variables. The column- and row- numbers are the node numbers. . . . . $\mathcal{A}-3$
A.3 The equalized distributions for the input variable (1st), the signal purity (2nd), the distributions after the preprocessing (3rd), and the purity curve on the efficiency (4th) for LR(KSFW). In the 1st and 3rd figures, the red corresponds to the signal while the black corresponds to the background. In the 4th figure, the red corresponds to the result after the training using all variables and the black corresponds to the one for single parameter. . . $\mathcal{A}-4$
A.4 The equalized distributions for the input variable (1st), the signal purity with a spline fit (2nd), the distributions after the preprocessing (3rd), and the purity curve on the efficiency (4th) for Cosine of $V_{\rm sig,1}$ and $V_{\rm oth.,1}$. In the 1st and 3rd figures, the red corresponds to the signal while the black corresponds to the background. In the 4th figure, the red corresponds to the result after the training using all variables and the black corresponds to the one for single parameter. . . . . $\mathcal{A}-5$
A.5 The equalized distributions for the input variable (1st), the signal purity with a spline fit (2nd), the distributions after the preprocessing (3rd), and the purity curve on the efficiency (4th) for Δz. In the 1st and 3rd figures, the red corresponds to the signal while the black corresponds to the background. In the 4th figure, the red corresponds to the result after the training using all variables and the black corresponds to the one for single parameter. We use a delta-function for the case that the tag-side vertex cannot be obtained. . . . . $\mathcal{A}-6$

A.6 The equalized distributions for the input variable (1st), the signal purity with a spline fit (2nd), the distributions after the preprocessing (3rd), and the purity curve on the efficiency (4th) for Distance of D and K^{*0}. In the 1st and 3rd figures, the red corresponds to the signal while the black corresponds to the background. In the 4th figure, the red corresponds to the result after the training using all variables and the black corresponds to the one for single parameter. . . . . $\mathcal{A}-7$
A.7 The equalized distributions for the input variable (1st), the signal purity with a spline fit (2nd), the distributions after the preprocessing (3rd), and the purity curve on the efficiency (4th) for $|qr|$. In the 1st and 3rd figures, the red corresponds to the signal while the black corresponds to the background. In the 4th figure, the red corresponds to the result after the training using all variables and the black corresponds to the one for single parameter. . . . . $\mathcal{A}-8$
A.8 The equalized distributions for the input variable (1st), the signal purity with a spline fit (2nd), the distributions after the preprocessing (3rd), and the purity curve on the efficiency (4th) for $|\cos\theta_B|$. In the 1st and 3rd figures, the red corresponds to the signal while the black corresponds to the background. In the 4th figure, the red corresponds to the result after the training using all variables and the black corresponds to the one for single parameter. . . . . $\mathcal{A}-9$
A.9 The equalized distributions for the input variable (1st), the signal purity with a spline fit (2nd), the distributions after the preprocessing (3rd), and the purity curve on the efficiency (4th) for $\cos\theta_{\mathrm{thu}}$. In the 1st and 3rd figures, the red corresponds to the signal while the black corresponds to the background. In the 4th figure, the red corresponds to the result after the training using all variables and the black corresponds to the one for single parameter. . . . . $\mathcal{A}-10$
A.10 The equalized distributions for the input variable (1st), the signal purity with a spline fit (2nd), the distributions after the preprocessing (3rd), and the purity curve on the efficiency (4th) for $\cos\theta_B^D$. In the 1st and 3rd figures, the red corresponds to the signal while the black corresponds to the background. In the 4th figure, the red corresponds to the result after the training using all variables and the black corresponds to the one for single parameter. . . . . $\mathcal{A}-11$
A.11 The equalized distributions for the input variable (1st), the signal purity with a spline fit (2nd), the distributions after the preprocessing (3rd), and the purity curve on the efficiency (4th) for Cosine of $V_{\mathrm{sig},3}$ and $V_{\mathrm{oth.},3}$. In the 1st and 3rd figures, the red corresponds to the signal while the black corresponds to the background. In the 4th figure, the red corresponds to the result after the training using all variables and the black corresponds to the one for single parameter. . . . . $\mathcal{A}-12$

A.12 The equalized distributions for the input variable (1st), the signal purity with a spline fit (2nd), the distributions after the preprocessing (3rd), and the purity curve on the efficiency (4th) for Cosine of $V_{\mathrm{sig},2}$ and $V_{\mathrm{oth.},2}$. In the 1st and 3rd figures, the red corresponds to the signal while the black corresponds to the background. In the 4th figure, the red corresponds to the result after the training using all variables and the black corresponds to the one for single parameter. . . . . $\mathcal{A}-13$
A.13 The equalized distributions for the input variable (1st), the signal purity with a spline fit (2nd), the distributions after the preprocessing (3rd), and the purity curve on the efficiency (4th) for Z of $V_{\mathrm{all},1}$. In the 1st and 3rd figures, the red corresponds to the signal while the black corresponds to the background. In the 4th figure, the red corresponds to the result after the training using all variables and the black corresponds to the one for single parameter. . . . . $\mathcal{A}-14$
A.14 The equalized distributions for the input variable (1st), the signal purity with a spline fit (2nd), the distributions after the preprocessing (3rd), and the purity curve on the efficiency (4th) for Magnitude of Thrust_oth. In the 1st and 3rd figures, the red corresponds to the signal while the black corresponds to the background. In the 4th figure, the red corresponds to the result after the training using all variables and the black corresponds to the one for single parameter. . . . . $\mathcal{A}-15$

List of Tables

2.1 Various e^+e^- process at $\sqrt{s} = 10.58$ GeV cross-section. 17

3.1 The flowchart of this study. 35
3.2 The power of individual parameters. 44
3.3 Correlation factor. 46
3.4 PDF. 47
3.5 The list of values of component yield for the fit on data. 49
3.6 Cross-feed matrix α_{ik} (values in per cent). 55
3.7 Comparison of (x, y) of $D\pi$ result 64

4.1 Systematic uncertainties in the (x, y) measurement for $B^0 \to DK^{*0}$ mode. 82
4.2 Result of $(x_\pm, y_\pm)$. 83

A.1 The rank in importance for network output (rank), the identification number of the input (node), the name of variable (name), and the preprocessing flag (preprocess) are listed. . . . . $\mathcal{A}-16$

Chapter 1

Introduction

In early universe, antimatter should have been produced in the same quantity as matter. However, in the current universe, almost everything is constructed from matter rather than antimatter. There is few antimatter than matter. We cannot explain this asymmetry, despite the standard model (SM) has been verified by many experiments. With CP-violation (CPV), we can explain the asymmetry of matter and antimatter. CPV will be one of the answer for disappearance of antimatter. Cabibbo-Kobayashi-Maskawa (CKM) mechanism was proposed by Cabibbo, Kobayashi and Maskawa. It suggests that CPV is possible if quarks have three generations.

In SM, there are many parameters that should be measured by experiments, for example particle mass, mixing angle and so on. Flavor physics aspires to measurements of those parameters and searching new physics. Measurements of flavor mixing parameters it's origin in particle mass, are important step toward answer for essential question including CPV. If we obtain result inconsistent with SM, it is a clue about the beyond SM.

In this chapter, we introduce the CKM mechanism and the methods for measuring ϕ_3. In Chapter 2, we describe the experimental apparatus and analysis tools. In Chapter 3, we show the analytical procedure, the event selection and the signal extraction, measurements of observables relative to ϕ_3, control sample study, pseudo experiments toy MC study and so on. In Chapter 4, we summarize the result of this study. In Chapter 5, we discuss about this study.

1.1 KM Mechanism

1.1.1 CKM Matrix

CPV is derived from mixing of three generation quarks in a spontaneous way [1, 2]. In SM, weak interference mediated by W boson is described by following Lagrangian.

$$\mathcal{L}_{\rm int}(x) = -\frac{g}{\sqrt{2}}(\overline{U}_L\gamma_\mu D_L W^+_\mu + \overline{D}_L\gamma_\mu U_L W^-_\mu), \tag{1.1}$$

where g is a coupling constant, U_L, D_L are status of quark flavor as

$$U = \begin{pmatrix} u \\ c \\ t \end{pmatrix}, D = \begin{pmatrix} d \\ s \\ b \end{pmatrix}. \tag{1.2}$$

Subscript L means left handed. Mass eigenstates of quarks U'_L and D'_L are obtained from (1.2) with conversion of unitary matrix S^u and S^d.

$$U_L = S^u U'_L \tag{1.3}$$
$$D_L = S^d D'_L \tag{1.4}$$

(1.1) can be written as

$$\begin{aligned} \mathcal{L}_{\text{int}}(x) &= -\frac{g}{\sqrt{2}}(\overline{U'}_L S^{u\dagger}\gamma_\mu S^d D'_L W^+_\mu + \overline{D'}_L S^{d\dagger}\gamma_\mu U'_L S^u W^-_\mu) \\ &= -\frac{g}{\sqrt{2}}(\overline{U'}_L V_{CKM}\gamma_\mu D'_L W^+_\mu + \overline{D'}_L V^\dagger_{CKM}\gamma_\mu U'_L W^-_\mu). \end{aligned} \tag{1.5}$$

Where

$$V_{CKM} = S^{u\dagger} S^d. \tag{1.6}$$

V_{CKM} is called CKM matrix, and its components represents coupling constant for quark transition.

$$V_{CKM} = \begin{pmatrix} V_{ud} & V_{us} & V_{ub} \\ V_{cd} & V_{cs} & V_{cb} \\ V_{td} & V_{ts} & V_{tb} \end{pmatrix} \tag{1.7}$$

From (1.6) and unitarity of S^u and S^d, V_{CKM} is unitary.

We confirm appearance of CPV phase in CKM matrix if quarks have 3 generations. In general, degree of freedom of $n \times n$ complex matrix are $2n^2$. The unitarity of V_{CKM} reduces n^2 of those, and we also have to consider the phases of the quarks. Since the phases of quarks do not have effects on the physics, we can suppress some degrees of freedom using the phase transitions. However, the same phase changes for all quarks do not vary the matrix V_{CKM}. So we reject $2n-1$ at total by phase transitions of quarks. Therefore, we get the number of degrees of freedom as

$$2n^2 - n^2 - (2n-1) = (n-1)^2 \tag{1.8}$$

In additional, possible complex phases in V_{CKM} is then obtained as follows: Considering the case without complex components, the unitary condition of V_{CKM} is equivalent to the orthogonal conditions,

$$\sum_j V_{CKM,ij} V_{CKM,kj} = \delta_{ik} \qquad (i \leq k) \tag{1.9}$$

The number of degrees of freedom of real components are then $n^2 - \dfrac{(n+1)n}{2} = \dfrac{n(n-1)}{2}$. Finally, n generation CKM matrix V_{CKM} have

$$(n-1)^2 - \frac{n(n-1)}{2} = \frac{(n-1)(n-2)}{2} \tag{1.10}$$

degree of freedom. If $n \leq 2$, all CKM matrix components can be described by real number. To appear the complex component in CKM matrix violating CP phase, larger than three generation quark is needed.

1.1.2 Unitarity Triangle

CKM matrix is described as follows with quark mixing angles θ_{ij} and a complex phase δ.

$$V_{CKM} = \begin{pmatrix} c_{12}c_{13} & s_{12}c_{13} & s_{13}e^{-i\delta} \\ -s_{12}c_{23} - c_{12}s_{23}s_{13}e^{i\delta} & c_{12}c_{23} - s_{12}s_{23}s_{13}e^{i\delta} & s_{23}c_{13} \\ s_{12}c_{23} - c_{12}s_{23}s_{13}e^{i\delta} & -c_{12}c_{23} - s_{12}s_{23}s_{13}e^{i\delta} & c_{23}c_{13} \end{pmatrix} \tag{1.11}$$

Where $s_{ij} \equiv \sin\theta_{ij}$, $c_{ij} \equiv \cos\theta_{ij}$. V_{CKM} should be unitary.

$$V_{CKM}^{\dagger} V_{CKM} = 1 \tag{1.12}$$

In (1.12) b row and d row, with leads to

$$V_{ud}V_{ub}^{*} + V_{cd}V_{cb}^{*} + V_{td}V_{tb}^{*} = 0. \tag{1.13}$$

(1.13) can be written as a triangle on complex plain since CKM matrix has complex phase, as shown in Figure 1.1.

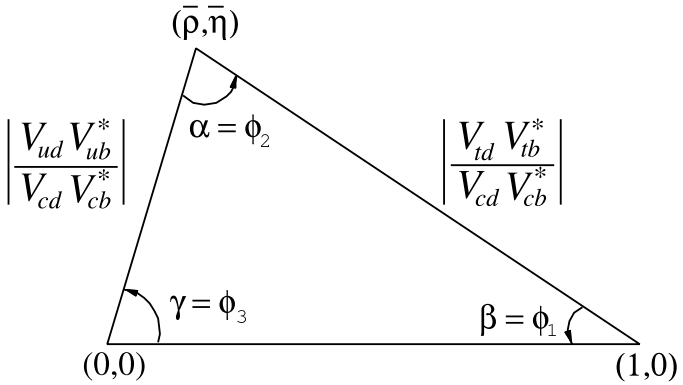

Figure 1.1: Unitarity triangle

To occur CPV, CKM matrix has non zero complex phase, in other wards, this unitarity triangle area is not zero. In Wolfenstein parametrization [3], CKM matrix is written by

$$V_{CKM} = \begin{pmatrix} 1 - \frac{\lambda^2}{2} & \lambda & A\lambda^3(\rho - i\eta) \\ -\lambda & 1 - \frac{\lambda^2}{2} & A\lambda^2 \\ A\lambda^3(1 - \rho - i\eta) & -A\lambda^2 & 1 \end{pmatrix} + O(\lambda^4). \tag{1.14}$$

The relation of (1.11) and (1.14) is

$$s_{12} \equiv \lambda,\ s_{23} \equiv A\lambda^2,\ s_{13} \equiv A\lambda^3(\rho - i\eta). \tag{1.15}$$

Where λ, A, ρ, η are real number, and $\lambda = \sin\theta_c \sim 0.22$, θ_c is Cabibbo angle, $|A|$, $|\rho|$, $|\eta|$ are all ~ 1. Here, we define

$$\overline{\rho} = \rho(1 - \frac{\lambda^2}{2}) \tag{1.16}$$

$$\overline{\eta} = \eta(1 - \frac{\lambda^2}{2}). \tag{1.17}$$

V_{td} can be written

$$V_{td} = A\lambda^3(1 - \overline{\rho} - i\overline{\eta}). \tag{1.18}$$

The lengths of each side of the triangle are described as follow

$$\begin{aligned} R_b &\equiv \frac{|V_{ud}V_{ub}^*|}{|V_{cd}V_{cb}^*|} = \sqrt{\overline{\rho}^2 + \overline{\eta}^2} \\ &= \frac{1 - \frac{\lambda^2}{2}}{\lambda}\frac{|V_{ub}^*|}{|V_{cb}|}, \end{aligned} \tag{1.19}$$

$$\begin{aligned} R_t &\equiv \frac{|V_{td}V_{tb}^*|}{|V_{cd}V_{cb}^*|} = \sqrt{(1 - \overline{\rho})^2 + \overline{\eta}^2} \\ &= \frac{1}{\lambda}\frac{|V_{td}^*|}{|V_{cb}|}. \end{aligned} \tag{1.20}$$

The angles of triangle are defined,

$$\phi_1 \equiv \arg\left(-\frac{V_{cd}V_{cb}^*}{V_{td}V_{tb}^*}\right), \tag{1.21}$$

$$\phi_2 \equiv \arg\left(-\frac{V_{td}V_{tb}^*}{V_{ud}V_{ub}^*}\right), \tag{1.22}$$

$$\phi_3 \equiv \arg\left(\frac{V_{ud}V_{ub}^*}{-V_{cd}V_{cb}^*}\right). \tag{1.23}$$

In this thesis, CPV angles are described as $\phi_{1,2,3}$, however sometimes they are written conventionally $\phi_1 = \beta$, $\phi_2 = \alpha$ and $\phi_3 = \gamma$. The R_b, R_t and $\phi_{1,2,3}$ can be measured by B meson decay. The confirmation with many phenomena are equivalent to validation of SM. The current result of $\phi_{1,2,3}$ measurements in CKMfitter [4] are.

- $\phi_1 = (21.50^{+0.75}_{-0.74})^\circ$
- $\phi_2 = (85.4^{+4.0}_{-3.9})^\circ$
- $\phi_3 = (70.0^{+7.7}_{-9.0})^\circ$

ϕ_3 is the most difficult parameter to measure among the CPV angles.

1.2 CP Asymmetry

1.2.1 $B^0 - \bar{B}^0$ Mixing

Consider the CP asymmetry for B meson with mixing of $B^0 - \bar{B}^0$. When we write the arbitrary linear-combination of flavor eigenstate of B as

$$a\,|B^0\rangle + b\,|\bar{B}^0\rangle\,, \tag{1.24}$$

the time revolution is

$$i\hbar\frac{d}{dt}\begin{pmatrix} a \\ b \end{pmatrix} = \mathcal{H}\begin{pmatrix} a \\ b \end{pmatrix} \equiv (M - i\Gamma)\begin{pmatrix} a \\ b \end{pmatrix}. \tag{1.25}$$

Where M and Γ are 2×2 Hermitian matrix. Mass eigenstates $|B_H\rangle$ and $|B_L\rangle$ are written as

$$|B_H\rangle \quad = p\,|B^0\rangle + q\,|\bar{B}^0\rangle \tag{1.26}$$

$$|B_L\rangle \quad = p\,|B^0\rangle - q\,|\bar{B}^0\rangle\,, \tag{1.27}$$

and those eigenvalues are given

$$\lambda_H \quad = m_H - \frac{i}{2}\gamma_H \tag{1.28}$$

$$\lambda_L \quad = m_L - \frac{i}{2}\gamma_L. \tag{1.29}$$

Where p and q are complex numbers, and $m_{H,L}$ and $\gamma_{H,L}$ are real numbers. The time revolution for mass eigenstate is written as

$$i\hbar\frac{d}{dt}\,|B_{H,L}(t)\rangle = \lambda_{H,L}\,|B_{H,L}(t)\rangle\,. \tag{1.30}$$

And

$$|B_{H,L}(t)\rangle = e^{-i\lambda_{H,L}t}\,|B_{H,L}(t)\rangle\,. \tag{1.31}$$

From Eq. 1.26 - 1.31, B^0, $\bar{B}^0$ time revolution are written as

$$|B^0(t)\rangle \quad = f_+(t)\,|B^0(0)\rangle + \frac{q}{p}f_-(t)\,|\bar{B}^0\rangle \tag{1.32}$$

$$|\bar{B}^0(t)\rangle \quad = f_+(t)\,|\bar{B}^0(0)\rangle + \frac{p}{q}f_-(t)\,|B^0\rangle\,, \tag{1.33}$$

where

$$f_+(t) \equiv \frac{1}{2}(e^{\lambda_H} + e^{\lambda_L}) = e^{-i\frac{\bar{m}}{2}t}e^{-i\frac{\gamma}{2}t}\cos\frac{\Delta m}{2}t \tag{1.34}$$

$$f_-(t) \equiv \frac{1}{2}(e^{\lambda_H} - e^{\lambda_L}) = -ie^{-i\frac{\bar{m}}{2}t}e^{-i\frac{\gamma}{2}t}\sin\frac{\Delta m}{2}t \tag{1.35}$$

$$\Delta m \equiv m_H - m_L,\ \bar{m} \equiv \frac{m_K + m_L}{2} \tag{1.36}$$

$$\gamma \simeq \gamma_H \simeq \gamma_L,\ \Delta\gamma \equiv \gamma_H - \gamma_L \simeq 0, \tag{1.37}$$

and this equations show B^0-$\bar{B}^0$ mixing.

1.2.2 Branching Fraction B^0 and $\bar{B}^0$

Decay widths A_f and $\bar{A}_f$ of B^0 and $\bar{B}^0$ to final state f are written as

$$A_f \equiv \langle f|H|B^0\rangle \tag{1.38}$$
$$\bar{A}_f \equiv \langle f|H|\bar{B}^0\rangle\,. \tag{1.39}$$

Decay width of B^0 and $\bar{B}^0$ at time t decay to f in minute time are written as

$$A_f(t) = \langle f|H|B^0(t)\rangle = A_f(f_+ + \frac{q}{p}f_-\bar{\rho}_f) \tag{1.40}$$
$$\bar{A}_f(t) = \langle f|H|\bar{B}^0(t)\rangle = A_f(f_+\bar{\rho}_f + \frac{p}{q}f_-), \tag{1.41}$$

where

$$\bar{\rho}_f \equiv \frac{\bar{A}_f}{A_f} = \frac{1}{\rho_f}. \tag{1.42}$$

From Eq. 1.40 and Eq. 1.41, the branching ratios of B^0 and $\bar{B}^0$ to f at time t are written as

$$\Gamma(B^0(t)\to f) = |A_f|^2\left(|f_+|^2 + |\frac{q}{p}|^2|\bar{\rho}_f|^2|f_-|^2 + 2Re(\frac{q}{p}\frac{1}{\bar{\rho}_f}f_+\bar{f_-})\right) \tag{1.43}$$
$$\Gamma(\bar{B}^0(t)\to f) = |A_f|^2\left(|\bar{\rho}_f||f_+|^2 + |\frac{p}{q}|^2|f_-|^2 + 2Re(\frac{p}{q}\bar{\rho}_f f_+\bar{f_-})\right). \tag{1.44}$$

1.2.3 Direct CP Violation

Consider processes $B\to f$ and $\bar{B}\to\bar{f}$ to consider the CP violation in B meson decay. Using strong phase δ and weak phase ϕ which comes from complex component of CKM matrix, those decay widths A_f and $\bar{A}_{\bar{f}}$ are written as

$$A_f = \sum_i A_i e^{i(\delta_i+\phi_i)} \tag{1.45}$$
$$\bar{A}_{\bar{f}} = \sum_i A_i e^{i(\delta_i-\phi_i)}. \tag{1.46}$$

Sign of δ does not flip with CP conversion because δ is the phase coming from strong interaction. However, sign of ϕ flip due to complex of $V_{\rm CKM}$.

CP asymmetry is written as

$$\mathcal{A}_f = \frac{\Gamma(B\to f)-\Gamma(\bar{B}\to\bar{f})}{\Gamma(B\to f)+\Gamma(\bar{B}\to\bar{f})} \tag{1.47}$$
$$= \frac{1-|\bar{A}_{\bar{f}}/A_f|^2}{1+|\bar{A}_{\bar{f}}/A_f|^2}. \tag{1.48}$$

That is

$$|\,\frac{\bar{A}_{\bar{f}}}{A_f}\,| \neq 1 \tag{1.49}$$

i.e. if

$$|A_f|^2 - |\bar{A}_{\bar{f}}|^2 = -2\sum_{i,j}\sin(\phi_i - \phi_j)\sin(\delta_i - \delta_j) \tag{1.50}$$

is not zero, CP violation is occurred. This is called direct CP violation. To occur the CP violation, it needs up to two processes to same final state, almost same decay widths, non zero strong phase difference, and non zero weak phase deference.

1.3 ϕ_3 Measurements

$$\phi_3 \sim \arg(V_{ub}^*) \tag{1.51}$$

$B \to DK$ which include $b \to u$ process is used. We explain three methods (GLW, ADS and GGSZ method) to measure ϕ_3 hereinafter. Currently, ϕ_3 is measured by charged $B^\pm \to DK^\pm$ studies. However motivation in this study is the measurement of CP violation from ϕ_3 effect in neutral $B^0 \to DK^{*0}$ decay.

1.3.1 GLW Method

In GLW (Gronau-London-Wyler) method [5, 6], decay process $B \to \tilde{D}K$ is used to measure the ϕ_3. $\tilde{D}$ is the CP eigenstate of neutral D meson. Hereinafter D_1, D_2 are CP-even, CP-odd eigenstate, and

$$D_{1,2} = \frac{1}{\sqrt{2}}(D^0 \pm \bar{D}^0) \tag{1.52}$$

respectively. For example, D_1 corresponds to $\tilde{D} \to K^+K^-, \pi^+\pi^-$, D_2 is $\tilde{D} \to K^0_S\pi^0, K^0_S\omega, K^0_S\phi$ and so on. Figure 1.2 shows $B^0 \to \tilde{D}^0K^{*0}$, $\tilde{D}^0 \to K^+K^-$ diagrams. From Eq. 1.46 am-

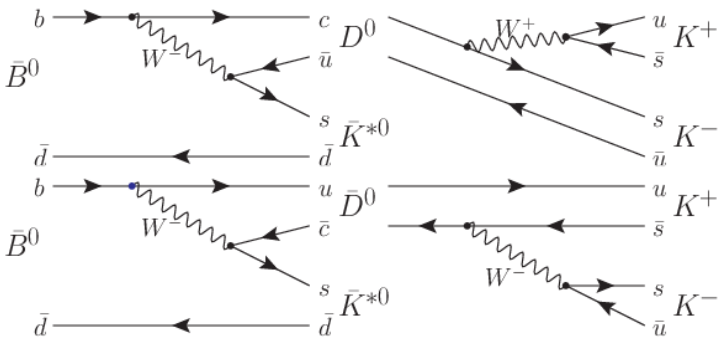

Figure 1.2: $B^0 \to \tilde{D}^0K^{*0}$, $\tilde{D}^0 \to K^+K^-$ diagrams.

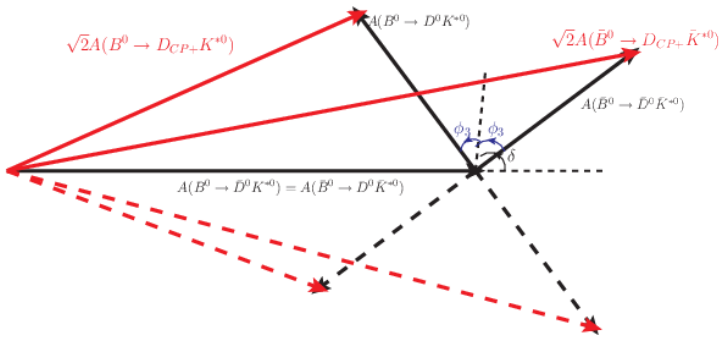

Figure 1.3: Relation the amplitudes fo (1.53) and (1.54)

plitudes of $B \to D_{1,2}K$ are written in

$$A(B^0 \to D_1K^{*0}) = \frac{1}{\sqrt{2}}\left(A(B^0 \to D^0K^{*0})e^{i(\phi_3+\delta_1)} + A(B^0 \to \bar{D}^0K^{*0})\right) \tag{1.53}$$

$$A(\bar{B}^0 \to D_1\bar{K}^{*0}) = \frac{1}{\sqrt{2}}\left(A(\bar{B}^0 \to \bar{D}^0\bar{K}^{*0})e^{i(-\phi_3+\delta_1)} + A(\bar{B}^0 \to D^0K^-)\right) \tag{1.54}$$

$$A(B^0 \to D_2K^{*0}) = \frac{1}{\sqrt{2}}\left(A(B^0 \to D^0K^{*0})e^{i(\phi_3+\delta_2)} - A(B^0 \to \bar{D}^0K^{*0})\right) \tag{1.55}$$

$$A(\bar{B}^0 \to D_2\bar{K}^{*0}) = \frac{1}{\sqrt{2}}\left(-A(\bar{B}^0 \to \bar{D}^0\bar{K}^{*0})e^{i(-\phi_1+\delta_2)} + A(\bar{B}^0 \to D^0\bar{K}^{*0})\right). \tag{1.56}$$

Due to the phase flip of ϕ_3 on CP conversion, CP asymmetry is occurred. $\delta_{1,2}$ are difference of strong phase between $\bar{B}^0 \to \bar{D}^0\bar{K}^{*0}$ and $\bar{B}^0 \to D^0\bar{K}^{*0}$, and $\delta_2 = \delta_1 + \pi$. The relation with Eq. 1.53 and 1.54 can be written on complex plane as shown Fig. 1.3. The appearance of ϕ_3 effect can be seen.

From Eq. 1.53-1.56, CP asymmetry $\mathcal{A}_{1,2}$ and ratios of branching ratios $B \to D_{1,2}K^*$ and $B \to \tilde{D}^0K^*$ $\mathcal{R}_{1,2}^{DK^*}$ are written in

$$\begin{aligned}\mathcal{A}_{1,2} &\equiv \frac{\Gamma(\bar{B}^0 \to D_{1,2}\bar{K}^{*0}) - \Gamma(B^0 \to D_{1,2}K^{*0})}{\Gamma(\bar{B}^0 \to D_{1,2}\bar{K}^{*0}) + \Gamma(B^0 \to D_{1,2}K^{*0})} \\ &= \frac{2r_B \sin\phi_3 \sin\delta_{1,2}}{1 + r_B^2 + 2r_B\cos\phi_3\cos\delta_{1,2}}\end{aligned} \tag{1.57}$$

$$\begin{aligned}\mathcal{R}_{1,2}^{DK^*} &\equiv \frac{\Gamma(\bar{B}^0 \to D_{1,2}\bar{K}^{*0}) + \Gamma(B^0 \to D_{1,2}K^{*0})}{\Gamma(\bar{B}^0 \to D^0\bar{K}^{*0}) + \Gamma(B^0 \to D^0K^{*0})} \\ &= 1 + r_B^2 + 2r_B\cos\phi_3\cos\delta_{1,2},\end{aligned} \tag{1.58}$$

where,

$$r_B \equiv \frac{|A(\bar{B}^0 \to \bar{D}^0 \bar{K}^{*0})|}{|A(\bar{B}^0 \to D^0 \bar{K}^{*0})|}. \tag{1.59}$$

Once $\tilde{B}^0 \to D_{1,2}\tilde{K}^{*0}$ decays are observed, r_B, $\mathcal{A}_{1,2}$ and $\mathcal{R}_{1,2}^{DK^*}$ can be obtained. Therefore two unknown parameters ϕ_3 and $\delta_{1,2}$ can be obtained, from the two equations $\mathcal{A}_{1,2}$ and $\mathcal{R}_{1,2}^{DK^*}$.

1.3.2 ADS Method

In ADS (Atwood-Donietz-Soni) method, decay process $B \to \tilde{D}K$ is used to measure the ϕ_3 [7,8]. Here $\tilde{D}$ does not decay to CP eigenstate, but decays modes are $K^{\pm}\pi^{\mp}$, $K^{\pm}\pi^{\mp}\pi^0$, $3K\pi$ and so on. Figure 1.4 shows $\bar{B}^0 \to \tilde{D}^0\bar{K}^{*0}$, $\tilde{D}^0 \to K^{\pm}\pi^{\mp}$ diagrams.

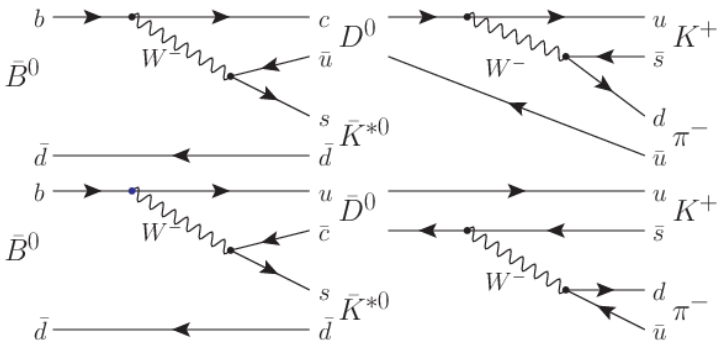

Figure 1.4: $\bar{B}^0 \to \tilde{D}^0\bar{K}^{*0}$, $\tilde{D}^0 \to K^{\pm}\pi^{\mp}$ diagrams.

Representing final state of $\tilde{D}$ as f, amplitudes of B and D decay as

$$\begin{aligned} A_B &= A(\bar{B}^0 \to D^0\bar{K}^{*0}) = A(B^0 \to \bar{D}^0 K^{*0}) && (1.60)\\ \bar{A}_B &= A(\bar{B}^0 \to \bar{D}^0\bar{K}^{*0}) = A(B^0 \to D^0 K^{*0}) && (1.61)\\ A_D &= A(\bar{D}^0 \to f) && (1.62)\\ \bar{A}_D &= A(D^0 \to f), && (1.63) \end{aligned}$$

and a branching fraction of $\bar{B}^0 \to \tilde{D}\bar{K}^{*0} \to f\bar{K}^{*0}$ can be written as

$$\begin{aligned} \Gamma(\bar{B}^0 \to [f]_D\bar{K}^{*0}) &= |A(\bar{B}^0 \to [f]_{D^0}\bar{K}^{*0}) + A(\bar{B}^0 \to [f]_{\bar{D}^0}\bar{K}^{*0})|^2 \\ &= |A_B|^2|A_D|^2\left(r_B^2 + r_D^2 + 2r_B r_D\cos(-\phi_3 + \delta_B + \delta_{D_f})\right), \end{aligned} \tag{1.64}$$

and one of $B^0 \to \tilde{D}K^{*0} \to \bar{f}K^{*0}$ as

$$\begin{aligned} \Gamma(B^0 \to [\bar{f}]_D K^{*0}) &= |A(B^0 \to [\bar{f}]_{\bar{D}^0}K^{*0}) + A(B^0 \to [\bar{f}]_{D^0}K^{*0})|^2 \\ &= |A_B|^2|A_D|^2\left(r_B^2 + r_D^2 + 2r_B r_D\cos(+\phi_3 + \delta_B + \delta_{D_f})\right). \end{aligned} \tag{1.65}$$

Where

$$r_B = \frac{|\bar{A}_B|}{|A_B|},\ r_D = \frac{|\bar{A}_D|}{|A_D|}, \tag{1.66}$$

and δ_B is difference of strong phase between $\bar{B}^0 \to D^0\bar{K}^{*0}$ and $\bar{B}^0 \to \bar{D}^0\bar{K}^{*0}$, δ_{D_f} is difference of strong phase between $D^0 \to f$ and $\bar{D}^0 \to f$. δ_{D_f} is dependent on final state of D which in f. Hereinafter CP asymmetry $\mathcal{A}_f$ and ratios of branching ratios $B \to fK^*$ and $B \to \bar{f}K^*$ are written as

$$\begin{aligned}
\mathcal{A}_f &\equiv \frac{\Gamma(\bar{B}^0 \to [f]_D\bar{K}^{*0}) - \Gamma(B^0 \to [\bar{f}]_D K^{*0})}{\Gamma(\bar{B}^0 \to [f]_D\bar{K}^{*0}) + \Gamma(B^0 \to [\bar{f}]_D K^{*0})} \\
&= \frac{2r_B r_D \sin\phi_3 \sin\delta_1}{r_B^2 + r_D^2 + 2r_B r_D \cos\phi_3 \cos(\delta_B + \delta_{D_f})} \qquad (1.67) \\
\mathcal{R}_f &\equiv \frac{\Gamma(\bar{B}^0 \to [f]_D\bar{K}^{*0}) + \Gamma(B^0 \to [\bar{f}]_D K^{*0})}{\Gamma(\bar{B}^0 \to [\bar{f}]_D\bar{K}^{*0}) + \Gamma(B^0 \to [f]_D K^{*0})} \\
&= r_B^2 + r_D^2 + 2r_B r_D \cos\phi_3 \cos(\delta_B + \delta_{D_f}). \qquad (1.68)
\end{aligned}$$

Assuming we have known i kinds of f_i, replacing $\delta_{f_i} \equiv \delta_B + \delta_{f_i}$, $\mathcal{A}_{f_i}$ and $\mathcal{R}_{f_i}$ can be written as

$$\begin{aligned}
\mathcal{A}_{f_1} &= \mathcal{A}_{f_1}(r_B, \phi_3, \delta_{f_1}) \qquad (1.69) \\
\mathcal{R}_{f_1} &= \mathcal{R}_{f_1}(r_B, -\phi_3, \delta_{f_1}) \qquad (1.70) \\
\mathcal{A}_{f_2} &= \mathcal{A}_{f_2}(r_B, \phi_3, \delta_{f_2}) \qquad (1.71) \\
\mathcal{R}_{f_2} &= \mathcal{A}_{f_2}(r_B, -\phi_3, \delta_{f_2}) \qquad (1.72) \\
&\vdots
\end{aligned}$$

Thus if we measure n modes f in $B \to DK$, $2n$ equation and $n+2$ unknowns are obtained. To extract ϕ_3, we should measure two or more f modes. And also it is possible to combine the $\mathcal{A}$ and $\mathcal{R}$ from GLW measurements.

1.3.3 GGSZ Method

In GGSZ (Giri-Grossman-Soffer-Zupan) method, decay process $B \to \tilde{D}K$ is used to measure the ϕ_3, here $\tilde{D}$ has three body decay such as $K_S\pi^+\pi^-$. We measure the effect of interference on the $D \to K_S\pi^+\pi^-$ plane called Dalitz plane defined by two dimension $m_+^2 = m_{K_S^0\pi^+}^2$ and $m_-^2 = m_{K_S^0\pi^-}^2$. Assuming no CP asymmetry in neutral D decays, the amplitude for $B^+ \to [K_S^0\pi^+\pi^-]_D K^+$ decay as a function of Dalitz plot variables m_+^2 and m_-^2 is

$$A_{B^+} = A_D(m_+^2, m_-^2) + r_B e^{i\phi_3 + i\delta_B} A_D(m_-^2, m_+^2) \qquad (1.73)$$

where $f_D(m_+^2, m_-^2)$ is the amplitude of the $\bar{D}^0 \to K_S^0\pi^+\pi^-$ decay. Similarly, the amplitude for $B^- \to [K_S^0\pi^+\pi^-]_D K^-$ decay is

$$A_{B^-} = A_D(m_-^2, m_+^2) + r_B e^{-i\phi_3 + i\delta_B} A_D(m_+^2, m_-^2) \qquad (1.74)$$

With large sample of flavor-tagged $\bar{D}^0 \to K_S^0\pi^+\pi^-$ decays produced in the continuum e^+e^- annihilation, the $\bar{D}^0 \to K_S^0\pi^+\pi^-$ decay amplitude f_D can be determined. Once f_D is known, a simultaneous fit to B^0 and $\bar{B}^0$ data allows the contributions of r_B, and δ_B to be

separated. This method has only two-fold ambiguity: $(\phi_3,\, \delta_B)$ and $(\phi_3 + 180°,\, \delta_B + 180°)$ solutions can not be distinguished. Due to the fact that r_B is bound to be positive, the direct extraction of r_B, δ_B and ϕ_3 can be biased. To avoid these biases, the Cartesian coordinates have been introduced, $x_\pm = r_B \cos(\delta_B \pm \phi_3)$ and $y_\pm = r_B \sin(\delta_B \pm \phi_3)$.

1.3.4 Dalitz Analysis

Dalitz plot analysis of three-body decays of neutral D mesons is a useful tool in various measurements where coherent admixtures of D^0 and $\overline{D}^0$ are observed. This technique was initially proposed for the measurement of the unitarity triangle angle ϕ_3 in $B \to DK$ decays [9, 10]. Later it was applied to the measurement of charm mixing [11, 12] and to the resolution of the quadratic ambiguity in the measurement of the angle ϕ_1 using a time-dependent analysis of the decay $B^0 \to D\pi^0$ [13, 14]. Most of these measurements are based on the $D \to K^0_S\pi^+\pi^-$ decay which offers the best precision in among three-body D^0 decays.

The technique is model-dependent — it depends on the complex amplitude of the D^0 decay which is obtained from the $D^{*+} \to D^0\pi^+$ sample using model assumptions. The result of the measurement contains therefore model uncertainties. In the case of ϕ_3 measurement, this uncertainty ($\sim$ 10°) is already comparable to the statistical accuracy [15, 16].

However, a modification of the Dalitz analysis is possible so as to perform a completely model-independent measurement [9]. It requires the phase space of the three-body D decay to be divided into bins as shown in Fig 1.5. Information about the complex phase in

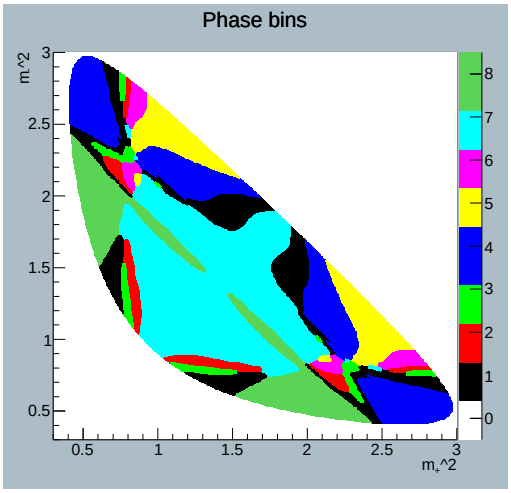

Figure 1.5: One of example of binning on Dalitz plane, eight binning. Binning index sign is flipped $m^2_+ = m^2_-$ reflection.

each bin can be extracted from the quantum-correlated D^0 decays from $\psi(3770) \to D\overline{D}$ process. The measurement of the strong phase in bins of the $D \to K^0_S\pi^+\pi^-$ phase space was recently performed by the CLEO collaboration [17]. This measurement should allow

to reduce the error of ϕ_3 related to the uncertainty in the $D \to K^0_S\pi^+\pi^-$ amplitude to $1-3^\circ$.

The binned approach allows not only to get rid of the model error, but also to reduce the systematic uncertainties. In our analysis, we try to develop the analysis procedure that minimizes the systematic uncertainties, in view of the future high-precision analyses at the super-B factory where systematics can become a limiting factor.

1.3.5 Model-independent Binned Analysis of Three-body D^0 Decays

In $B^\pm \to DK^\pm$ decay

To introduce the notation we briefly recap the technique of model-independent binned Dalitz plot analysis of $B^\pm \to DK^\pm$, $D \to K^0_S\pi^+\pi^-$ decays used to extract the angle ϕ_3. As usually presented, this does not take charm mixing effects into account.

The amplitude of the $B^+ \to DK^+$, $D \to K^0_S\pi^+\pi^-$ decay can be written as

$$A_B = \overline{A} + r_B e^{i(\phi_3+\delta_B)} A \tag{1.75}$$

where $\overline{A} = \overline{A}(m^2_{K_S\pi^+}, m^2_{K_S\pi^-}) = \overline{A}(m^2_+, m^2_-)$ is the amplitude of the $\overline{D}^0 \to K^0_S\pi^+\pi^-$ decay, $A = A(m^2_+, m^2_-)$ is the amplitude of the $D^0 \to K^0_S\pi^+\pi^-$ decay ($A(m^2_+, m^2_-) = \overline{A}(m^2_-, m^2_+)$ in the case of CP conservation in D decay), r_B is the ratio of the absolute values of the interfering $B^+ \to \overline{D}^0 K^+$ and $B^+ \to D^0 K^+$ amplitudes, and δ_B is the strong phase difference between these amplitudes. The density of the D decay Dalitz plot from $B^+ \to DK^+$ decay is given by the absolute value squared of the amplitude

$$P_B = |A_B|^2 = |\overline{A} + r_B e^{i(\delta_B+\phi_3)} A|^2 = \overline{P} + r_B^2 P + 2\sqrt{P\overline{P}}(x_+ C + y_+ S) \tag{1.76}$$

where

$$x_+ = r_B \cos(\delta_B + \phi_3); \quad y_+ = r_B \sin(\delta_B + \phi_3) \tag{1.77}$$

The functions $C = C(m^2_+, m^2_-)$ and $S = S(m^2_+, m^2_-)$ are the cosine and sine of the strong phase difference $\delta_D = \arg\overline{A} - \arg A$ between the $\overline{D}^0 \to K^0_S\pi + \pi-$ and $D^0 \to K^0_S\pi^+\pi^-$ amplitudes :

$$C = \cos\delta_D(m^2_+, m^2_-); \quad S = \sin\delta_D(m^2_+, m^2_-) \tag{1.78}$$

The equations for the charge-conjugate mode $B^- \to DK^-$ are obtained with the substitution $\phi_3 \to -\phi_3$. Using both B charges, one can obtain ϕ_3 and δ_B separately. Figure 1.6 shows the picture of how to observe the effect of ϕ_3.

In the binned model-independent approach, the Dalitz plot is divided into $2\mathcal{N}$ bins symmetrically to the exchange $m^2_- \leftrightarrow m^2_+$. The expected number of events in the bin "i" (B of the Dalitz plot of D from $B^+ \to DK^+$ is

$$N^+_i = h_B[K_i + r_B^2 K_{-i} + 2\sqrt{K_i K_{-i}}(x_+ c_i + y_+ s_i)] \tag{1.79}$$

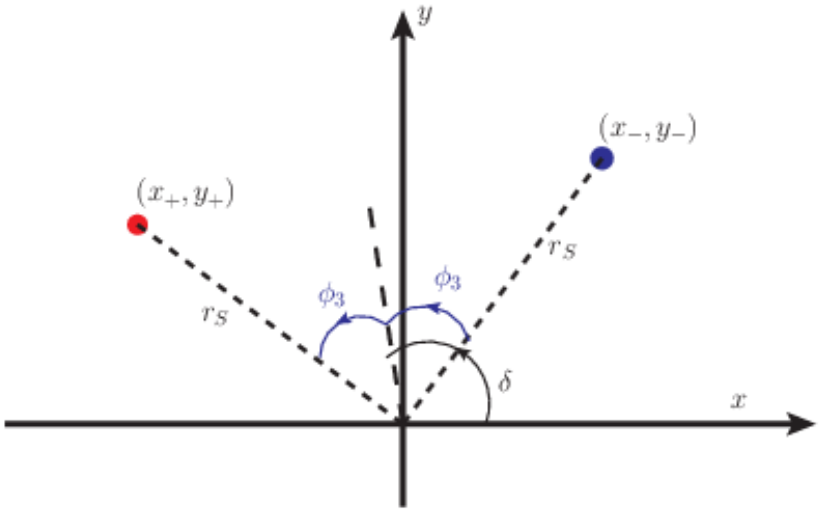

Figure 1.6: Image of ϕ_3 effect on ($x_\pm$, $y_\pm$) Dalitz analysis observables.

where K_i is the number of events in the corresponding bin of the Dalitz plot of the D meson in a flavor eigenstate (obtained using $D^{*\pm} \to D\pi^\pm$ samples) and h_B is a normalization constant which is proportional to total signal number. The bin index " i " ranges from $-\mathcal{N}$ to $\mathcal{N}$ (excluding 0); the exchange $m_+^2 \leftrightarrow m_-^2$ corresponds to the exchange $i \leftrightarrow -i$. The terms c_i and s_i include information about the cosine and sine of the phase difference averaged over the bin region:

$$c_i = \frac{\int_{\mathcal{D}_i} |A||\overline{A}| \cos\delta_D d\mathcal{D}}{\sqrt{\int_{\mathcal{D}_i} |A|^2 d\mathcal{D} \int_{\mathcal{D}_i} |\overline{A}|^2 d\mathcal{D}}} \tag{1.80}$$

Here $\mathcal{D}$ represents the Dalitz plot phase space and $\mathcal{D}_i$ is the bin region over which the integration is performed. The terms s_i are defined similarly with cosine substituted by sine.

According to $i \leftrightarrow -i$ exchanging (reflection on $m_+^2 = m_-^2$ line), the symmetry under $\pi^+ \leftrightarrow \pi^-$ requires $c_i = c_{-i}$ and $s_i = -s_{-i}$. The values of c_i and s_i terms can be provided by charm-factory experiments operated at the threshold of $D\overline{D}$ pair production [17]. The wave function of the two mesons is antisymmetric, thus the four-dimensional density of two correlated $D \to K_S^0\pi^+\pi^-$ Dalitz plots is

$$\begin{aligned} |A_{corr}(m_+^2, m_-^2, m_+'^2, m_-'^2)|^2 &= |A_1\overline{A}_2 - \overline{A}_1 A_2|^2 \\ &= P_1\overline{P}_2 + \overline{P}_1 P_2 - \sqrt{P_1\bar{P}_2\bar{P}_1 P_2}(C_1C_2 + S_1S_2) \end{aligned} \tag{1.81}$$

where the indices "1" and "2" correspond to the two decaying D mesons. In the case of a binned analysis, the number of events in the region of the $(K_S^0\pi^+\pi^-)^2$ phase space described by the indices "i" and "j" is

$$M_{ij} = K_i K_{-j} + K_{-i} K_j + 2\sqrt{K_i K_{-i} K_j K_{-j}}(c_i c_j + s_i s_j) \tag{1.82}$$

Once the values of the terms c_i and s_i are known from charm-factory data, the system of equations (1.79) contains only three free parameters (x, y, and h_B) for each B charge, and can be solved using maximum likelihood method to extract the value of ϕ_3.

Note that technically the system (1.79) can be solved without external constraints on c_i and s_i for $\mathcal{N} \geq 2$. However, due to the small value of r_B, there is very little sensitivity to the c_i and s_i parameters in $B^{\pm} \to DK^{\pm}$ decays, which results in a reduction in the precision on ϕ_3 that can be obtained [18].

In $B^0 \to DK^{*0}$ decay

In this study we present the first measurement of the angle ϕ_3 using neutral B meson decays. We reconstruct $B^0 \to DK^{*0}$, with $K^{*0} \to K^+\pi^-$ (charge conjugate processes are assumed throughout the paper and K^{*0} refers to $K^*(892)^0$), where the flavor of the B meson is identified by the kaon electric charge. Neutral D mesons are reconstructed in the $K^0_S\pi^+\pi^-$ decay mode and are analyzed with the model independent Dalitz technique which is written above.

In analyzing $B^0 \to DK^{*0}$ decays, the natural width of the K^{*0} ($\sim 50\text{MeV}/c^2$) has to be considered. In the K^{*0} mass region, amplitudes for decays to higher-mass $K\pi$ resonances interfere with the signal decay amplitude and width each other. For this analysis we use effective variables, introduced in Ref. [19], obtained by integrating amplitude over a region of the $B^0 \to DK^+\pi^-$ Dalitz plot corresponding to the K^{*0}. For this purpose we introduce the quantities r_S, k, and δ_S defined as

$$r_S^2 = \frac{\Gamma(B^0 \to D^0K^+\pi^-)}{\Gamma(B^0 \to \overline{D}^0K^+\pi^-)} = \frac{\int dpA_u^2(p)}{\int dpA_c^2(p)} \tag{1.83}$$

$$ke^{i\delta_S} = \frac{\int A_c(p)A_u(p)e^{i\delta(p)}}{\sqrt{\int dpA_c^2(p)\int dpA_u^2(p)}} \tag{1.84}$$

where $0 \leq k \leq 1$ and $\delta_S \in [0,\ 2\pi]$. The amplitudes for the $b \to c$ and $b \to u$ transitions, $A_c(p)$ and $A_u(p)$, are real and positive and $\delta(p)$ is the relative strong phase. The variable p indicates the position in the $DK^+\pi^-$ Dalitz plot. In case of a two-body B decay, r_S and δ_S become $r_B = \mid A_u \mid / \mid A_c \mid$ and δ_B (the strong phase difference between A_u and A_c) and $k = 1$. Because of CKM factors and the fact that both diagrams, for the neutral B decays we consider, are color suppressed, the average amplitude ratio r_S in $B^0 \to DK^{*0}$ is expected to be in the range [0.3, 0.5], larger than the analogous ratio for charged $B^{\pm} \to DK^{\pm}$ decays (which is of the order of 10% [4, 20]). An earlier measurement sets an upper limit $r_S < 0.4$ at 90% probability [21]. A phenomenological approach from $B^+ \to D^0K^+$ and $B^0 \to D^0K^0$ [22] proposed to evaluate r_B in the $B^0 \to DK^0$ system gives $r_B = 0.27 \pm 0.18$.

Finally, we consider the signal number of i bin on Dalitz plot is

$$\begin{aligned} N_i = &\quad h_B[K_i + r_S^2K_{-i} + 2k\sqrt{K_iK_{-i}}(xc_i + ys_i)] \ \ (\text{on } B^0) \\ \overline{N}_i = &\quad \overline{h}_B[K_{-i} + r_S^2K_i + 2k\sqrt{K_iK_{-i}}(\overline{x}c_{-i} + \overline{y}s_{-i})] \ \ (\text{on } \overline{B}^0). \end{aligned} \tag{1.85}$$

Here, $x = r_S \sin(\delta_S + \phi_3)$, $y = r_S \cos(\delta_S + \phi_3)$, $\bar{x} = r_S \sin(\delta_S - \phi_3)$, $\bar{y} = r_S \cos(\delta_S - \phi_3)$. Where, this $x(\bar{x})$ is correspond to the $x_+(x_-)$ in charged B Dalitz, and $y(\bar{y})$ is the $y_+(y_-)$. Only differences are $r_B \Rightarrow r_S$ and $\delta_B \Rightarrow \delta_S$.

Note that the effects of the CP violation to the observables are limited by value of $r_{B,S}$. Briefly, ϕ_3 precision scales as $1/r_{B,S}$. r_S will be lager than r_B because of color suppression on favored decay. ϕ_3 measurement with neutral $B^0 \to DK^{*0}$ is hopeful.

Chapter 2

Experimental Apparatus and Analysis Tools

In this chapter, we describe the experimental apparatus and analysis tools. The data set we use is collected with the Belle detector at the KEKB accelerator located at High Energy Accelerator Research Organization (KEK) in Tsukuba-city, Japan. All the developments and the constructions shown in this chapter have been done by the collaborators.

2.1 KEKB Accelerator

KEKB [23] is tow-ring energy-asymmetric e^+e^- collider intended for large number of B and $\bar{B}$ meson pairs production. Figure 2.1 shows schematic view of KEKB accelerator. The electrons emitted from the thermionic gun are collected to make electron bunch. And to produce positron bunch, parts of thermionic gun electron are injected into tungsten target. A linear accelerator (Linac) accelerates electron and positron up to the required energy and injects then to each storage ring.The tow ring in KEKB accelerator to store beam bunch, are the one for 8 GeV electron named High Energy Ring (HER), and the other for 3.5 GeV positron named Low Energy Ring (LER) respectively. In both ring, radio-frequency cavities accelerate particles, while the dipole (quadruple) magnets bend (focus) them. The beams are collided at the interaction point (IP) with crossing angle of ± 11 mrad.

The KEKB center-of-mass energy is designed to be

$$\sqrt{s} = 2\sqrt{E_{\rm HER} \cdot E_{\rm LER}} = 10.58 \text{ GeV}, \tag{2.1}$$

which corresponds to the $\Upsilon(4S)$ resonance mass, i.e. $B\bar{B}$ pare production threshold. In this situation, the cross-section for various processes in e^+e^- collision are summarized in Table 2.1.

The $b\bar{b}$ pair production cross-section is about 1.1 nb. The $\Upsilon(4S)$ stand on top of large $q\bar{q}$, $(q = u, d, s, c)$ continuum backgrounds. KEKB is called B-factory because it is operated at $\Upsilon(4S)$ resonance and $\Upsilon(4S)$ dominantly decay to $B^0\bar{B}^0$ and B^+B^-. In this

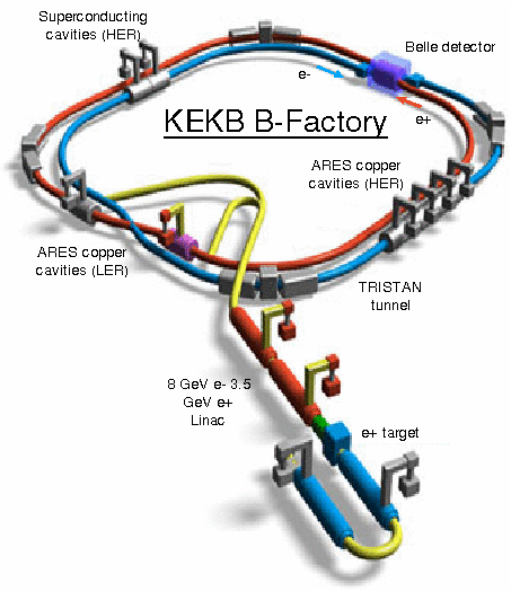

Figure 2.1: KEKB accelerator

Process	σ [nb]
$b\bar{b}$	1.1
$c\bar{c}$	1.3
$q\bar{q}(q{=}u,d,s)$	2.1
$\tau\bar{\tau}$	0.93
QCD $(25.551^\circ < \theta < 159.94^\circ)$	37.8
$\gamma\gamma$	11.1

Table 2.1: Various e^+e^- process at $\sqrt{s} = 10.58$ GeV cross-section.

situation, the Lorentz boost is

$$\beta\gamma = \frac{E_{\rm HER} - E_{\rm LER}}{2\sqrt{E_{\rm HER}E_{\rm LER}}} = 0.425, \tag{2.2}$$

due to the energy asymmetry. The integrated luminosity of 711 fb^{-1} is recorded at the $\Upsilon(4S)$ resonance, where 772×10^{-6} $B\bar{B}$ pairs are produced.

For $B^0 \to DK^{*0}$ signal in this study branching ratio is less than charged $B^+ \to DK^+$ as.

$$\begin{aligned} \Gamma(B^+ \to \bar{D}^0 K^+) &= (3.65 \pm 0.33) \times 10^{-4}, \\ \Gamma(B^0 \to \bar{D}^0 K^{*0}) &= (4.2 \pm 0.6) \times 10^{-5}. \end{aligned}$$

Thanks to KEKB largest $B\bar{B}$ dataset in the world of lepton colliders, we can do this analysis.

2.2 Belle Detector

Covering KEKB interaction point, Belle detector [24] is installed. Belle detector is a general-purpose detector consist of a many sub-detectors. Figure 2.2 shows the configuration of the Belle detector. From inner to outer, There are silicon vertex detector (SVD), central drift chamber (CDC), aerogel Cherenkov counter (ACC), time-of-flight counter (TOF), electro-magnetic calorimeter (ECL), and outermost coverage K_L and muon detector (KLM). SVD and CDC provide charged particle tracking and vertex measurement. Energy loss dE/dx from CDC, ACC hit, and TOF information are used by the operation of the identification of charged pion and kaon (PID). ECL are CsI(Tl) crystal scintillation calorimeters. KLM, layers of resistive plate counters instrumented on the iron flex return, identify K_L or muon.

A major detector upgrad in the summer of 2003. A 3-layer SVD with a 2 cm radius beam-pipe was used until the summer of 2003 for the $152 \times 10^6 B\bar{B}$ paris. In the summer of 2003, a 4-layer SVD, a 1.5 cm radius beam-pipe, and small-cell inner drift chamber were installed. The following sub-chapters provide a more detailed description of every sub-detector.

2.2.1 Silicon Vertex Detector (SVD)

The Silicon Vertex Detector (SVD) [25, 26] provides the information of interaction point position and finds the charged particle tracks together with CDC mentioned after. To provide precise B decay vertex, SVD is required that have high precision for z axis. And due to close by beam-pipe, SVD is made highly radiative resistant. SVD is composed of Silicon detectors based on the $p - n$ junction diodes operated at reverse bias. The ionization currents caused by particle passing through the depleted region are detected and measured.

SVD has upgraded at summer of 2003, SVD1 [25] to SVD2 [26]. SVD1 configuration is shown at Fig 2.3. SVD1 has 3-layer structure and radius of each layer is 30, 45.5, 60.5 mm.

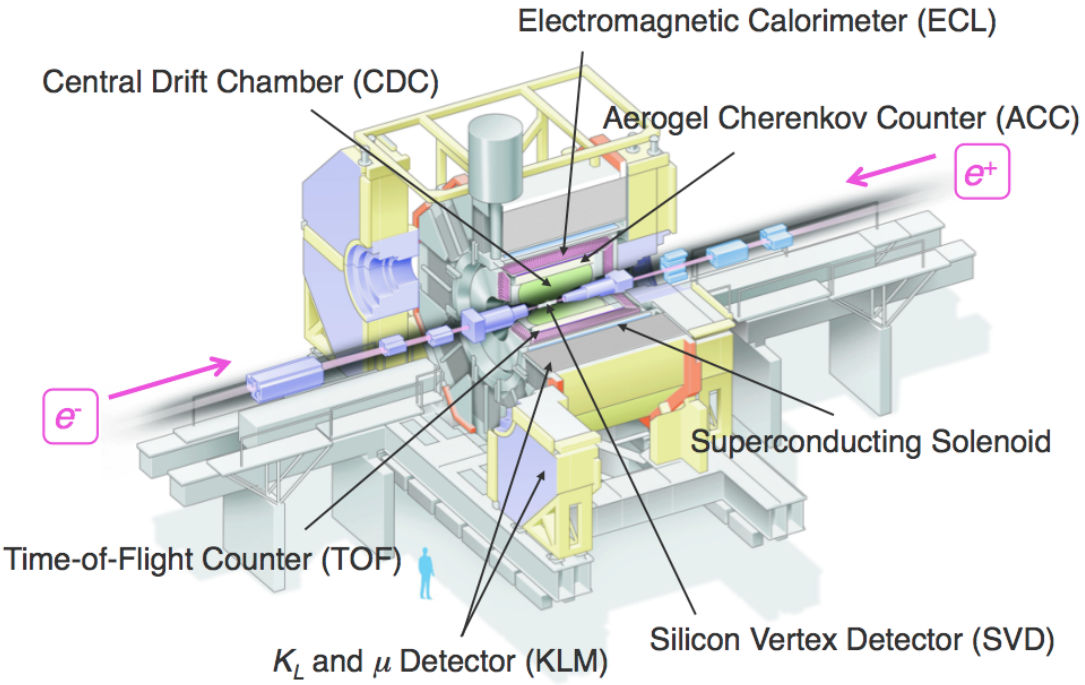

Figure 2.2: Belle Detector

It consists of three layers in barrel-only designed and covers a solid angle $23° < \theta < 139°$ where θ is the angle from the beam axis. Each layer is composed by independent 8, 10, 14 ladder. One ladder has double-sided silicon strip detectors (DSSDs). In SVD1 total, 102 DSSDs are used.

The impact parameter resolution $\sigma_{r\phi}$ and σ_z measure using cosmic rays are Fig 2.4, and well represented by the following formula:

$$\sigma_{r\phi} = 19 \oplus 50/(p\beta \sin^{3/2}\theta)\ \mu\text{m}, \sigma_z = 36 \oplus 42/(p\beta \sin^{5/2}\theta)\ \mu\text{m}. \tag{2.3}$$

The upgraded SVD2 (configuration is shown as Fig 2.5)has four layers, where 6, 12, 18 ladders. It has larger coverage of $17° < \theta < 150°$, which corresponds to 92% of the full solid angle. VA1TA integrated circuits are used in SVD2 readout electronics, which have excellent radiation tolerance of more than 20 Mrad. The impact parameter resolutions are

$$\sigma_{r\phi} = 21.9 \oplus 35.5/(p\beta \sin^{3/2}\theta)\ \mu\text{m}, \sigma_z = 27.8 \oplus 31.9/(p\beta \sin^{5/2}\theta)\ \mu\text{m}. \tag{2.4}$$

The SVD upgrade significantly improved the impact parameter resolution in both the $r - \phi$ and z coordinates.

Information of vertex is needed, especially charged particle track selection in this study. And also effective for backgrounds rejection of the reconstruction of $K_S \to \pi^+\pi^-$ because of non-zero flight length of K_S.

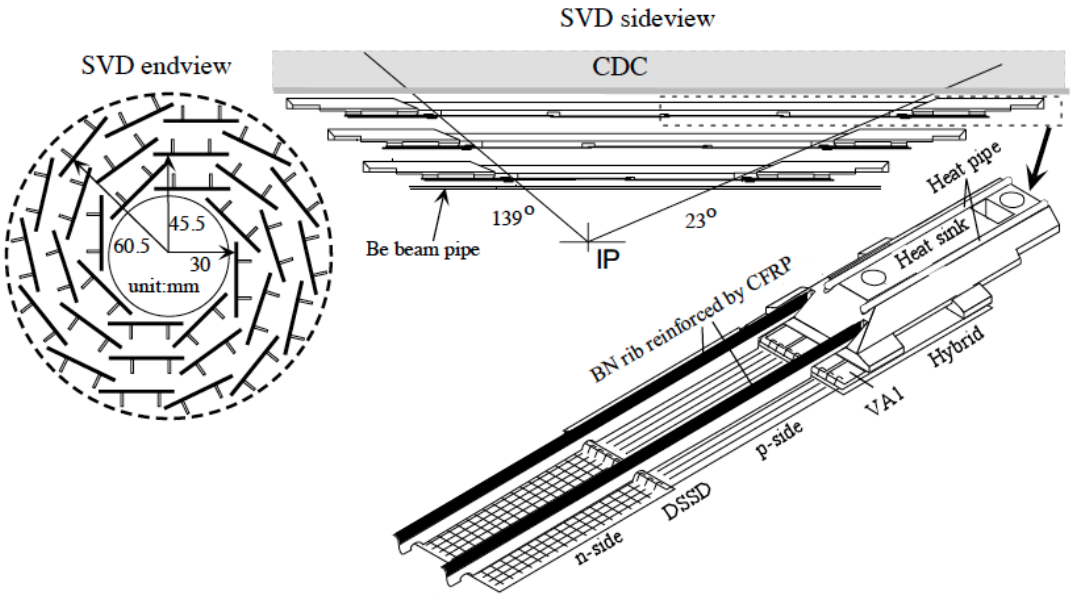

Figure 2.3: SVD1

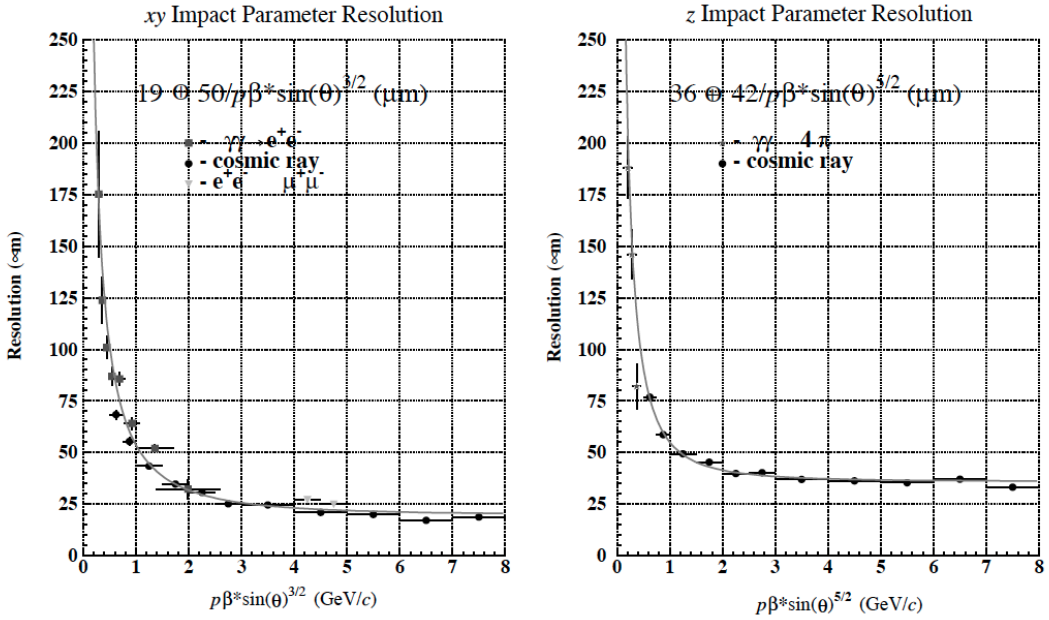

Figure 2.4: SVD impact parameter resolution

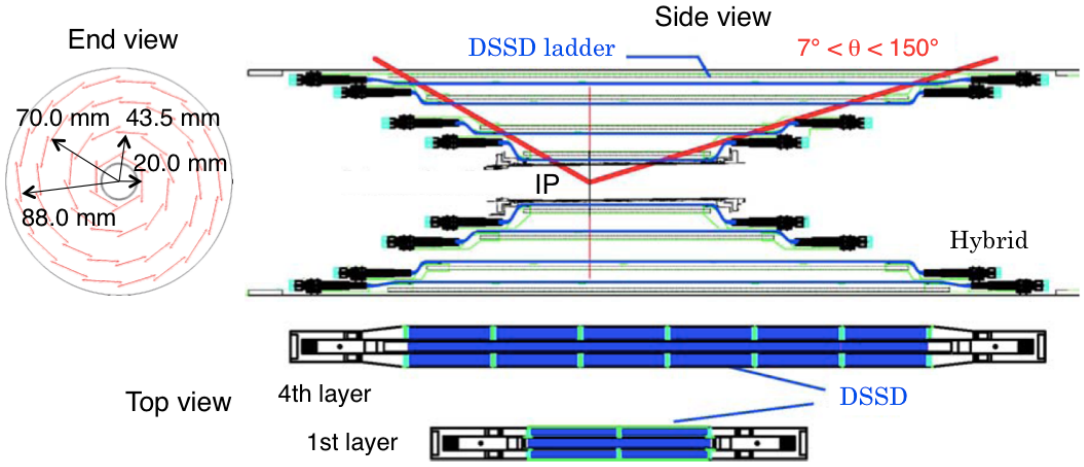

Figure 2.5: SVD2

2.2.2 Central Drift Chamber (CDC)

The Central Drift Chamber [27] measures the charged particles tracking. To obtain the momentum, CDC determines their curvature in the magnetic field of 1.5 T provided by the superconducting solenoid. Additional important information is the energy deposit dE/dx usable for the particle identification.

Figure 2.6 shows CDC configuration. CDC coverage is $17° < \theta < 150°$ with asymmetric structure in z direction. CDC has 50 cylindrical layers of anode wires and 8400 drift cells. Their is composed in 32 parallel to z axis layers ("axial wires") and 18 slanted off the z axis layers ("stereo wires") for the improvement of measurements z direction resolution. In summer of 2003, the inner three layers are replaced by two small-cell layers for making a space of SVD2, maintaining the performance of the trigger. The total number of drift cell is change 8400 $\rightarrow$ 8464.

The position resolution for track of charged particles near the center of drift space is $\sim$ 100 μm. The transverse momentum resolution measures using the cosmic ray as

$$\frac{\sigma_{p_t}}{p_t}(\%) = 0.19 p_t \oplus 0.30/\beta, \tag{2.5}$$

and shown as Fig. 2.7. The charged particle momentum is obtained from

$$p[\mathrm{GeV/c}] = 0.3 \cdot B[\mathrm{T}] \cdot \rho[\mathrm{m}], \tag{2.6}$$

here B is magnetic field. ρ is radius of track of one. Figure 2.8 shows a scatter plot on dE/dx and particle momentum. dE/dx is expected

$$dE/dx = \left(\frac{e^2}{4\pi\epsilon^0}\right)^2 \frac{4\pi N_A}{m_e c^2} \frac{\rho Z}{A} \frac{1}{\beta^2} \left(\ln\left(\frac{2m_e c^2 \gamma^2 \beta^2}{I^2}\right) - \beta^2 - \frac{\delta}{2}\right), \tag{2.7}$$

here ρ, A, Z and N_A are material density, atomic mass, atomic number and Avogadro's number. Clear separation between pions and kaons are obtained on a momentum range up to $\sim$ 1 GeV.

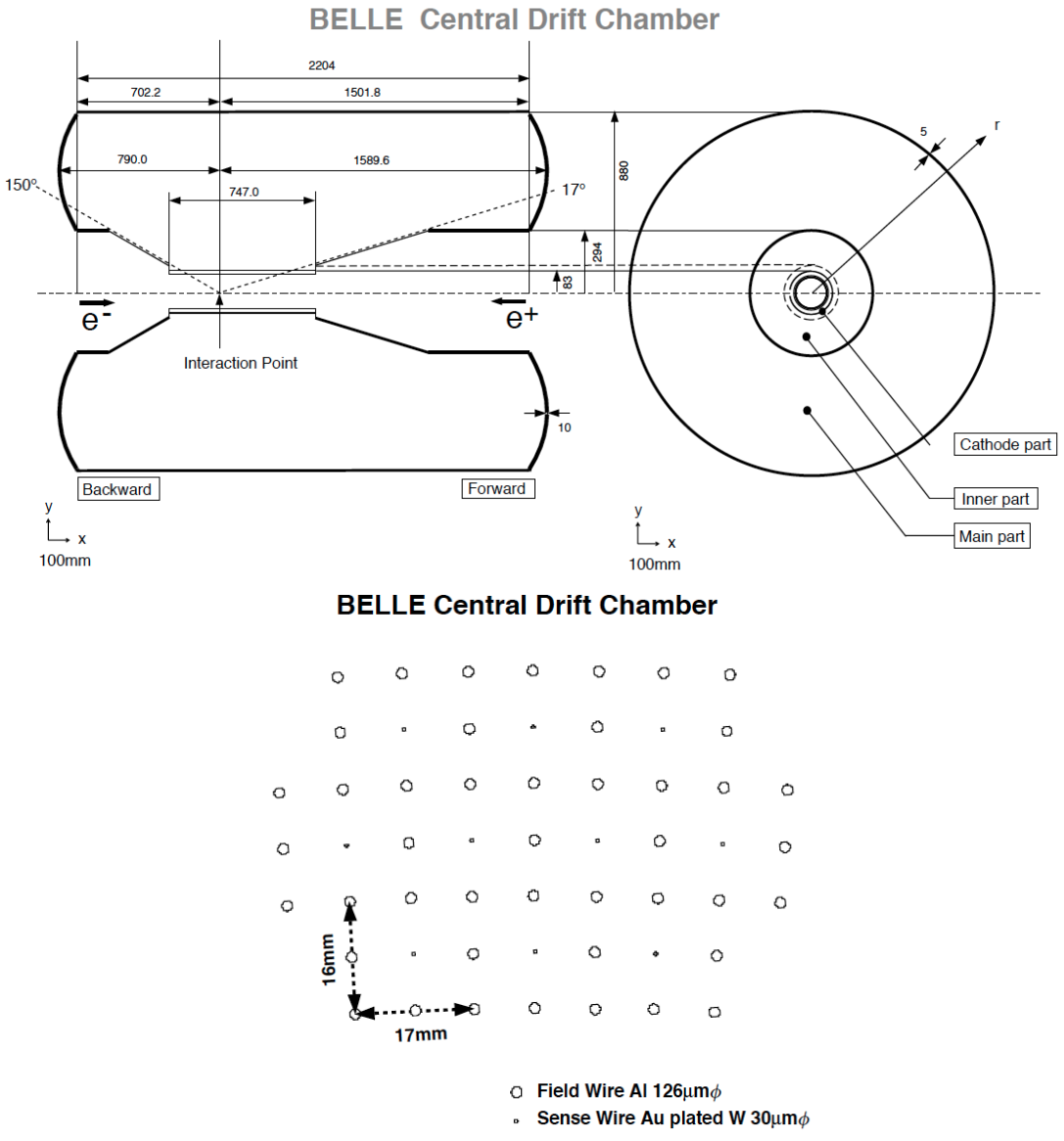

Figure 2.6: CDC configuration

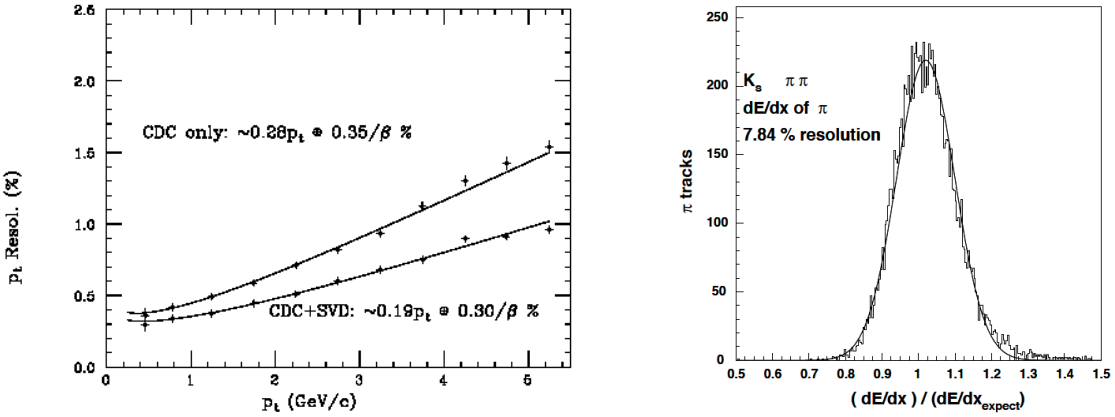

Figure 2.7: CDC resolution

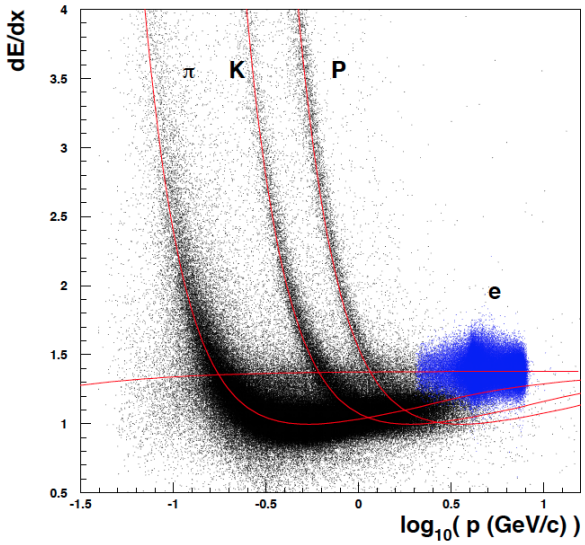

Figure 2.8: dE/dx

In this study, momentum of charged particles are obtained from CDC information. CDC permit us to perform analysis using charged track kinematics. One of the most important observable, Dalitz parameters $m_{K^0_S\pi^\pm}$ are calculated from momentum of particles. Also identification of particle use dE/dx from CDC in low (< 1 GeV) and very high (> 3 geV) momentum region, (this detail is described below Sec.2.3).

2.2.3 Aerogel Cherenkov Counter (ACC)

Aerogel Cherenkov Counter (ACC) provides the information to identification of charged particle pions or kaons at high momentum range (1.2 GeV/$c < p < 3.5$ GeV/c). ACC is silica aerogel threshold Cherenkov counter, which detect Cherenkov light a particle emit or not, and distinguishes it particle speed is faster or not than the velocity of light in that medium. The condition to emit Cherenkov light is given as

$$n > \frac{1}{\beta} = \sqrt{1 + (\frac{m}{p})^2}, \tag{2.8}$$

where, m, p and β are particle mass, momentum and velocity, n is the refractive index of the matter.

The identification of charged Kaons and pions (PID) are very important for studying B meson decay. ACC particle identification are applied momentum range of $1.2 < p < 3.5$ GeV/c and $17^\circ < \theta < 127^\circ$ solid angle. Figure 2.9 shows ACC configuration. Aerogels with the refractive indices from 1.01 to 1.03 depending on θ angle are used. The choice of the refractive index for the barrel ACC is optimized for separation of high momentum pions and kaons from the two-body B decay, such as $B \to \pi\pi$ and $K\pi$. For and-cap ACC aerogel, due to absent of TOF, $n = 1.030$ for low momentum aerogel is used. The fine-mesh photomultiplier tubes (FM PMTs) are attached to the aerogels, for operating in 1.5 T magnetic field. ACC is composed 960 counter modules segmented into 60 cells for the barrel part and 228 modules arranged for end-cap part. Five aerogel tiles are stacked in thin (0.2 mm thick) aluminum box of $12 \times 12 \times 12$ cm^2.

The performance of the ACC [28] is checked by using $D^{*-} \to \bar{D}^0\pi^-$ followed by $\bar{D}^0 \to K^+\pi^-$ decay. The slow π from D^* allows to identify the K and π from D decay. Figure 2.10 shows the distribution of the number of photoelectron, where the K/π separation is good and consistent with MC.

2.2.4 Time-of-Flight Counter (TOF)

The Time-of-Flight Counter (TOF) [29] provides particle identification for charged kaons and pions in momentum range < 1.2 GeV/c to measure the flight time. TOF is plastic scintillator with FM PMTs. The time of flight t and particle mass m are given by

$$t = \frac{l}{c\beta} = \frac{l}{c}\sqrt{1 + (\frac{m}{p})^2}, m = p\sqrt{(\frac{ct}{l})^2 - 1}, \tag{2.9}$$

where l is flight length here $l \sim 1.2$ m, β, p and m is particle velocity, momentum and mass.

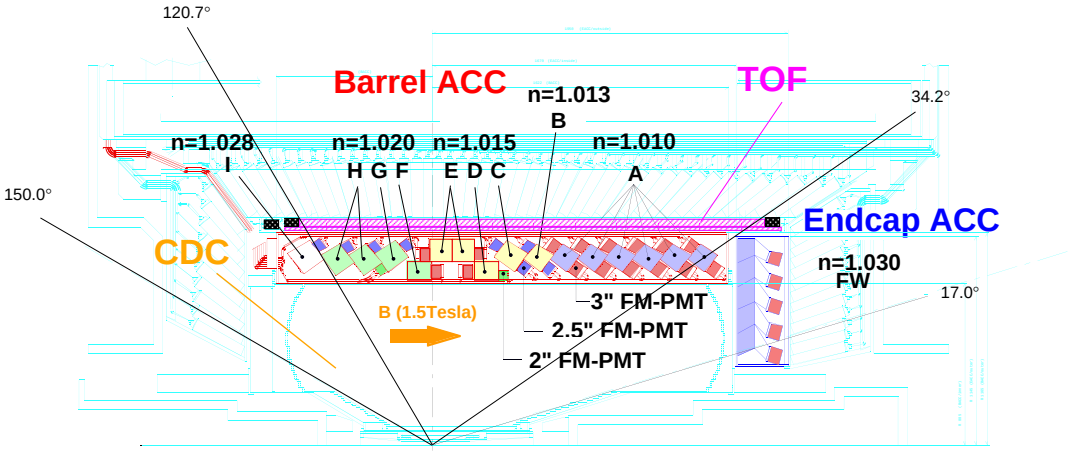

Figure 2.9: ACC configuration

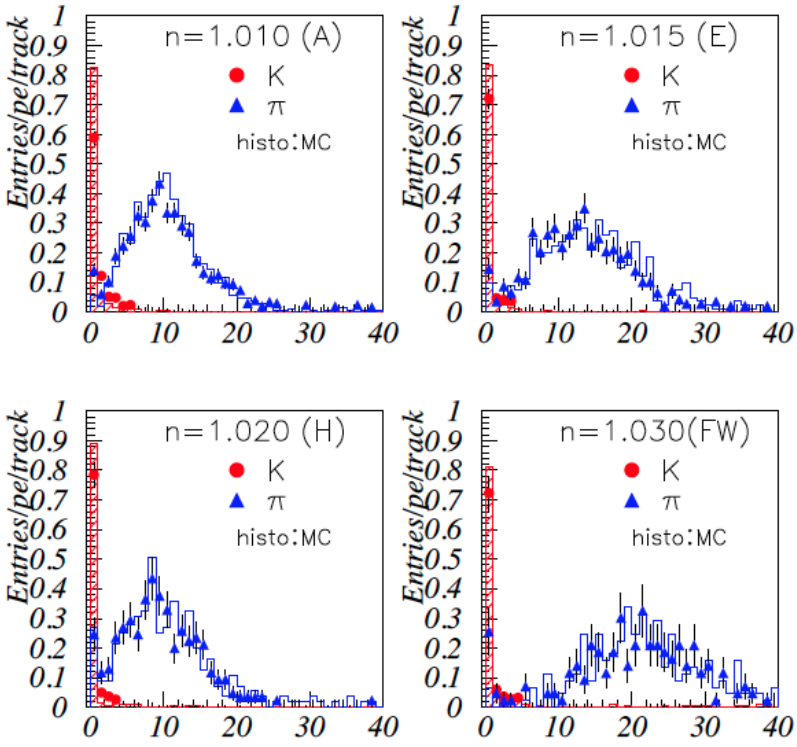

Figure 2.10: ACC pid

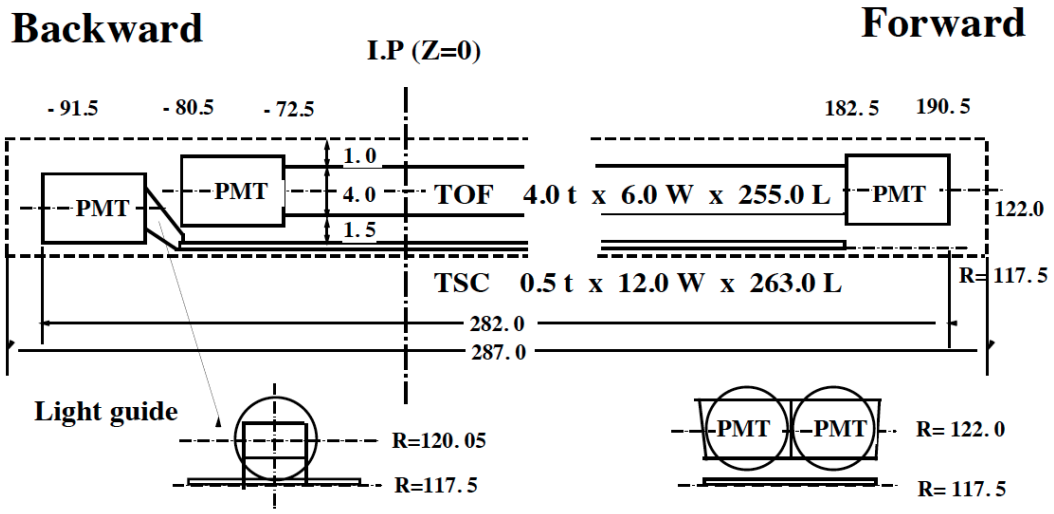

Figure 2.11: TOF configuration

Figure 2.11 shows TOF configuration. TOF is composed 128 TOF counters and 64 thin trigger scintillation counters (TSCs). TSC is used for keeping the fast trigger rate below 70 kHz. There are located at a 1.2 m from IP, covering the barrel part $34° < \theta < 120°$.

By the measurements with weighted on forward and backward FM PMTs, the TOF time resolution is $\sim$ 100ps. Figure 2.12 shows the mass distribution obtained by TOF for particle $p < 1.2$ GeV$_c$. Clear peaks corresponding to pions, kaons and protons are seen.

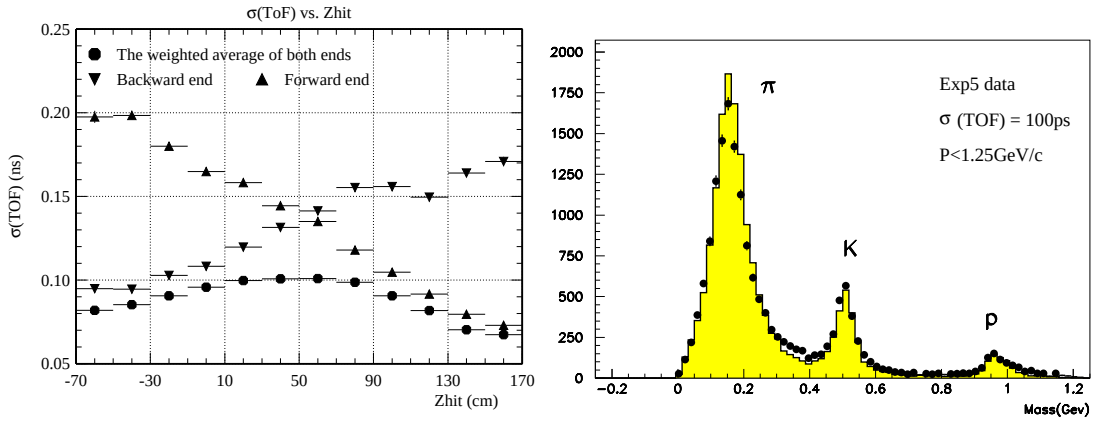

Figure 2.12: TOF resolution and mass distribution

Thanks to PID, in this study we can distinguish $B^0 \to DK^{*0}$ signal from other back-

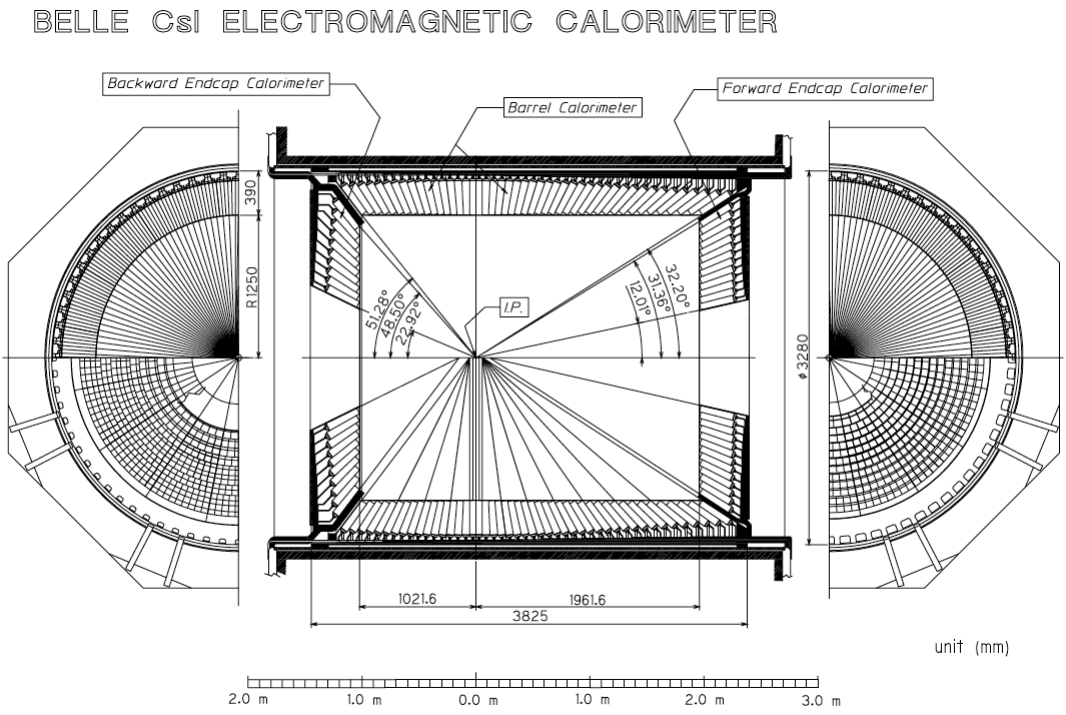

Figure 2.13: ECL configuration

ground decay modes. For example, possible backgrounds due to PID are $B^0 \to D\rho^0$, $B^0 \to D\pi^+\pi^-$ and so on. In those decays, D can be reconstructed from real D. So those background modes has some distribution on Dalitz plane.

2.2.5 Electromagnetic Calorimeter (ECL)

ECL [30] provides the information of energy and position of photon and electron. When electrons and photons enter in material, electromagnetic shower is occurred. ECL measures that shower energy deposition. A comparison with the momentum provides the identification of electrons.

Figure 2.13 shows ECL configuration. ECL is composed 8736 thallium dopes CsI crystal counters. Figure 2.14 shows one counter configuration. ECL consists three parts, one is barrel part composed 6624 crystal, radius $12.5 - 3.0$ m and $32.2° < \theta < 128.7°$ solid angle, two is forward part composed 1152 crystal, 2.0 m forward from IP and $12.4° < \theta < 31.4°$ solid angle, last is backward part composed 960 crystal, 1.0 m backward from IP and $130.7° < \theta < 155.1°$ solid angle.

The energy resolution obtained from beam test is

$$\frac{\sigma_E}{E}(\%) = \frac{0.066}{E} \oplus \frac{0.81}{\sqrt{4E}} \oplus \ (E \text{ in GeV}), \tag{2.10}$$

where the value is affected by the electronic noise (1st term), the shower leakage fluctuation

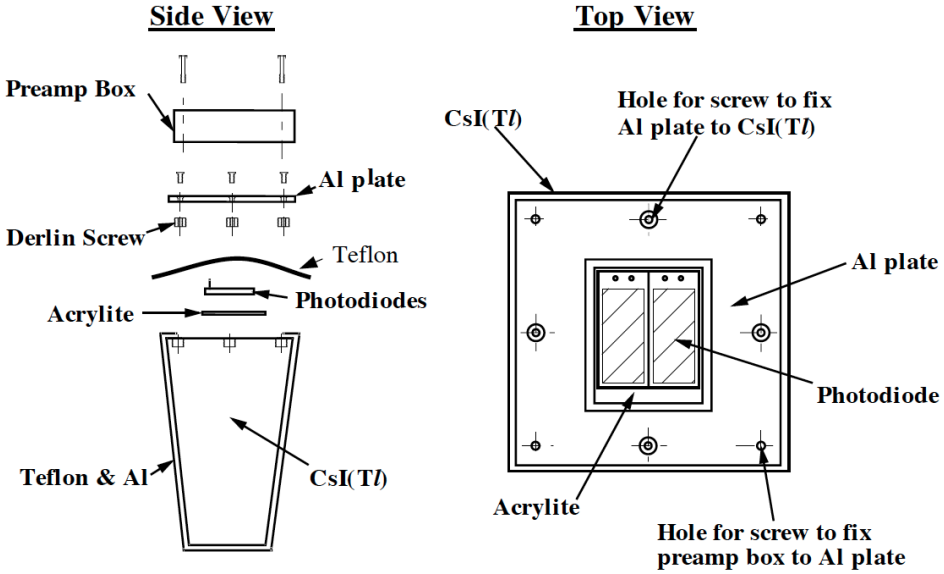

Figure 2.14: ECL counter configuration

(2nd and 3rd terms) and the systematic effect such as the uncertainty of calibration (3rd term). The spacial resolution is approximately found to be 0.5 cm/$\sqrt{E}$ (E in GeV).

2.2.6 K_L and Muon Detector (KLM)

K_L and Muon Detector [31] provide the identification of K_L and μ with high efficiency over a broad momentum range greater than 600 MeV/c. The KLM is composed alternately 4.7 cm thick 15(14) iron plates and charged particle detectors (resistive plate counters, RPCs) for barrel (end-cap) part. K_L can be identified by a product of shower in iron plate or ECL. Because μ is more penetrating, it go through out of all detector and hits in RPC. Other particles, such as pions and kaons are stopped in the inner detectors and can be easily separated from μ.

KLM covers $45° < \theta < 125°$ in barrel part only and $20° < \theta < 155°$ in total. Figure 2.15 shows KLM configuration. Resistive plate counters have two parallel plate electrodes separated with resistivity ($\geq 10^{10}$ Ωcm) separated by a gas-filled gap. An ionizing particle induces a streamer in the gas that results in a local discharge. The discharge generates a signal on external pickup strips, and the location and the time are recorded. The number of KL clusters per event is in good agreement with the prediction. Typical muon identification efficiency is 90% with a fake rate around 2%.

2.2.7 Extreme Forward Calorimeter (EFC)

Extreme Forward Calorimeter (EFC) [32] provide the information for luminosity in order to measure the energy of electron or photon in extreme forward and backward, no ECL coverage. EFC are located in 60 cm forward and 43.5 cm backward, and compose radiation

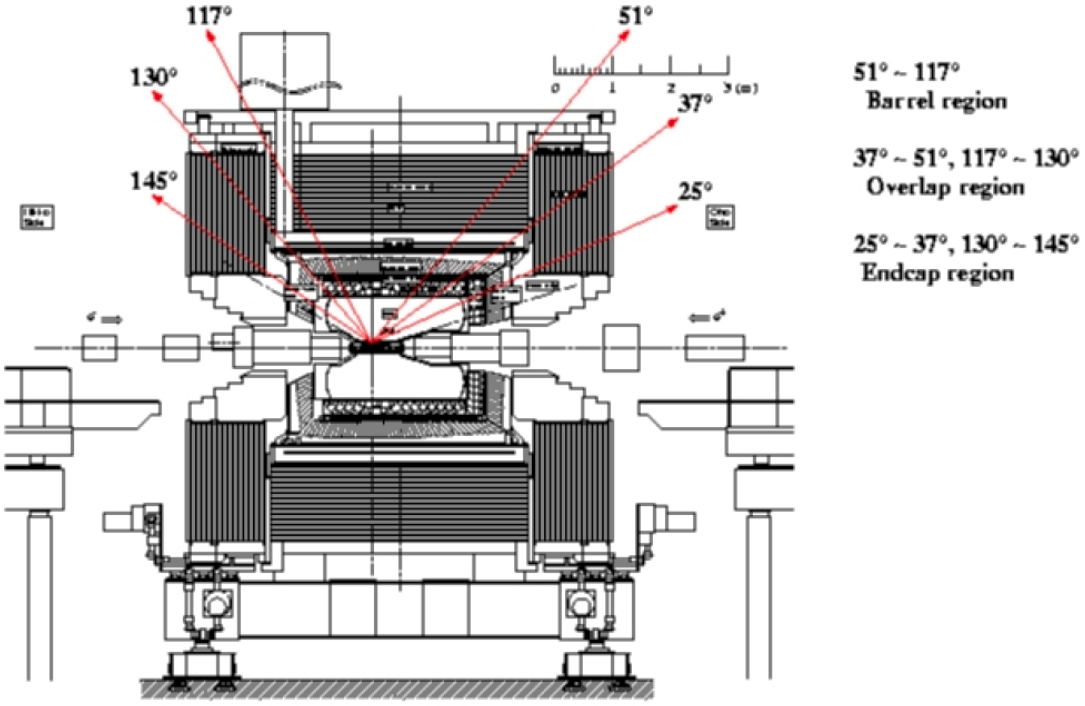

Figure 2.15: KLM configuration

resistant BGO ($Bi_4Ge_3O_12$) crystal. EFC coverage is $6.4° < \theta < 11.5°$ for forward, and $163.3° < \theta < 171.2°$ for backward. EFC energy resolution is 7.3% at 8 GeV and 5.8% at 3.5 GeV.

2.2.8 Trigger and Data Acquisition

The cross-section of events of interest B meson are smaller than background events, for example $e^+e^- \to q\bar{q}$ ($q = u, d, s, c$), Bhabha scattering and so on. The trigger for probable signal events are needed. Belle trigger system is composed of hardware trigger and software trigger. Belle trigger schematic view is shown at Fig 2.17. Each CDC, TOF, ECL, KLM and EFC detector provide the trigger information based on tracks and energy. The trigger signal is delivered Global Decision Logic (GDL) [33]. GDL make a judgement to storage event or not, within 2.2 μsec from trigger informations.

Data acquisition (DAQ) is constructed as parallel system as shown in Fig 2.18 to reduce dead-time even if high trigger rate. Each detector deliver measured information to event builder, when it receives trigger signal. The event builder summarize those information from detectors as one event data. That event data is filtered by online computer farm and delivered to high speed magnetic tape device.

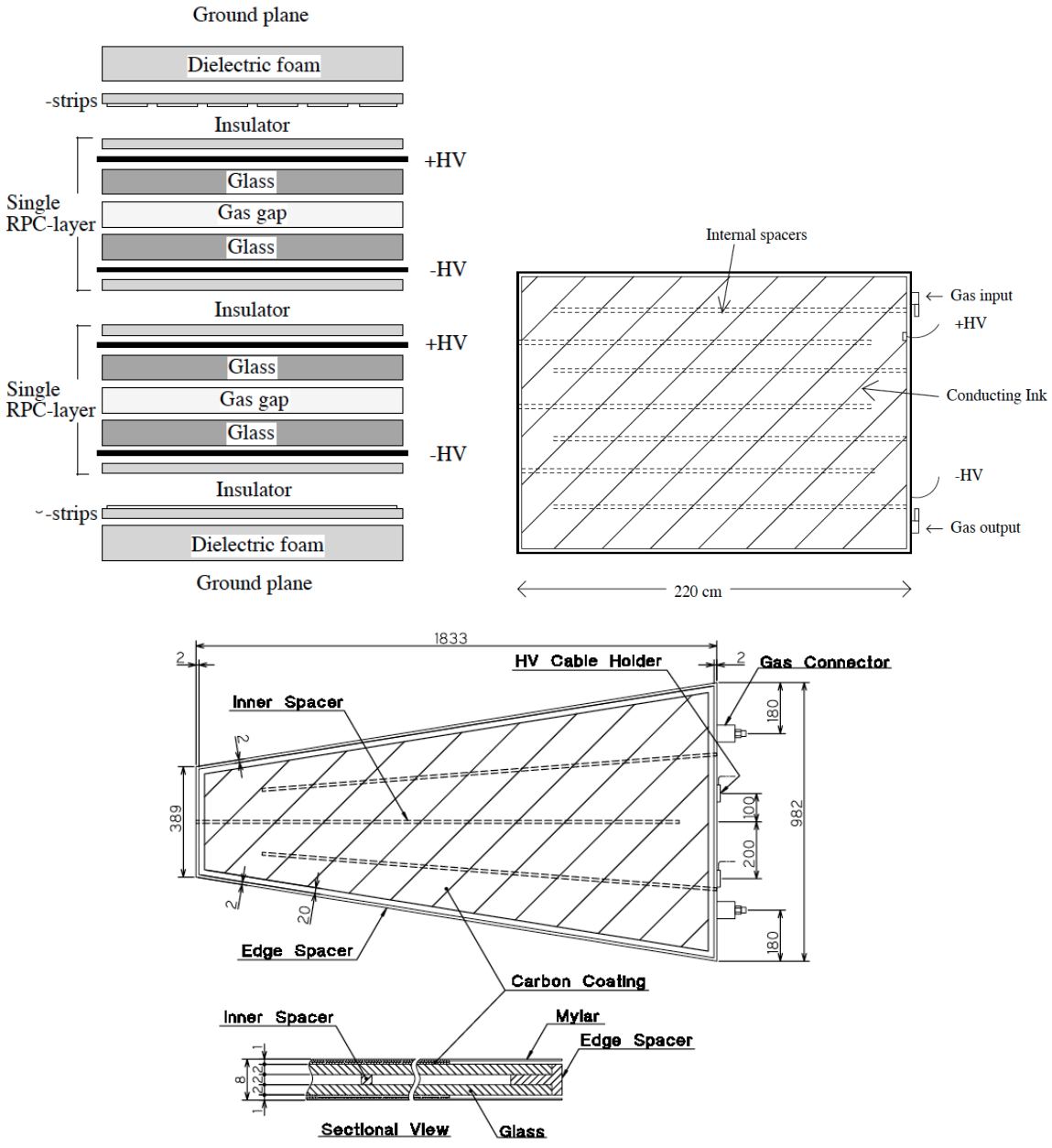

Figure 2.16: KLM component

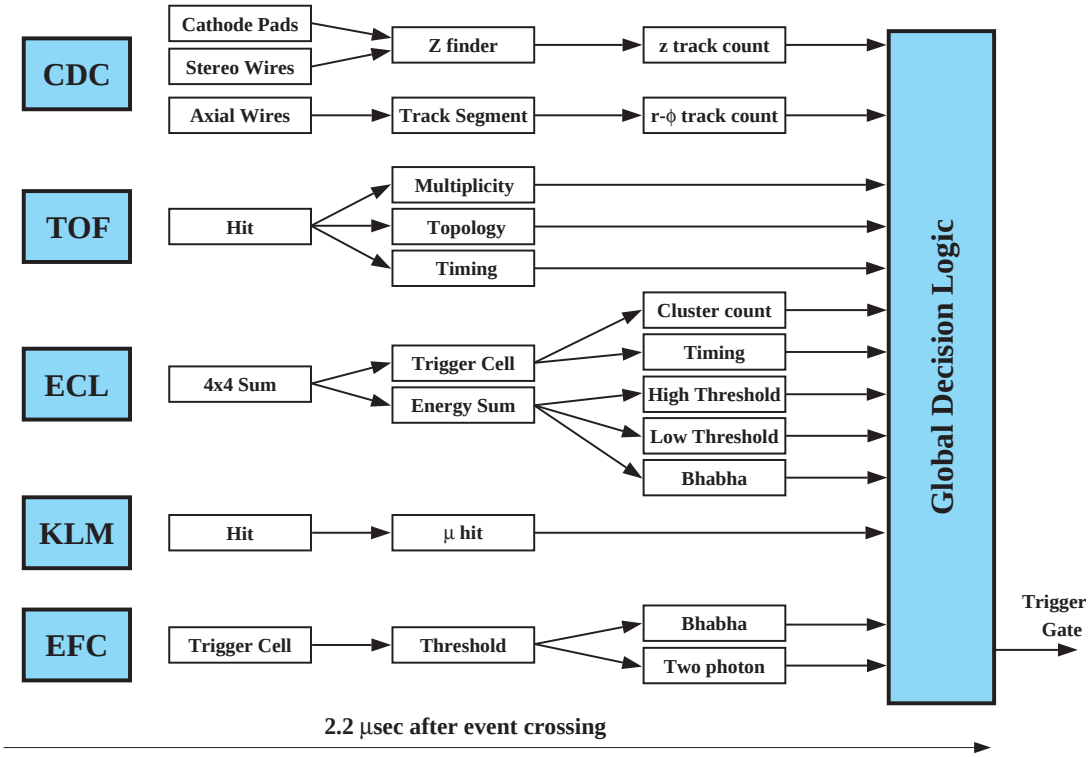

Figure 2.17: Trigger configuration

2.3 Particle Identification (PID) for $K^{\pm}/\pi^{\pm}$

In this section, particle identification (PID) for $K^{\pm}/\pi^{\pm}$ [34, 35] which is very important for our study is described. The $K^{\pm}/\pi^{\pm}$ PID are performed using the informations of ACC, TOF and dE/dx from CDC. Figure 2.19 shows the region of what detector is used for PID. The likelihood function for $K^{\pm}(\pi^{\pm})$ obtained from the three detectors (as shown in 2.8, 2.10 and 2.12) are combined to obtain the kaon (pion) likelihood $\mathcal{L}_K(\mathcal{L}_\pi)$. The likelihood ratio $P(K/\pi)$ is calculated as

$$P(K/\pi) = \frac{\mathcal{L}_K}{\mathcal{L}_K + \mathcal{L}_\pi}. \tag{2.11}$$

The PID performance is checked by using the decay $D^{*+} \to D^0\pi^+$ followed by $D^0 \to K^-\pi^+$. Figure 2.20 shows the relation of $P(K/\pi)$ and particle momentum. The clear separation up to 4 GeV can be seen.

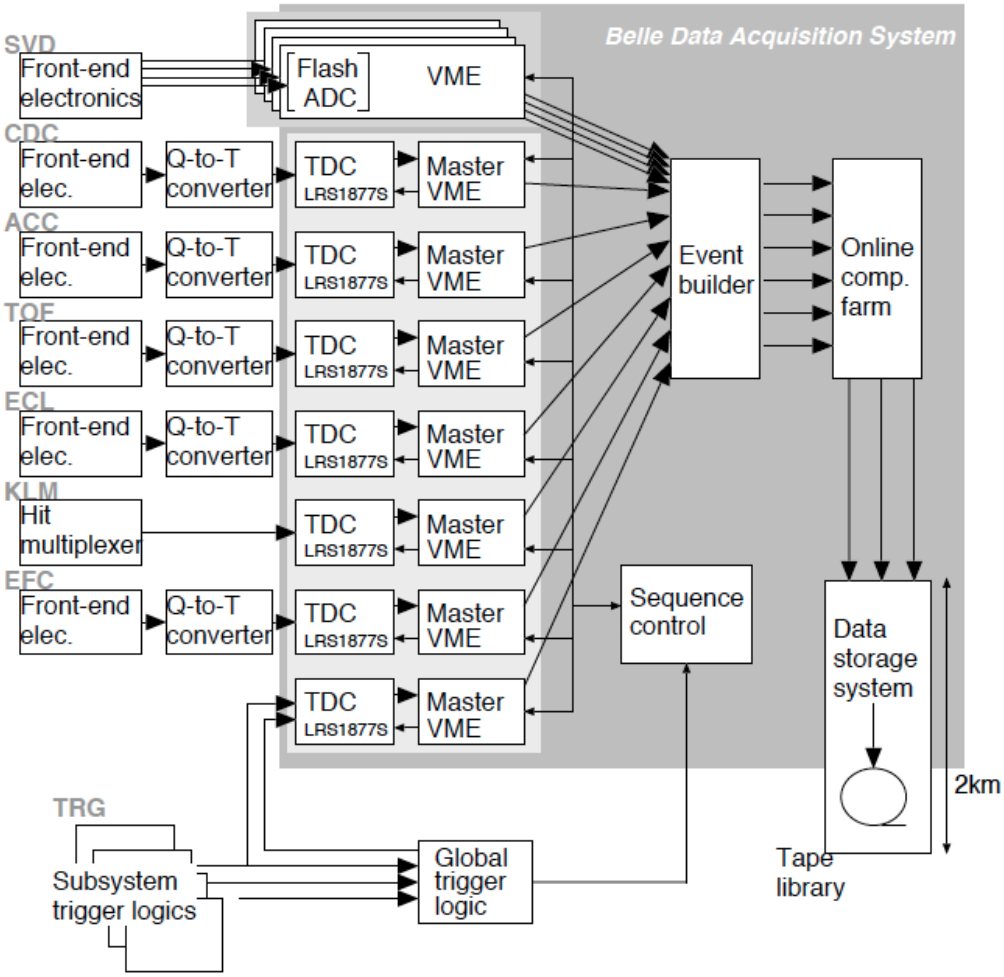

Figure 2.18: DAQ

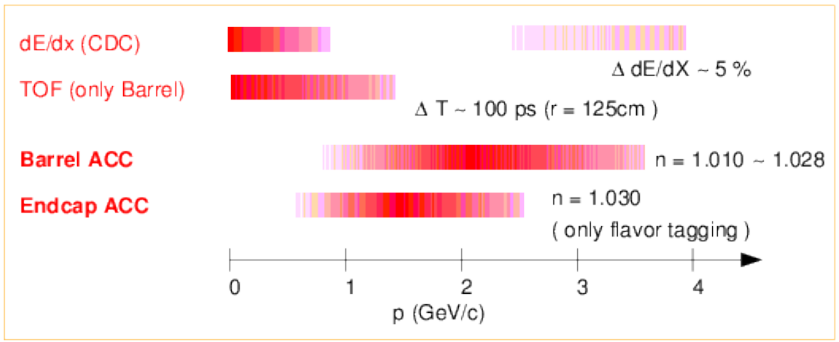

Figure 2.19: PID coverage

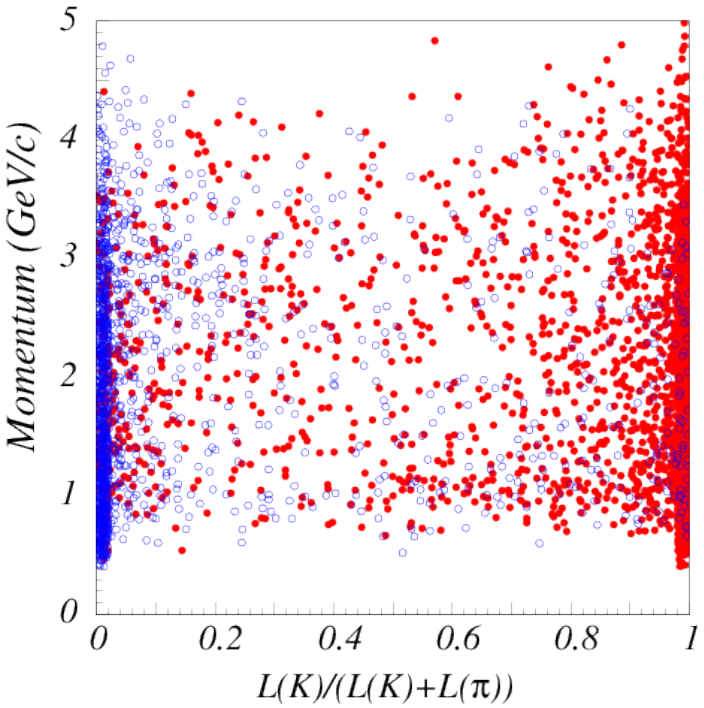

Figure 2.20: PID and momentum

Chapter 3

Analysis

3.1 Analysis Procedure

From this chapter, we explain the analysis procedures in order. This study uses N_i which is the event number of $B^0 \to DK^{*0}$ decay in "i"th binning on Dalitz plane (as shown in Fig 1.5 $m_{K_S\pi^+}$ and $m_{K_S\pi^-}$) to obtain the observables ($x_\pm$, $y_\pm$) which can be describe (ϕ_3, r_S, δ_S) physical parameters. At first, Table 3.1 shows the flowchart on this analysis.

3.2 Event Selection

We search for the signal B decay in the mode $B^0 \to [K^0_S\pi^+\pi^-]_D[K^+\pi^-]_{K^{*0}}$. The results are based on a 711 fb^{-1} reprocessed data sample.

3.2.1 Reconstruction of K^0_S Meson

K_S candidates are reconstructed from a pair of two oppositely-charged pions. K_S has some characteristic kinematics due to its comparative long life time. Also reconstructed K_S has background contribution from $\Lambda \to p\pi$ decay. We use 20 kinematics and detector information for neural network inputs to find K_S like events.

- For finding K_S like event
  - K_S momentum in lab. frame.
  - $z_{\rm dist}$: distance between two helices in z parallel of beam direction. K_S can have non-zero flight length because of its long life time.
  - flight length in vertical distance from beam x-y plane. K_S can have non-zero flight length because of its long life time.
  - angle between K_S momentum and K_S direction. If true K_S is reconstructed, this value should be near zero.
  - $dr_{\rm low}$: shorter distance between IP and helix. K_S can have non-zero flight length because of its long life time.

Event Selection	←	We select the signal decay events $B^0 \to [K^0_S\pi^+\pi^-]_D\,[K^+\pi^-]_{K^{*0}}$. Simultaneously, signal B is reconstructed. Here, some distinguishing backgrounds are vetoed.
⇓		
Discrimination of $q\bar{q}$ Background	←	In reconstructed events, there is certainly large contribution from $q\bar{q}$ backgrounds. In this section, we explain how to discriminate signal and this backgrounds.
⇓		
Probability Density Function	←	From obtained events, we use signal distribution on some parameters which is independent of Dalitz parameters. In this section, we explain how to obtain signal and other backgrounds distributions.
⇓		
Signal Extraction Projected for All Dalitz Region	←	We can check the total signal number.
⇓		
Control Sample Study	←	We check validation on $(x,\, y)$ fitter with the real data. We use $B^+ \to D\pi^+$ decay mode which has almost common kinematics as the signal.
⇓		
$(x,\, y)$ Fit on Pseudo-Experiments	←	We check validation on $(x,\, y)$ fitter with the total signal number which is estimated on above.
⇓		
Statistical Uncertainty	←	In this chapter, way to estimate statistical uncertainty is explained. Statistical uncertainty on $(x,\, y)$ is estimated by scanning on true values $(x,\, y)_{\rm true}$ with pseudo-experiments. In this study, before data fit, we consolidate way to estimate systematic uncertainty.
⇓		
$(x,\, y)$ Fit on Real Data	←	(Chapter 4) In this chapter, we obtain $(x_\pm,\, y_\pm)$ values.
⇓		
Systematic Uncertainty	←	In this chapter, we describe about systematic uncertainty on $(x_\pm,\, y_\pm)$.
⇓		
Physical Parameter Extraction	←	In this chapter, we perform the transformation $(x_\pm,\, y_\pm) \to (\phi_3,\, r_S,\, \delta_S)$.

Table 3.1: The flowchart of this study.

- $dr_{\rm high}$: longer distance between IP and helix. K_S can have non-zero flight length because of its long life time.
- angle between p_{K_S}(lab.) and $p_\pi(K_S)$. If true K_S is reconstructed, daughter pion decays to isotropic because of zero spin of K_S.
- SVD information of positive child.
- SVD information of negative child.
- CDC axial wire hit number of positive child.
- CDC stereo wire hit number of positive child.
- CDC axial wire hit number of negative child.
- CDC stereo wire hit number of negative child.

- For veto Λ event
  - particle identification (PID) (π, p) of positive child (21 bin).
  - PID (π, p) of negative child (21 bin).
  - m_Λ.
  - momentum of positive child.
  - momentum of negative child.
  - $\sin\theta$ (mom. direction) of positive child.
  - $\sin\theta$ of negative child.

As performance of this finder, reconstructed K_S purity is 92.2 %, and K_S reconstructed efficiency is 75.1 %.

3.2.2 Reconstruction of D Meson

The D meson is reconstructed by combining two oppositely-charged pion tracks and one K_S trajectory. We require $LR(K/\pi) = L_K/(L_\pi + L_K) < 0.6$ for π, here L_K (L_π) is kaon (pion) likelihood based on ionization energy loss dE/dx (measured by CDC), time of flight (TOF) and Cherenkov light yield (ACC). And also its charged track required to have a point of closest approach to the beam line within $\pm$ 5 mm of the interaction point in the direction perpendicular to the beam axis (dr) and $\pm$ 5 cm in the direction parallel to the beam axis (dz), which requirement means that track used reconstruction comes from origin of beam collision. The D candidate is required to have an invariant mass to be within 0.015 GeV/c^2 of the nominal D mass as shown in Figure 3.1. The fake events mean that reconstructed D is not real D, random combination of $K_S\pi^+\pi^-$ accidentally comes in the mass of D. To improve the momentum determination of B meson, tracks from D candidates are refitted constraining the invariant mass to the nominal D mass.

We check D mass selection significance as a function of $x \equiv |m_{D^0} - M_{K_S\pi\pi}|$ as shown Fig. 3.2.

$$\text{Significance} = \frac{N_{\rm sig.}}{\sqrt{N_{\rm sig.} + N_{\rm BG}}} \tag{3.1}$$

We check D selection in signal region varying x of selection. Signal region is defined by $|\Delta E| < 0.03$, $|m_{B^0} - M_{bc}| < 0.008$, $\mathcal{NB}^{\mathrm{TRANS}} > 5$, those parameters are defined below. Significance has a maximum at $x \sim 10$ MeV, however significance at 15 MeV agrees within error. In this analysis, poor signal number raises instability in (x, y) fit. I employ $|m_{D^0} - M_{K_S\pi\pi}| < 15\mathrm{MeV}/c^2$ selection.

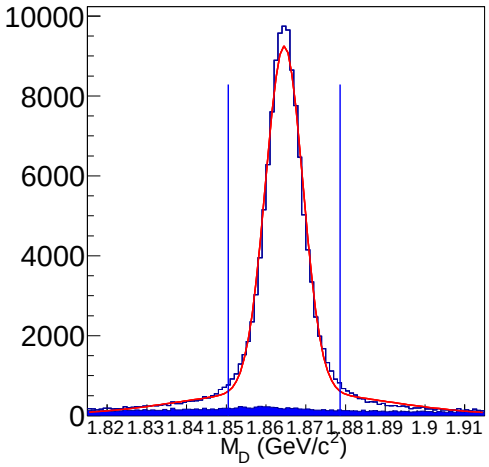

Figure 3.1: The distributions of $M(K\pi)$ for signal MC. The lines correspond to the requirement. Blue filled histogram is fake D events.

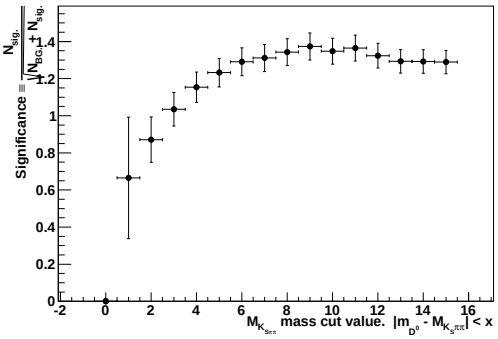

Figure 3.2: Significance of x of D mass selection for MC in signal region. Here signal region is defined by $|\Delta E| < 0.03$, $|m_{B^0} - M_{bc}| < 0.008$, $\mathcal{NB}^{\mathrm{TRANS}} > 5$. ($\Delta E$, m_{bc}, $\mathcal{NB}^{\mathrm{TRANS}}$) are described below, and they are parameters to distinguish signal and backgrounds.

3.2.3 Reconstruction of K^{*0} Meson

The K^{*0} meson is reconstructed by combining two oppositely-charged kaon and pion tracks. We require $LR(K/\pi) > 0.7$ for K and $LR(K/\pi) < 0.6$ for π. And also its charged

track required to have a point of closest approach to the beam line within ± 5 mm of the interaction point in the direction perpendicular to the beam axis (dr) and ± 5 cm in the direction parallel to the beam axis (dz). The K^{*0} candidate is also required to have an invariant mass to be within 0.050 GeV/c^2 of the nominal K^{*0} mass as shown in Figure 3.3, which corresponds to $\pm \sim 1\Gamma$ with Γ denoting the full width at half maximum of mass width. To use K^* higher resonance interference term k from Ref. [36], we decide K^{*0} mass selection as $|m_{K^{*0}} - M_{K\pi}| < 0.050$ GeV/c^2.

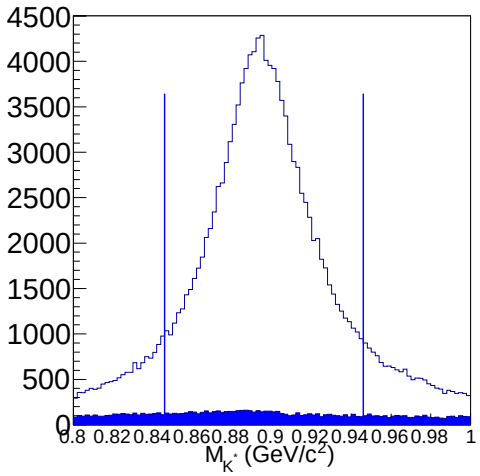

Figure 3.3: The distributions of $M(K\pi)$ for signal MC. The lines correspond to the requirement. Blue filled histogram is fake K^{*0} events.

3.2.4 Reconstruction of B^0 Meson

We reconstruct the B^0 candidate by combining a D candidate and a K^{*0} candidate. In addition, we use two kinematic variables, the energy difference $\Delta E \equiv E_D + E_{K^{*0}} - E_{\rm beam}$ and the beam-energy-constrained mass $m_{\rm bc} \equiv \sqrt{E^2_{\rm beam} - (\vec{p}_D + \vec{p}_{K^{*0}})^2}$ here $E_{D,K^{*0}}$ is the energy of the D, K^{*0} candidate and $E_{\rm beam}$ is the beam energy, all are evaluated in the e^+e^- center-of-mass (cm) frame. Figure 3.4 shows the distributions of ΔE and $m_{\rm bc}$. The fake signal, self cross-feeds define that the reconstructed events which decays to signal mode but is reconstructed with combinatorial swapping π from D and K^*, or tag-side B, and so on.

Self cross-feed events can have wrong Dalitz parameter information. And also detector resolution and radiative correction from charged tracks cause migration on binning of Dalitz plane. We evaluate those cross-feed between bin of Dalitz plane with MC sample, detail of it is described at Section 3.6.2.

Due to combination of tracks, we may reconstruct multiple B in one event. For those multiple candidates, we choose the best candidate on the minimum value of difference between measured and nominal values of $m_{\rm bc}$. The reduction of the detection efficiency due to the best candidate selection is 7.0%.

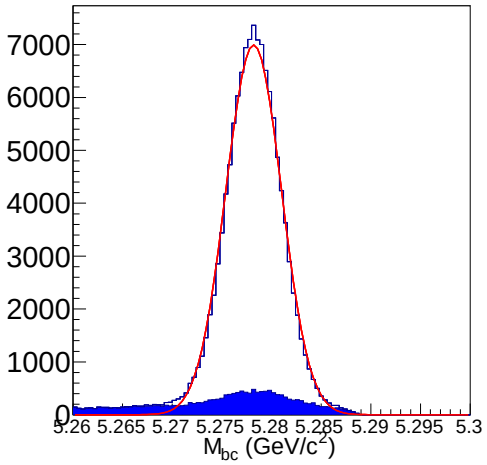

(a) The distributions of $m_{\rm bc}$ for signal MC.

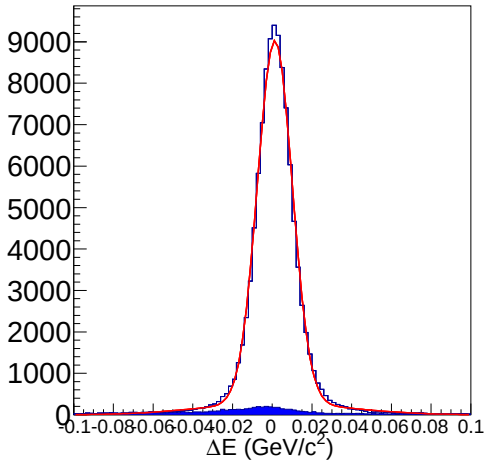

(b) The distributions of ΔE for signal MC.

Figure 3.4: The distribution of $m_{\rm bc}$ and ΔE for signal MC. Blue filled histogram is fake B self cross-feed events.

3.2.5 Rejection of Backgrounds

We have a background contribution from $[K^+\pi^-\pi^-]_{D^-}[K^0\pi^+]_{K^{*+}}$ in reconstructed signal events, which has the same final state and can peak in the signal window. In order to reject this background, we veto the events that satisfy $|M_{K^{*0}\pi^-} - 1.870| > 0.004$ GeV/c^2. In Figures 3.5, the distributions of $M_{K^{*0}\pi^-}$ for signal and background are shown. We will estimate the number of remaining background events by fitting the MC sample. The relative loss of signal efficiency by this requirement is 0.6%.

There is large contribution from the decay $D^{*\pm} \to D\pi^\pm$ in $e^+e^- \to c\bar{c}$. For removing this, we use a variable ΔM defined as the mass difference between the $D^{*\pm}$ and D candidates, here the $D^{*\pm}$ meson is reconstructed from the D candidate used in the B reconstruction and the $\pi^\pm$ not used in the B reconstruction. Those real D backgrounds have strong tendency to be mis-reconstructed as signal B. They can cause some bias due to structures on ΔE. To avoid this bias, we apply ΔM veto. We try all the pions to be combined, and select one for which the value of ΔM is closest to 0.142 GeV/c^2. For $\pi^\pm$, we apply no particle-identification requirement because of the characteristic low momentum of $\pi^\pm$ from $D^{*\pm}$ decay. By requiring $\Delta M > 0.15$ GeV/c^2, 14% of $q\bar{q}$ background (19% of $c\bar{c}$ background) and 11% of $B\bar{B}$ backgrounds are removed according to MC. The relative loss of signal efficiency is 5.5%. Figure 3.6 shows the ΔM distributions for signal and $q\bar{q}$ background.

To distinguish between the signal and the background from $e^+e^- \to q\bar{q}$ ($q = u, d, s, c$) continuum process, we use a neural network method based on 12 variables. For the output of neural network, named $\mathcal{NB}$, we apply a loose requirement $\mathcal{NB} > -0.6$, which retains 93.7% of the signal and removes 28.1% of the $q\bar{q}$ background remaining after the

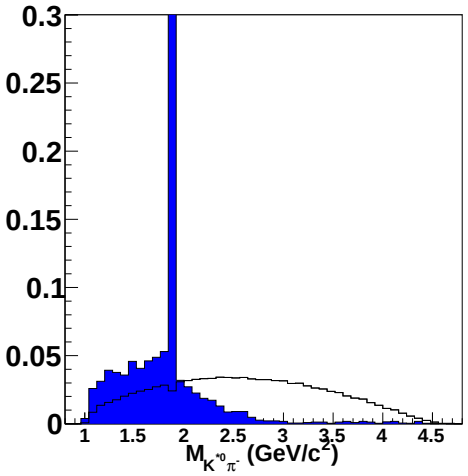

(a) The distributions of $M_{K^{*0}\pi^-}$ for the background $D^-_{K^+\pi^-\pi^-}K^{*+}_{K^0\pi^+}$ (blue) and the signal (white).

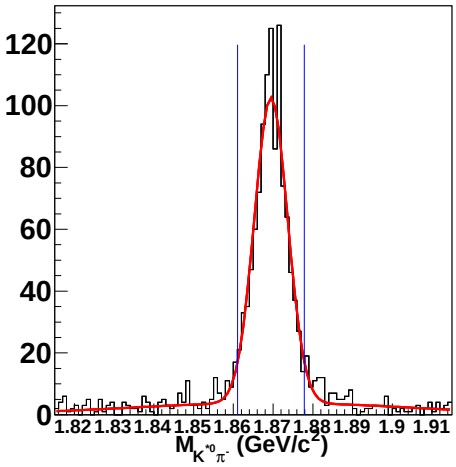

(b) The distributions of $M_{K^{*0}\pi^-}$ for the background $D^-_{K^+\pi^-\pi^-}K^{*+}_{K^0\pi^+}$ (the same as blue histogram of left plots). We veto inside of blue line.

Figure 3.5: The lines correspond to the requirement.

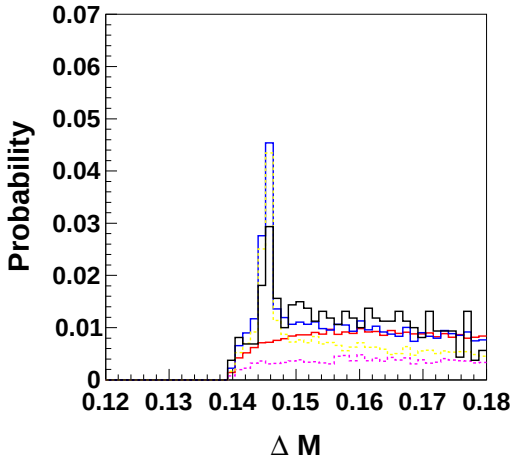

Figure 3.6: The distributions of ΔM for the signal (red), the $q\bar{q}$ background (blue, $q = c$ is yellow dashed and $q = u, d, s$ is magenta dashed) and the $B\bar{B}$ background (black). The histograms are obtained from MC.

requirement on ΔM, according to MC. The variable $\mathcal{NB}$ will be fitted for extracting the signal after a transformation described in Section 3.3.4. For details about $\mathcal{NB}$, see Chapter 3.3, here the distribution can be seen in Figure 3.8 (a).

3.3 Discrimination of $q\bar{q}$ Background

There is large contribution of the continuum background from the process $e^+e^- \to q\bar{q}$ ($q = u, d, s, c$). In this section, we describe a approach to discriminate between the signal and the background using a neural network method.

3.3.1 Introduction of Variables

Since the background $e^+e^- \to q\bar{q}$ plays a critical role to decrease the significance of our mode, we employ 12 variables to improve $q\bar{q}$ events suppression. In the following, we list these variables. These distributions on signal and background components are shown in Figure 3.7.

- LR(KSFW): the likelihood ratio obtained from the Fisher discriminants based on modified Super-Fox-Wolfram moments [37]. Standard KSFW package is used; thus such as the effect of the correlation to missing mass is included. The coefficients of Fisher discriminants are optimized using the signal and $q\bar{q}$ MC.

- $|\cos\theta_{\rm thr}|$: the absolute value of the cosine of the angle in CM frame between the thrust axis of the B decay and the one of the detected remainders. For the detected remainders, we use all the charged particles, for which the pion mass is assigned, and the gammas which have the energies larger than 0.1 GeV.

- Δz: the distance of the reconstructed and tag-side B vertices. For the signal event, the absolute value can be larger because of the longer life time of the B meson.

- Distance of D and K^{*0}: the distance of closest approach between the trajectory of the K^* candidate and the trajectory of the D candidate. The value is close to zero for the signal, while the value can be larger for the $c\bar{c}$ background, for which the K^{*0} meson can be secondary from the particle having longer life time.

- $|qr|$: the absolute value of the flavor tagging information qr [38], here q indicates the b-flavor and r indicates the quality of the tagging. We use the multi-dimensional-likelihood method (the standard method) for the tagging.

- $|\cos\theta_B|$: the absolute value of the cosine of the angle between the B-flight and the beam axes. The B meson tends to have perpendicular direction to the beam axis, while the $q\bar{q}$ background has random direction which makes the distribution about flat.

- $\cos\theta_B^D$: the cosine of the angle between the daughter D direction and the opposite direction to $\Upsilon(4S)$ in the B-rest frame.

- Z of $\mathrm{V_{all,1}}$: z component of sphericity vector of largest eigen-value.

- Cosine of $\mathrm{V_{sig,1}}$ $\mathrm{V_{oth.,1}}$: cosine of sphericity vector from signal and tag side of largest eigen-value.

- Cosine of $V_{sig,2}$ $V_{oth.,2}$: cosine of sphericity vector from signal and tag side of second largest eigen-value.
- Cosine of $V_{sig,3}$ $V_{oth.,3}$: cosine of sphericity vector from signal and tag side of smallest eigen-value.
- Magnitude of $Thrust_{oth.}$: magnitude of thrust from tag side.

3.3.2 NeuroBayes Method

For combining the parameters, we employ the NeuroBayes neural network package [39], which is a highly sophisticated tool for multivariate analysis of correlated data. We show the result of the output ($\mathcal{NB}$) of the training in Figure 3.8 (a). Figure 3.8 (b) shows the $\mathcal{NB}$ performance of cut-based analysis. We show the performance of cut-based analysis for the comparison. We do not use the cut-based but the fit for $\mathcal{NB}$. For details about the training, see Appendix A.

3.3.3 Contribution of Each Variable

As a check, we obtain the powers for individual variables as in Table 3.2, here the explanations of contents are the following.

- Only this: the significance for single parameter. The quantity is obtained as the correlation of a variable to the output multiplied by $\sqrt{n}$, here n is the sample size. The computation does not take into account other parameters.
- Without this: the significance loss when a parameter is removed. This is the loss of correlation multiplied by $\sqrt{n}$ when only one parameter is removed from the input set and the total correlation to the output is recomputed.
- Corr. to others: the linear-correlation factor of a parameter to all the others, computed with the complete correlation matrix.

On higher "Only this" for the parameters, for example LR(KSFW) has the highest value among 12 parameters, we can see distribution which have clearly-separated as shown in Fig 3.7 left-top. The values of "Only this" are higher for the variables which have the distributions clearly different between the signal and the background. The value of "Without this" is related to the value of "Only this", becoming lower if the value of "Corr. to others" is higher. For "Only this" and "Without this", the relative magnitudes have meanings. All values are the standard outputs from the NeuroBayes package obtained from the correlations of the variables. The Values in Table 3.2 make sense according to the distributions in Figure 3.7 and the definitions.

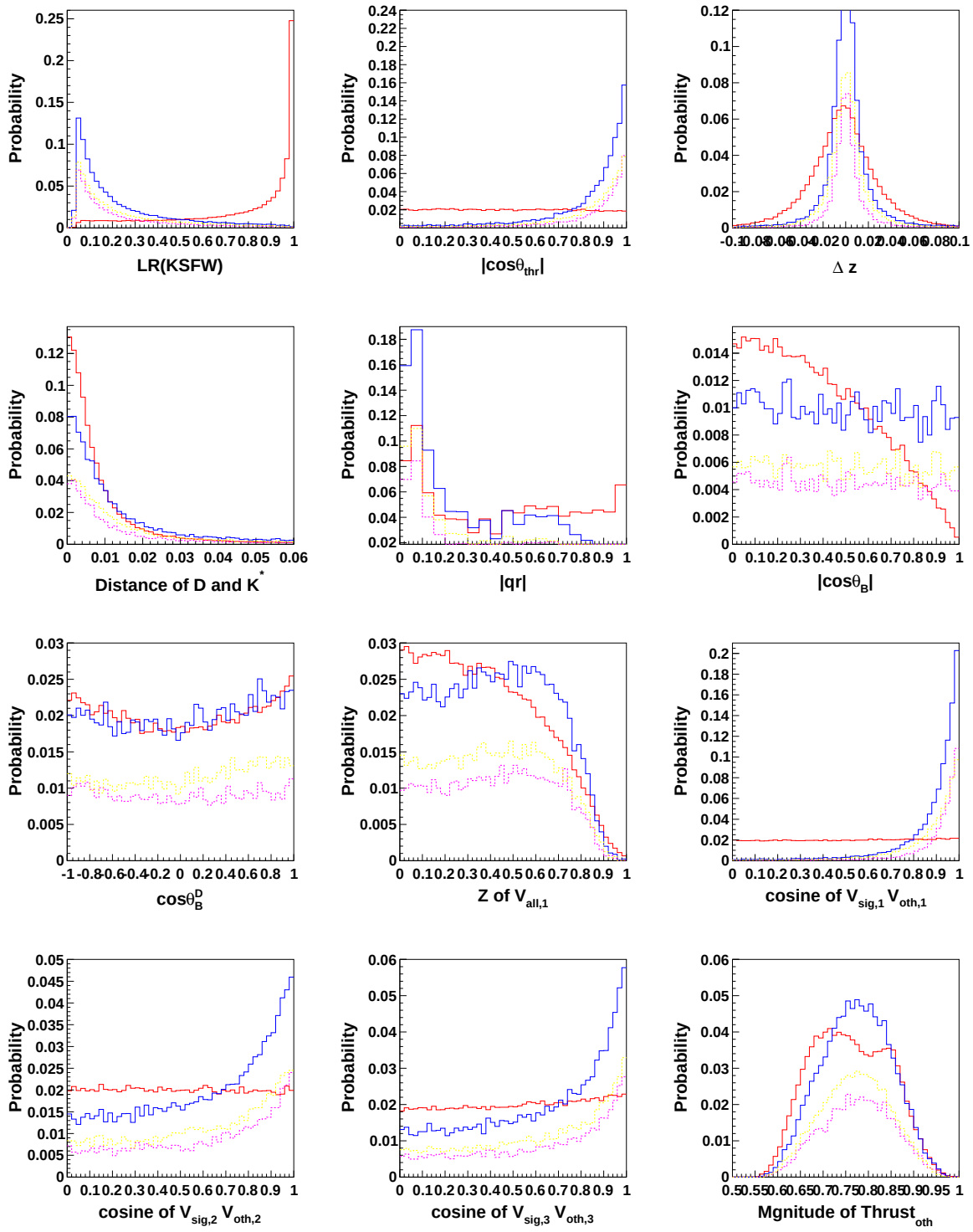

Figure 3.7: The distributions of the variables used for the discrimination. We use red curve for the signal MC and blue curve for the $q\bar{q}$ background MC, which is divided into two components shown with yellow ($q = c$) and magenta ($q = u, d, s$). All the requirements except for the one on $\mathcal{NB}$ are applied before showing the plots.

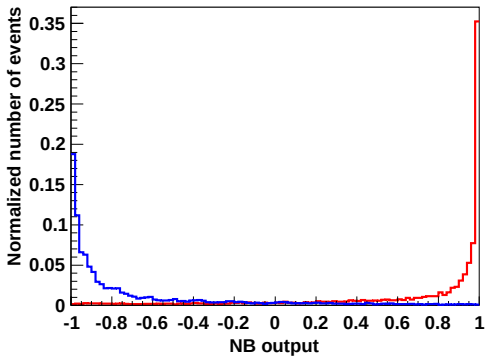

(a) The distributions of the NeuroBayes output $\mathcal{NB}$ for signal MC (red) and $q\bar{q}$ MC (blue).

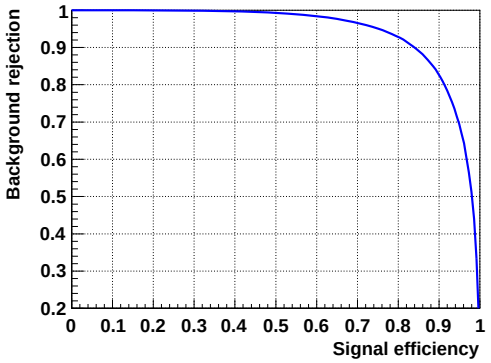

(b) The performance of the cut-based analysis is shown with BG rejection versus signal efficiency.

Figure 3.8: The output and the performance of the NeuroBayes based on 12 parameters.

Variable	Only this (σ)	Without this (σ)	Corr. to others
LR(KSFW)	290	62	0.85
Cosine of $V_{sig,1}$ $V_{oth.,1}$	280	35	0.87
Δz	145	68	0.29
Distance of D and K^{*0}	105	49	0.23
$\mid qr \mid$	126	51	0.31
$\mid \cos\theta_B \mid$	102	42	0.21
$\mid \cos\theta_{\rm thr} \mid$	246	14	0.81
Magnitude of Thrust_oth.	58	12	0.23
Z of $V_{all,1}$	42	9	0.18
Cosine of $V_{sig,3}$ $V_{oth.,3}$	84	7	0.64
Cosine of $V_{sig,2}$ $V_{oth.,2}$	80	6	0.66
$\cos\theta_B^D$	10	4	0.12

Table 3.2: The power of individual parameters.

3.3.4 $\mathcal{NB}^{\mathrm{TRANS}}$

$\mathcal{NB}$ has too peaky distribution to be used to fit parameter. $\mathcal{NB}$ is transformed to $\mathcal{NB}^{\mathrm{TRANS}}$. The definition of $\mathcal{NB}^{\mathrm{TRANS}}$ is

$$\mathcal{NB}^{\mathrm{TRANS}} = \log \frac{\mathcal{NB} - \mathcal{NB}_{\mathrm{MIN}}}{\mathcal{NB}_{\mathrm{MAX}} - \mathcal{NB}}. \tag{3.2}$$

Here we set $\mathcal{NB}_{\mathrm{MIN}} = -0.6$ and $\mathcal{NB}_{\mathrm{MAX}} = 0.9992$. The distribution of the $\mathcal{NB}^{\mathrm{TRANS}}$ is Gaussian-like as shown in Figure 3.9 which is easy to fitted (; strictly speaking, it is not Gaussian). Events whose $\mathcal{NB} < \mathcal{NB}_{\mathrm{MIN}}$ are discarded, and we confirm that there is no event which satisfy $\mathcal{NB} > \mathcal{NB}_{\mathrm{MAX}}$.

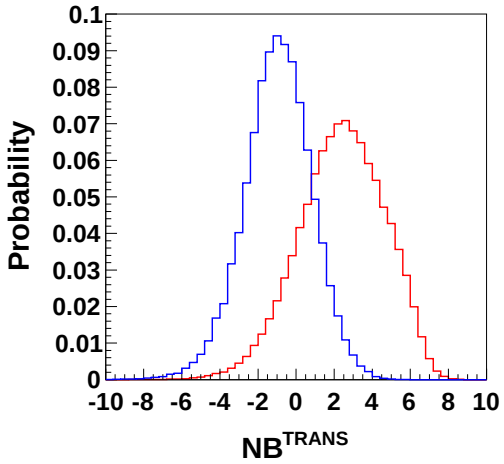

Figure 3.9: The distribution of $\mathcal{NB}^{\mathrm{TRANS}}$ for signal MC (red) and $q\bar{q}$ MC (blue).

3.4 Probability Density Function (PDF)

The number of signal events is obtained by the three-dimensional fitting to ΔE, $\mathcal{NB}^{\mathrm{TRANS}}$ and m_{bc}. There are three groups of components in the fitting. We prepare a three-dimensional function for each component to be combined for making a probability density function (PDF).

3.4.1 PDF

The strategy to make a PDF is to obtain three-dimensional function by taking a product of one-dimensional functions for ΔE, $\mathcal{NB}^{\mathrm{TRANS}}$ and m_{bc}. This method is supported by very small correlation between ΔE, $\mathcal{NB}^{\mathrm{TRANS}}$ and m_{bc} as shown in Figure 3.10. We fit in the region indicated by -0.1 GeV $< \Delta E < 0.3$ GeV, $-10 < \mathcal{NB}^{\mathrm{TRANS}} < 10$ and 5.21 GeV/c $< m_{\mathrm{bc}}$.

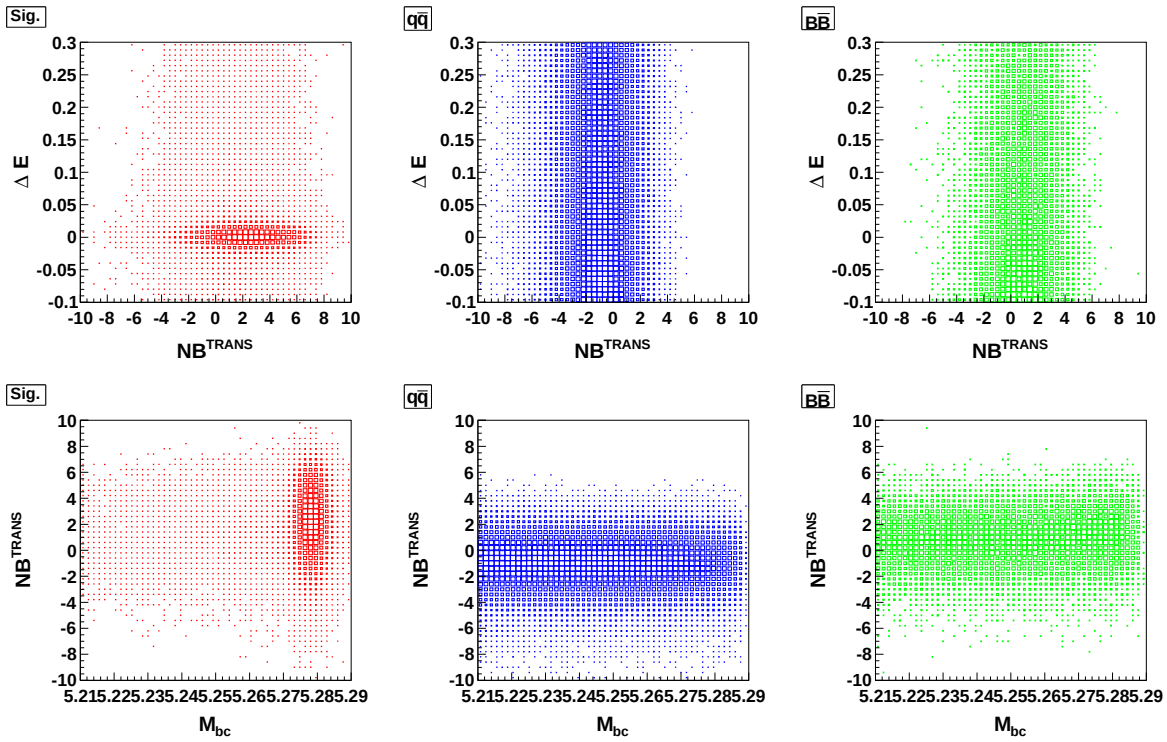

Figure 3.10: 3D distribution projected for 2D (ΔE, $\mathcal{NB}^{\rm TRANS}$) (upper) and ($\mathcal{NB}^{\rm TRANS}$, $m_{\rm bc}$) (lower) for signal (left), $q\bar{q}$ background (center) and $B\bar{B}$ background (right). The correlation factors are listed at Table 3.3.

	Correlation factor (%)	
	ΔE vs $\mathcal{NB}$	$\mathcal{NB}$ vs $m_{\rm bc}$
Signal	-4	6
$B\bar{B}$	-2	-2
$q\bar{q}$	1	10

Table 3.3: Correlation factor.

Functions for each component

We perform the 3D-fit assuming six components ; one is $B^0 \to DK^{*0}$signal, and others are backgrounds. I list these components at Table 3.4.

- Signal : This component is $B^0 \to DK^{*0}$ signal. Signal PDF shape is obtained from the 2×10^6 events generated signal MC fit. Figure 3.11 shows projection for each parameter on fit range and signal range.

- $B\bar{B}$ real D : $B\bar{B}$ background is split into $B\bar{B}$ real D and $B\bar{B}$ fake D. $B\bar{B}$ real D is $B\bar{B}$ background which is reconstructed $[K_S\pi^+\pi^-]_D$ is true D. PDF shape is obtained from MC sample six times larger than real data. One MC dataset as large as real data (corresponding to 772×10^6 $B\bar{B}$) is counted "stream" unit, each steam is independent. Figure 3.12 shows projection for each parameter on fit range and signal range. In this fit, $D^0\rho^0$ like one miss-PID backgrounds yield is floated.

- $B\bar{B}$ fake D : $B\bar{B}$ fake D is $B\bar{B}$ background other than $B\bar{B}$ real D. PDF shape is obtained from six streams MC fit. Figure 3.13 shows projection for each parameter on fit range and signal range.

- $q\bar{q}$: $e^+e^- \to q\bar{q}$, q is (u, d, s and c), events. PDF shape is obtained from six streams MC fit. Figure 3.14 shows projection for each parameter on fit range and signal range.

- $D^0\rho^0$: We defined $D^0\rho^0$ like one miss-PID events are called it. So, this component describes not only $D^0\rho^0$. PDF shape is obtained from 1×10^6 events (corresponding to $\sim$ 300 times larger than expected one) generated $D^0\rho^0$ MC. Figure 3.15 shows projection for each parameter on fit range and signal range.

- $D^0a_1^+$: We defined $D^0a_1^+$ like one miss-PID and 1 π^0 missing events are called it. So, this component describes not only $D^0a_1^+$. PDF shape is obtained from 5×10^6 (corresponding to $\sim$ 60 times larger than expected one) events generated $D^0a_1^+$ MC. Figure 3.16 shows projection for each parameter on fit range and signal range.

	ΔE	$\mathcal{NB}^{\mathrm{TRANS}}$	m_{bc}
Signal	Double Gaussian	Gaussian + BifurcatedGaussian	Gaussian + Argus
$B\bar{B}$ real D	Exponential	Gaussian + BifurcatedGaussian	Crystal Ball
$B\bar{B}$ fake D	Exponential	Gaussian + BifurcatedGaussian	Argus
$q\bar{q}$	1^{st} order Chebychev	BifurcatedGaussian	Argus
$D^0\rho^0$	Double Gaussian	Gaussian + BifurcatedGaussian	Gaussian + Argus
$D^0a_1^+$	Double Gaussian	Gaussian	Gaussian

Table 3.4: PDF.

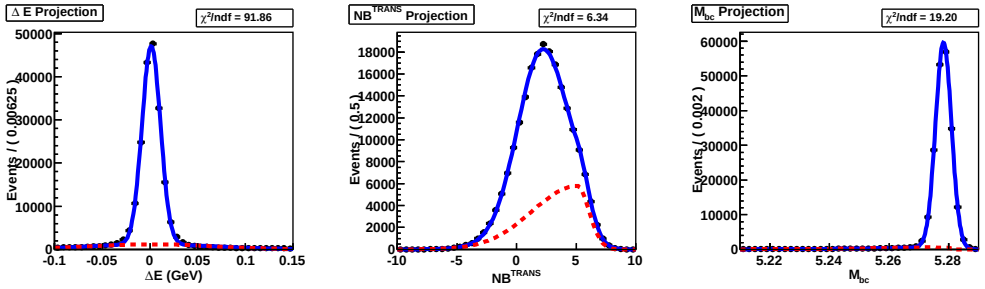

(a) The 3D-distribution projected for each parameter (ΔE lest, $\mathcal{NB}^{\mathrm{TRANS}}$ middle, m_{bc} right) on the signal MC sample.

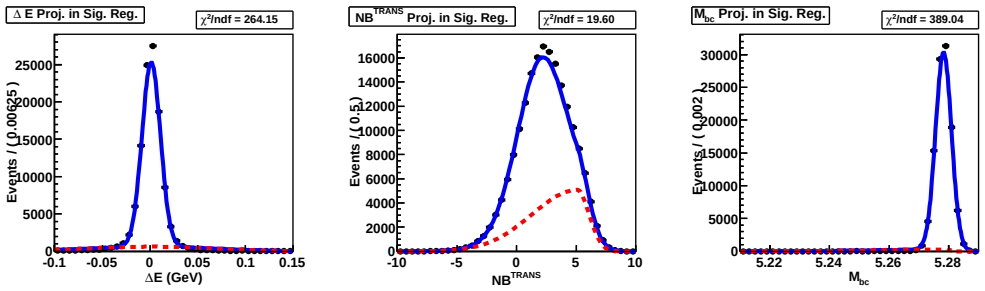

(b) The 3D-distributions in signal region on the signal MC sample. Signal region is defined $|\Delta E| < 0.03$, $\mathcal{NB}^{\mathrm{TRANS}} > 2$ and $|m_{B^0} - m_{\mathrm{bc}}| < 0.008$.

Figure 3.11: Signal PDF, projected for each parameter on fit region and signal region.

3.5 Signal Extraction Projected for All Dalitz Region

Using the method of configuring PDF described in the previous section, we fit the MC and data samples. We use all the $\Upsilon(4S)$ samples that contain 772 million $B\bar{B}$ pairs in reprocessed data.

I obtain the result of signal yield $\sum_i (N_i + \bar{N}_i) = 44.2^{+13.3}_{-12.1}$ with unbinned all Dalitz region. Fig. 3.17 shows that projections for each of 3D parameter, and Table. 3.5 show summarized each component yield.

I can obtain the branching fraction of $B^0 \to \bar{D}^0 K^{*0}$ as $\Gamma(B^0 \to \bar{D}^0 K^{*0}) = (2.9 \pm 0.9) \times 10^{-5}$ with assumption there is no contribution $B^0 \to D^0 K^{*0}$ interference. This error includes only statistical uncertainty. In PDG value, $\Gamma(B^0 \to \bar{D}^0 K^{*0}) = (4.2 \pm 0.6) \times 10^{-5}$. A difference between obtained branching fraction and world average's one is 1.2 σ. Possible causes for this difference are assumption of no $B^0 \to D^0 K^{*0}$ (suppressed decay) contribution, existence of $B^0 \to DK\pi$ non resonant or K^* higher resonant, and so on. For the first, in neutral B decay, suppressed decay $B^0 \to D^0 K^{*0}$ contribution is larger than charged B one. The amplitude ratio ($= r_S$) is expected to be [0.2, 0.4]. For the second, to check existence of $B^0 \to DK\pi$ non resonant or K^* higher resonant, (k factor is affected or not) we have to study on $B^0 \to DK^+\pi^-$ three body decay Dalitz. Here, I assume this difference comes from only suppressed decay. The statistical significances are

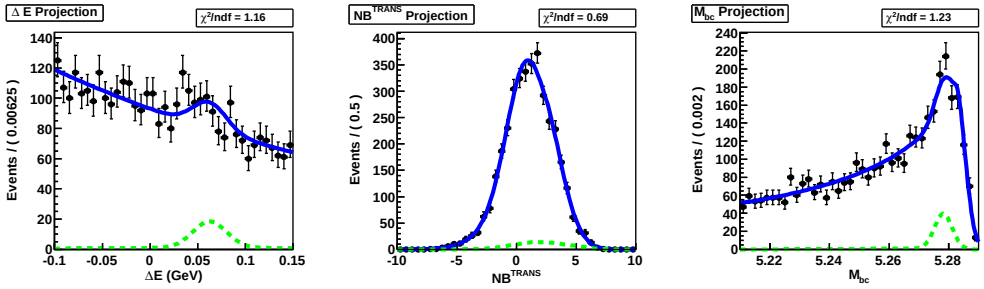

(a) The 3D-distribution projected for each parameter (ΔE lest, $\mathcal{NB}^{\mathrm{TRANS}}$ middle, m_{bc} right) on the $B\bar{B}$ real D MC sample.

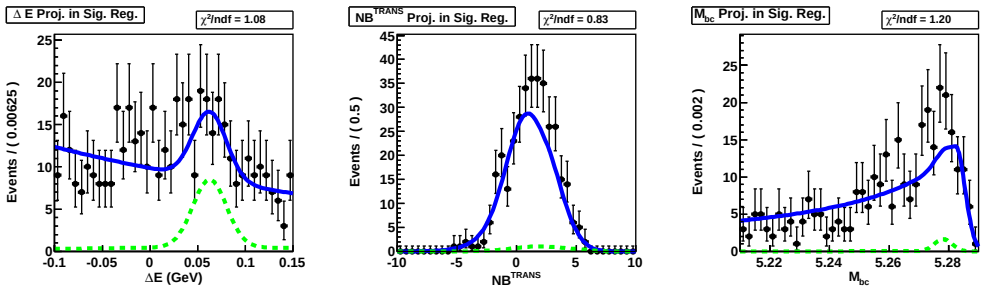

(b) The 3D-distributions in signal region on the $B\bar{B}$ real D MC sample. Peaking at $\Delta E \sim 0.05$ GeV is $D\rho$ events, its shape is fixed by fit for $D\rho$. Signal region is defined $|\Delta E| < 0.03$, $\mathcal{NB}^{\mathrm{TRANS}} > 2$ and $|m_{B^0} - m_{\mathrm{bc}}| < 0.008$.

Figure 3.12: $B\bar{B}$ real D PDF, projected for each parameter on fit region and signal region.

estimated as $\sqrt{-2\ln(\mathcal{L}_0/\mathcal{L}_{\mathrm{max}})} = 2.80\ \sigma$, here $\mathcal{L}_{\mathrm{max}}$ is the maximum likelihood and $\mathcal{L}_0$ is the likelihood when the signal yield is constrained to be zero.

Signal	$44.2^{+13.3}_{-12.1}$
$B\bar{B}$ real D	$695.8^{+177.6}_{-175.6}$
$D^0\rho^0$	$16.6^{+16.7}_{-13.6}$
$D^0a_1^+$	$59.3^{+22.3}_{-20.8}$
$B\bar{B}$ fake D	$1963.2^{+228.1}_{-227.5}$
$q\bar{q}$	$11075.7^{+156.6}_{-155.5}$

Table 3.5: The list of values of component yield for the fit on data.

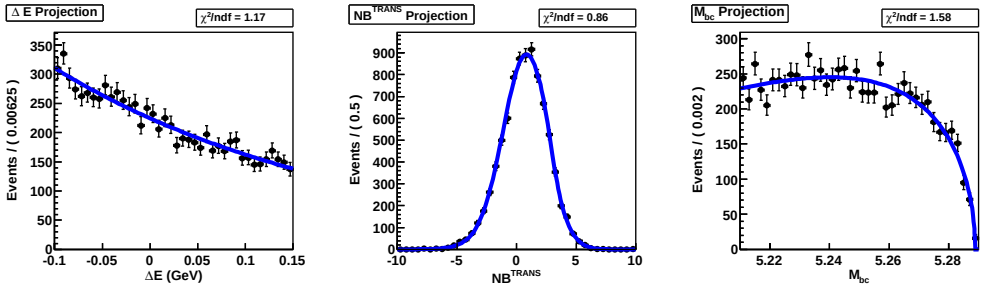

(a) The 3D-distribution projected for each parameter (ΔE lest, $\mathcal{NB}^{\mathrm{TRANS}}$ middle, m_{bc} right) on the $B\bar{B}$ fake D MC sample.

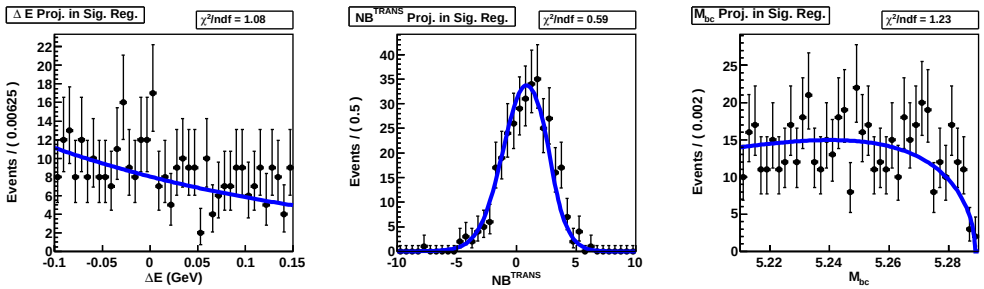

(b) The 3D-distributions in signal region on the $B\bar{B}$ fake D MC sample. Signal region is defined $|\Delta E| < 0.03$, $\mathcal{NB}^{\mathrm{TRANS}} > 2$ and $|m_{B^0} - m_{\mathrm{bc}}| < 0.008$.

Figure 3.13: $B\bar{B}$ fake D PDF, projected for each parameter on fit region and signal region.

3.6 (x, y) Fit on $D\pi$ Mode

3.6.1 Fit Procedure to Obtain $(x_{\pm}, y_{\pm})$

In this analysis, we obtain $x_{\pm}$ and $y_{\pm}$, which in tern are used to obtain ϕ_3 as well as r_S and δ_S. The procedure to obtain the $x_{\pm}$, $y_{\pm}$ is as follows:

- Parametrize the distributions of signal and background events in the variables that will be used to extract the number of events – in our case, m_{bc}, ΔE, and $q\bar{q}$ suppression parameter $\mathcal{NB}^{\mathrm{TRANS}}$.
- Fit the data distribution in each bin of Dalitz plane separately, with the number of events for signal and backgrounds as free parameters.
- Once the numbers of events in "i-th" bin N_i have been found, put them into Eq. 1.85 to obtain the parameters $x_{\pm}$, $y_{\pm}$. Technically it can be done by minimizing the negative logarithmic likelihood of the form

$$-2\log\mathcal{L}(x,y) = -2\sum_i \log p(\langle N_i\rangle(x,y), N_i, \sigma_{N_i}), \tag{3.3}$$

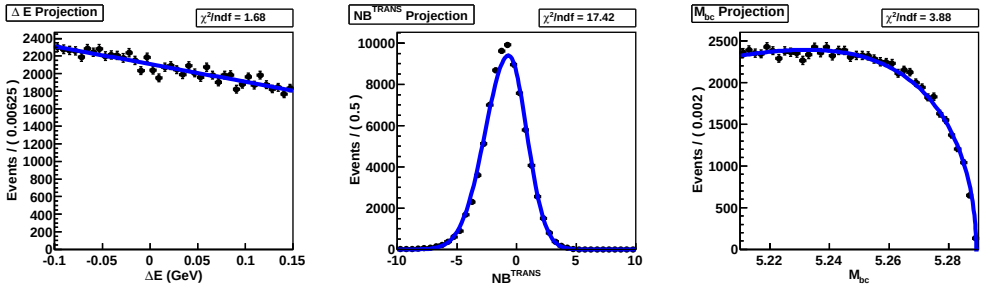

(a) The 3D-distribution projected for each parameter (ΔE lest, $\mathcal{NB}^{\mathrm{TRANS}}$ middle, m_{bc} right) on the $q\bar{q}$ MC sample.

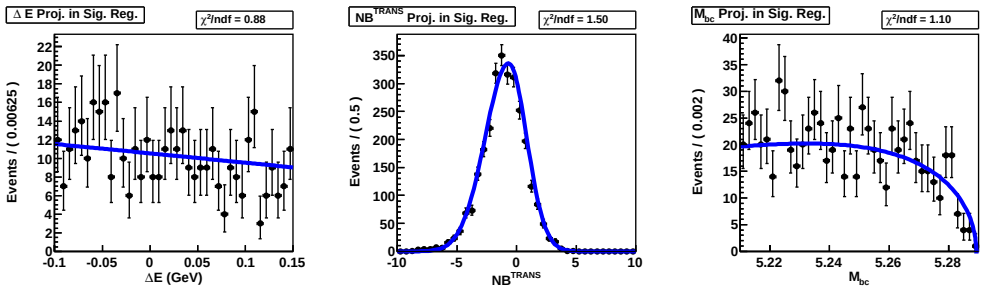

(b) The 3D-distributions in signal region on the $q\bar{q}$ MC sample. Signal region is defined $|\Delta E| < 0.03$, $\mathcal{NB}^{\mathrm{TRANS}} > 2$ and $|m_{B^0} - m_{\mathrm{bc}}| < 0.008$.

Figure 3.14: $q\bar{q}$ PDF, projected for each parameter on fit region and signal region.

here $\langle N_i \rangle(x, y)$ is the expected number of events in the bin i obtained from Eq. 1.85, N_i and σ_{N_i} are the observed number of events and its error obtained from the data fit. If the distribution p is Gaussian, this likelihood translates to the χ^2 fit. Here, I assume this likelihood method as normally χ^2 method.

Note that the procedure described above does not make any assumptions on the Dalitz distribution of the background events, since the fits in each bin are independent. Thus there is no associated systematic uncertainty. However, in the case of small number of events and many background components this can be a limiting factor. The solution would be to use the Combined Fit with a common likelihood in all bins. Relative numbers of background events in bins in such a fit can be constrained externally from e.g. MC sample. In addition, in the case of the Combined Fit, the two-step procedure of first extracting the numbers of signal events, and then using them to obtain (x, y) is not needed anymore – we can plug the expected numbers of events $\langle N_i \rangle$ as functions of (x, y) directly into the likelihood. Thus the variables (x, y) become free parameters of the combined likelihood fit, and the assumption of the Gaussian distribution of the number of signal events is not needed. Both approaches (Separate Fit in bins, and the Combined Fit) are tested in the MC sample fits, and the results are compared. Generally speaking, Combined Fit has advantage on small statistic and large background contribution.

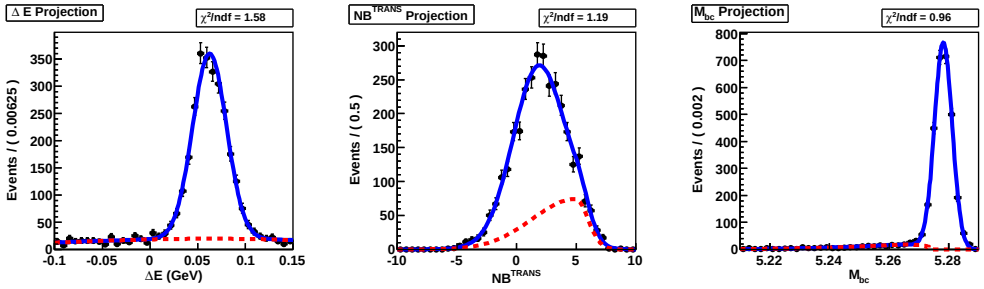

(a) The 3D-distribution projected for each parameter (ΔE lest, $\mathcal{NB}^{\mathrm{TRANS}}$ middle, m_{bc} right) on the $D^0\rho^0$ MC sample.

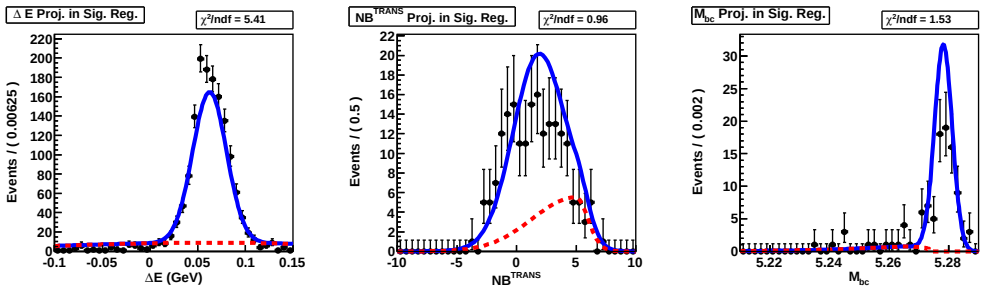

(b) The 3D-distributions in signal region on the $D^0\rho^0$ MC sample. Signal region is defined $|\Delta E| < 0.03$, $\mathcal{NB}^{\mathrm{TRANS}} > 2$ and $|m_{B^0} - m_{\mathrm{bc}}| < 0.008$.

Figure 3.15: $D^0\rho^0$ PDF, projected for each parameter on fit region and signal region.

3.6.2 Correction on N_i

In this section, we review the procedure of the analysis taking into account various experimental effects: efficiency variations across the decay phase space, background, finite momentum resolution, radiative corrections, and flavor flip. Corrections on N_i taken into account are

1). Difference in efficiency between bins

2). Cross-feed between each bin

3). Flavor flip due to $K^{*0} \to K^+\pi^-$ double miss PID.

Details of those are below. However, the effect of flavor flip can not affect on $D\pi$ control sample study. Also in DK^{*0}, it is neglected, because flavor flip event rate is very small. Effects of efficiency and cross-feed are estimated with DK^{*0} signal mode MC sample.

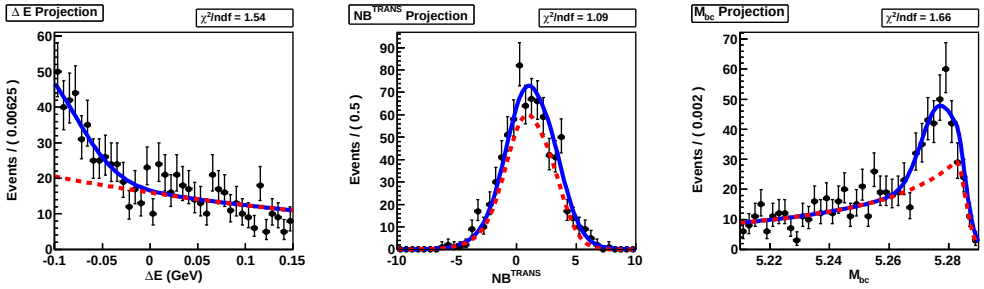

(a) The 3D-distribution projected for each parameter (ΔE lest, $\mathcal{NB}^{\mathrm{TRANS}}$ middle, m_{bc} right) on the $D^0a_1^+$ MC sample.

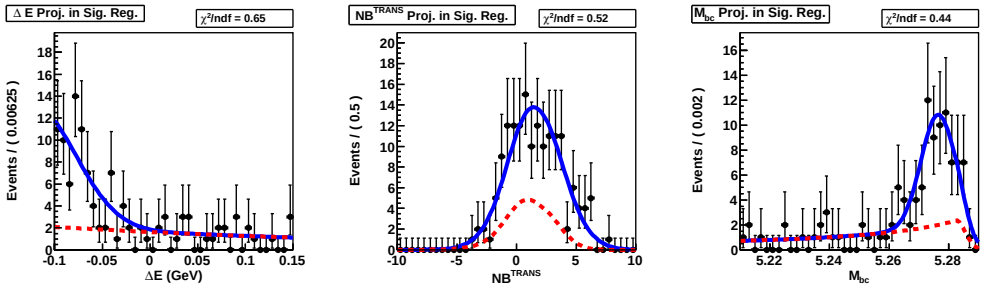

(b) The 3D-distributions in signal region on the $D^0a_1^+$ MC sample. Signal region is defined $|\Delta E| < 0.03$, $\mathcal{NB}^{\mathrm{TRANS}} > 2$ and $|m_{B^0} - m_{\mathrm{bc}}| < 0.008$.

Figure 3.16: $D^0a_1^+$ PDF, projected for each parameter on fit region and signal region.

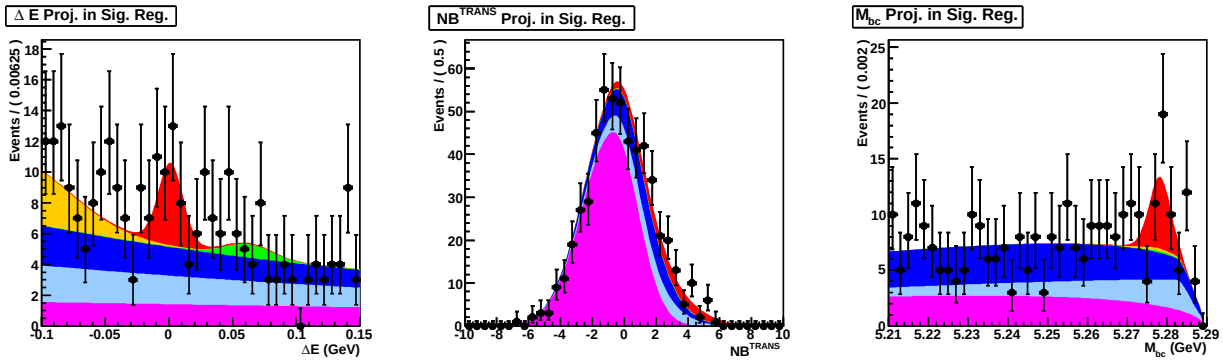

Figure 3.17: 3D-fit all dalitz region for real data, projected for each parameter (ΔE left, $\mathcal{NB}^{\mathrm{TRANS}}$ middle, m_{bc} right) in signal region. Red is signal. Dark blue is $B\bar{B}$ real D. Light blue is $B\bar{B}$ fake D. Magenta is $q\bar{q}$. Yellow is $D^0\rho^0$. Green is $D^0a_1^+$.

Difference in efficiency between bins

With the detection efficiency taken into account (that is in general non-uniform across the bin region), the number of events detected is:

$$N' = \int p(\mathcal{D})\epsilon(\mathcal{D})d\mathcal{D} \tag{3.4}$$

Here $\mathcal{D}$ is position of Dalitz plane, $p(\mathcal{D})$ is density of signal number at $\mathcal{D}$, $\epsilon(\mathcal{D})$ is the signal efficiency at $\mathcal{D}$. Clearly, the efficiency does not factorize. One can use an efficiency averaged over the bin, and to correct for it in the analysis:

$$\bar{\epsilon}_i = N_i'/N_i = \int p(\mathcal{D})\epsilon(\mathcal{D})d\mathcal{D} / \int p(\mathcal{D})d\mathcal{D} \tag{3.5}$$

The averaged efficiency $\bar{\epsilon}_i$ can be determined from MC, but it depends on $p(\mathcal{D})$, *i. e.* it is weakly model-dependent. Figure 3.18 show $\bar{\epsilon}_i$ the efficiency averaged on each bin.

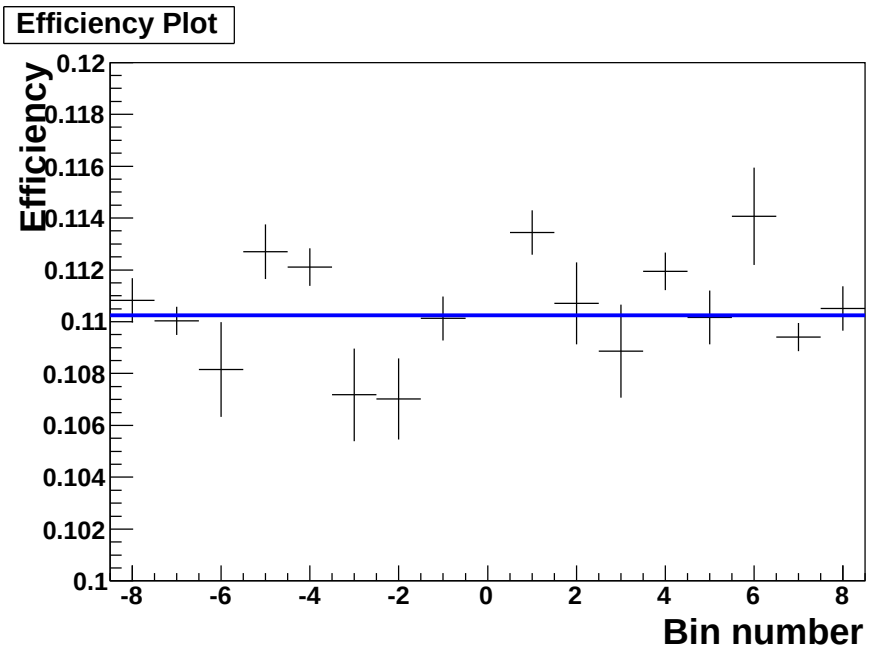

Figure 3.18: Efficiency for each bin $\bar{\epsilon}_i$. Blue line means average of all Dalitz region. Vertical error bars mean statistical uncertainty of CM sample.

Cross-feed between each bin

Finite momentum resolution leads to the migration on the events between the bins. In the binned approach, this effect can be easily described and corrected for. The migration can be described by the linear transformation of the number of events in bins:

$$N_i' = \sum \alpha_{ik} N_k \tag{3.6}$$

here N_k is the number of events the bin k would contain without the crossfeed, and N_i' is the reconstructed number of events in the bin i. The crossfeed matrix α_{ik} is nearly unit: $\alpha_{ik} \ll 1$ for $i \neq k$. This matrix can be obtained from the signal MC simulation. The matrix α_{ik} depends on the density over the Dalitz plot. Therefore, the reasonably realistic model has to be used in the simulation.

Generated bin \ Measured bin	-8	-7	-6	-5	-4	-3	-2	-1	1	2	3	4	5	6	7	8
8	0	0	0	0	0	0	0	0	2	1	0	1	0	0	2	93
7	0	1	0	0	0	0	0	0	2	2	0	0	1	0	94	0
6	0	0	0	0	0	0	0	0	0	4	0	0	2	93	0	0
5	0	0	0	0	0	0	0	0	0	0	0	1	96	2	1	0
4	0	0	0	0	0	0	0	0	1	0	0	97	1	0	0	0
3	0	0	0	0	0	0	0	0	3	4	92	0	0	0	0	0
2	0	0	0	0	0	0	0	0	1	90	4	0	0	2	1	0
1	0	0	0	0	0	0	0	0	92	1	3	2	0	0	1	0
-1	0	1	0	0	2	3	1	92	0	0	0	0	0	0	0	0
-2	0	1	3	0	0	4	90	1	0	0	0	0	0	0	0	0
-3	0	0	0	0	0	92	4	3	0	0	0	0	0	0	0	0
-4	0	0	0	1	97	0	0	1	0	0	0	0	0	0	0	0
-5	0	1	2	96	1	0	0	1	0	0	0	0	0	0	0	0
-6	0	0	93	2	0	0	4	0	0	0	0	0	0	0	0	0
-7	0	94	0	1	0	0	2	2	0	0	0	0	0	0	1	0
-8	92	2	1	0	1	0	1	3	0	0	0	0	0	0	0	0

Table 3.6: Cross-feed matrix α_{ik} (values in per cent).

Note also that in the case of $D \to K^0_S\pi^+\pi^-$ decay from B, the crossfeed depends on the parameters (x, y). We assume that this effect is small. I listed cross-feed matrix in Table. 3.6.

Flavor flip due to $K^{*0} \to K^+\pi^-$ double miss PID

In K^{*0} reconstruction from $K^+\pi^-$, if we take a double miss particle identification, reconstructed B flavor is taken flip from true B flavor. We obtain the ratio of double miss PID β, and the number of events is writen in:

$$N'_i = N_i + \beta\bar{N}_i. \tag{3.7}$$

β can be obtained by signal MC, to be $\beta \sim (0.119 \pm 0.007)\%$. This value is too small to be able to neglected.

3.6.3 (x, y) Fit on $D\pi$ Real Data

To check validity of my (x, y) fitter, we analyze $B^\pm \to D\pi^\pm$ and check the consistency with Belle charged B 605 fb^{-1} model-independent result [18]. Decay $B^\pm \to D\pi^\pm$ has almost similar dynamics as the corresponding signal modes $B^0 \to DK^{*0}$, but with an order of magnitude larger branching ratio. Small amplitude ratio of $B^- \to D^0\pi^-$ and $B^- \to \bar{D}^0\pi^-$, $r \sim 0.01$ (which can be ϕ_3 limited factor) is expected in those decays due to small ratio of the weak coefficients $|V_{ub}V^*_{cd}|/|V_{cb}V^*_{ud}| \sim 0.02$ and additional color

suppression factor as in the case of $B^{\pm} \to DK^{\pm}$. These decays are used as control samples to test the procedures of the background extraction and Dalitz plot fit.

As to event selection, the same criteria on D selection as $B^0 \to DK^{*0}$ is required. Primary pion is required $LR(K/\pi) < 0.6$. B selection (best candidate selection) is the same as $B^0 \to DK^{*0}$. For rejection of backgrounds, $\Delta M < 0.15$ GeV/c^2 veto and $q\bar{q}$ events reduction: $\mathcal{NB}^{\rm TRANS} > -0.6$ are required. We obtain $\mathcal{NB}^{\rm TRANS}$ from the same parameters as $B^0 \to DK^{*0}$ ones with optimization for separation of $B^{\pm} \to D\pi^{\pm}$ signal and $q\bar{q}$ events.

Extraction of the number of signal events is performed by the same way as $B^0 \to DK^{*0}$, fitting the 3D distribution of variables ΔE, $m_{\rm bc}$ and $q\bar{q}$ suppression parameter $\mathcal{NB}^{\rm TRANS}$. The fit to $B^{\pm} \to D\pi^{\pm}$ sample uses four background components in addition to the signal PDF. These are:

- $q\bar{q}$ backgrounds, it is from $e^+e^- \to q\bar{q}$ process, here $q = (u,\ d,\ s,\ c)$.
- $D^{*0}\pi^{\pm}$ background, it has peak on ΔE lower than signal. The its PDF shape is fixed from MC.
- $D^{*\pm}\pi^{\mp}$ background, it has peak on ΔE lower than signal. The its PDF shape is fixed from MC.
- Other $B\bar{B}$ backgrounds. The its PDF shape is fixed from MC.

The PDF for the signal parametrization (as well as for each of the background components) is a product of (ΔE, $m_{\rm bc}$, $\mathcal{NB}^{\rm TRANS}$) PDFs. The signal PDF is obtained from the same way as $B^0 \to DK^{*0}$. However, ΔE and $m_{\rm bc}$ peak position and width are floated at the data fit. 3D-fit without Dalitz binning are shown in Fig. 3.19

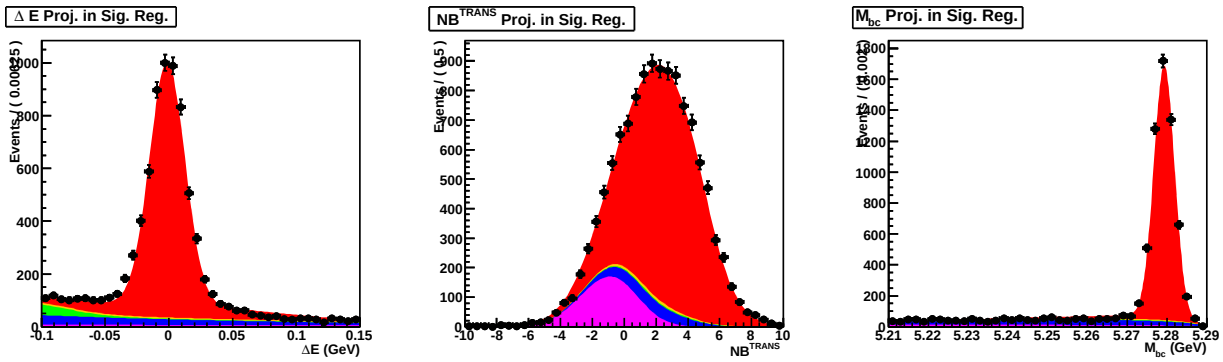

Figure 3.19: $D\pi$ 3D-fit all dalitz region for real data, projected for each parameter (ΔE left, $\mathcal{NB}^{\rm TRANS}$ middle, $m_{\rm bc}$ right) in signal region.

To obtain (x, y), we perform binned 3D-fit on real data. We show the legend of bin region on Dalitz plane at Fig 3.20. Combined fit is used. Fit result on each production of 3D in signal region ($|\Delta E| < 0.03$, $m_{\rm bc} > 5.27$, $\mathcal{NB}^{\rm TRANS} > 0$) for each bin are shown in Fig. 3.21-3.26. (x, y) result are summarized at Table 3.7, here error of my result

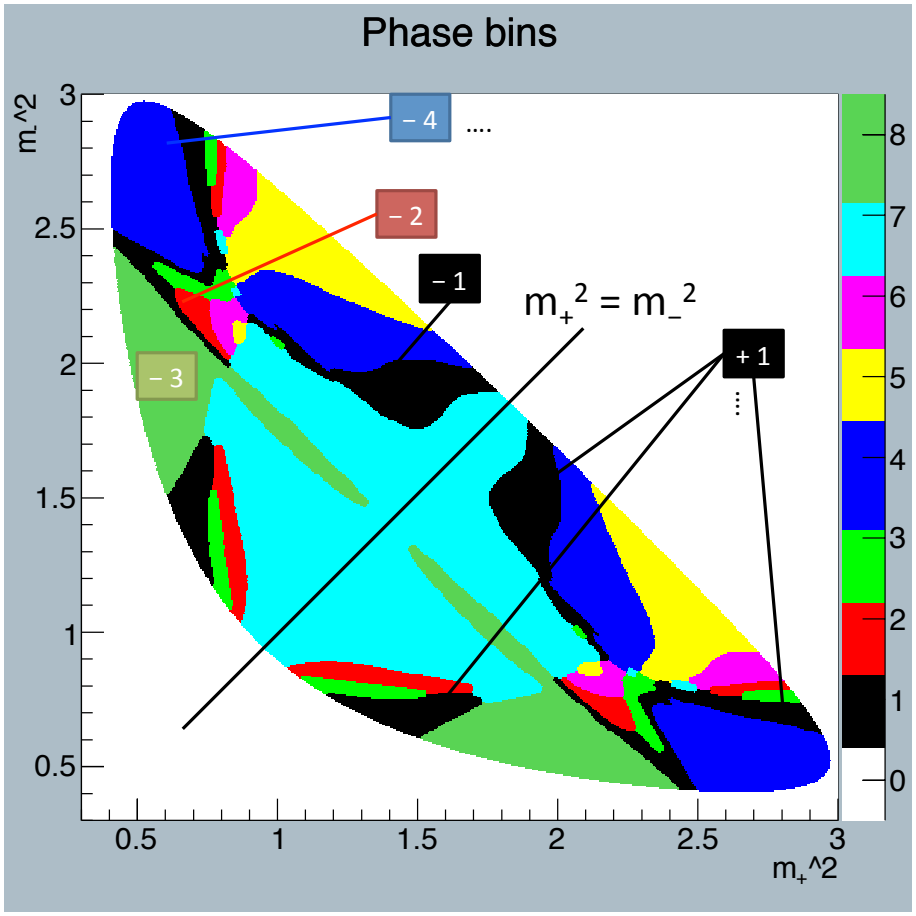

Figure 3.20: Legend of Dalitz binning. We use almost the same manner on $D\pi$ and DK^{*0} modes except for $B^0 \leftrightarrow B^+$ and $\bar{B}^0 \leftrightarrow B^-$.

are obtained from the likelihood distribution with assumption of no correlation x and y, however previous result first errors are corresponding to the statistical uncertainty from Feldman-Cousin method, and second errors are systematic uncertainty.

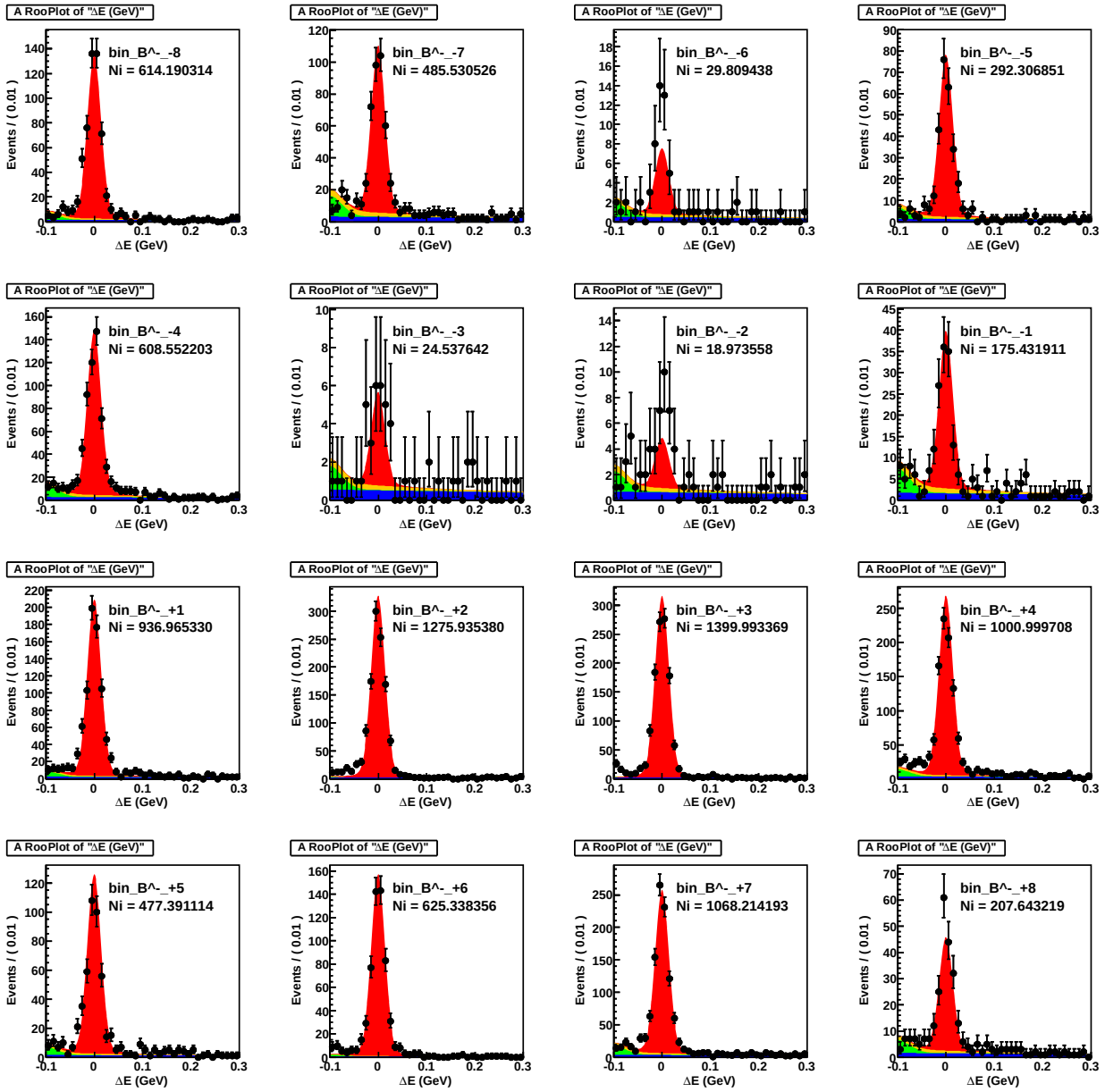

Figure 3.21: $D\pi$ 3D-fit each Dalitz bin region, projection for ΔE in signal region on B^-. Red is signal. Magenta is $q\bar{q}$. Yellow is $D^{*0}\pi^{\pm}$. Green is $D^{*\pm}\pi^{\mp}$. Blue is $B\bar{B}$.

$(x_{\pm}, y_{\pm})$ we obtained and previous one are shown in Table 3.7, and we added my $D\pi$ result on Belle previous result (x, y) 2D plot at Fig. 3.28. The value for (x_+, y_+) are good agreement for previous result, however those for (x_-, y_-) are 2-3 σ apart. The possible

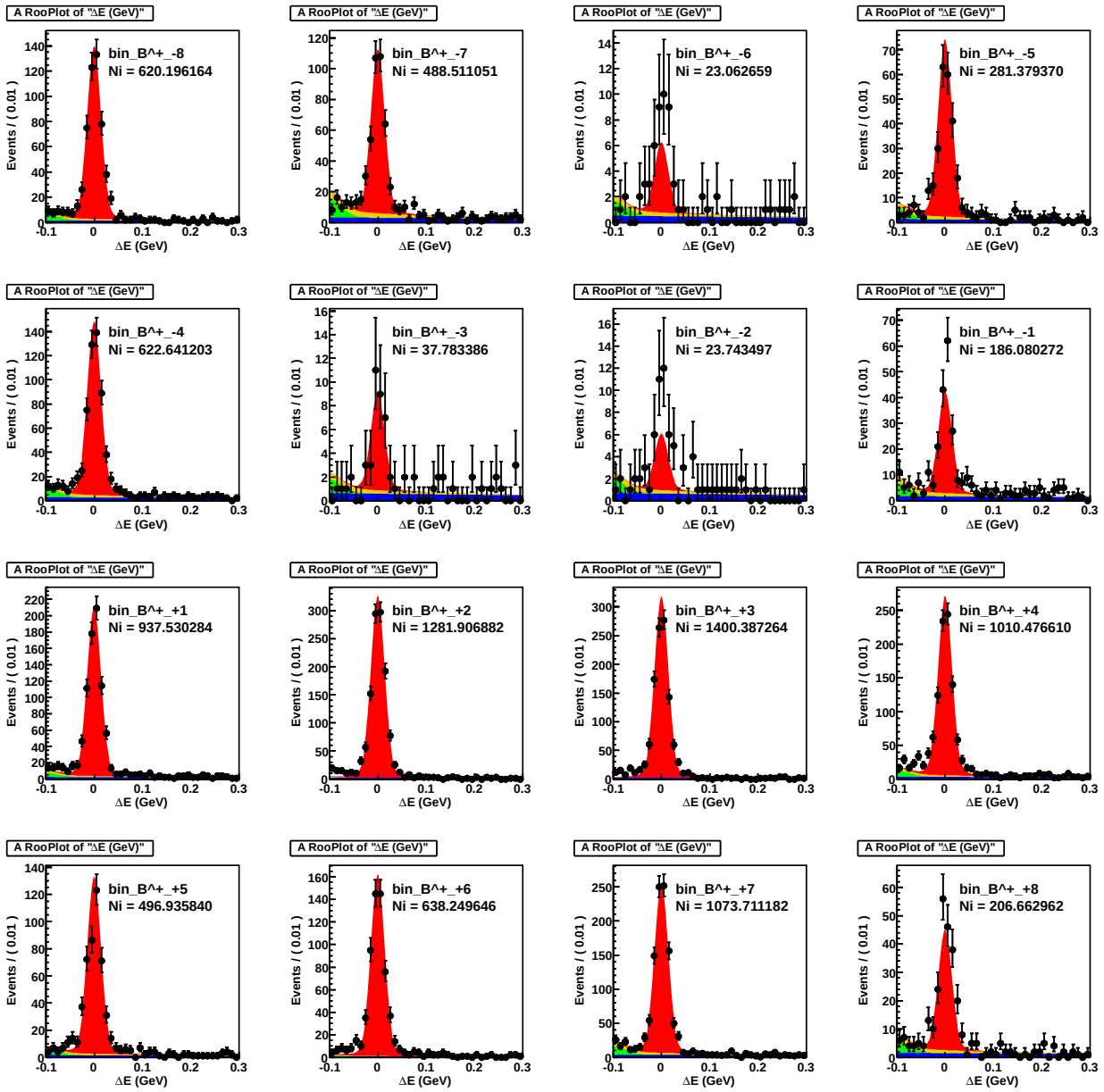

Figure 3.22: $D\pi$ 3D-fit each Dalitz bin region, projection for ΔE in signal region on B^+. Red is signal. Magenta is $q\bar{q}$. Yellow is $D^{*0}\pi^{\pm}$. Green is $D^{*\pm}\pi^{\mp}$. Blue is $B\bar{B}$.

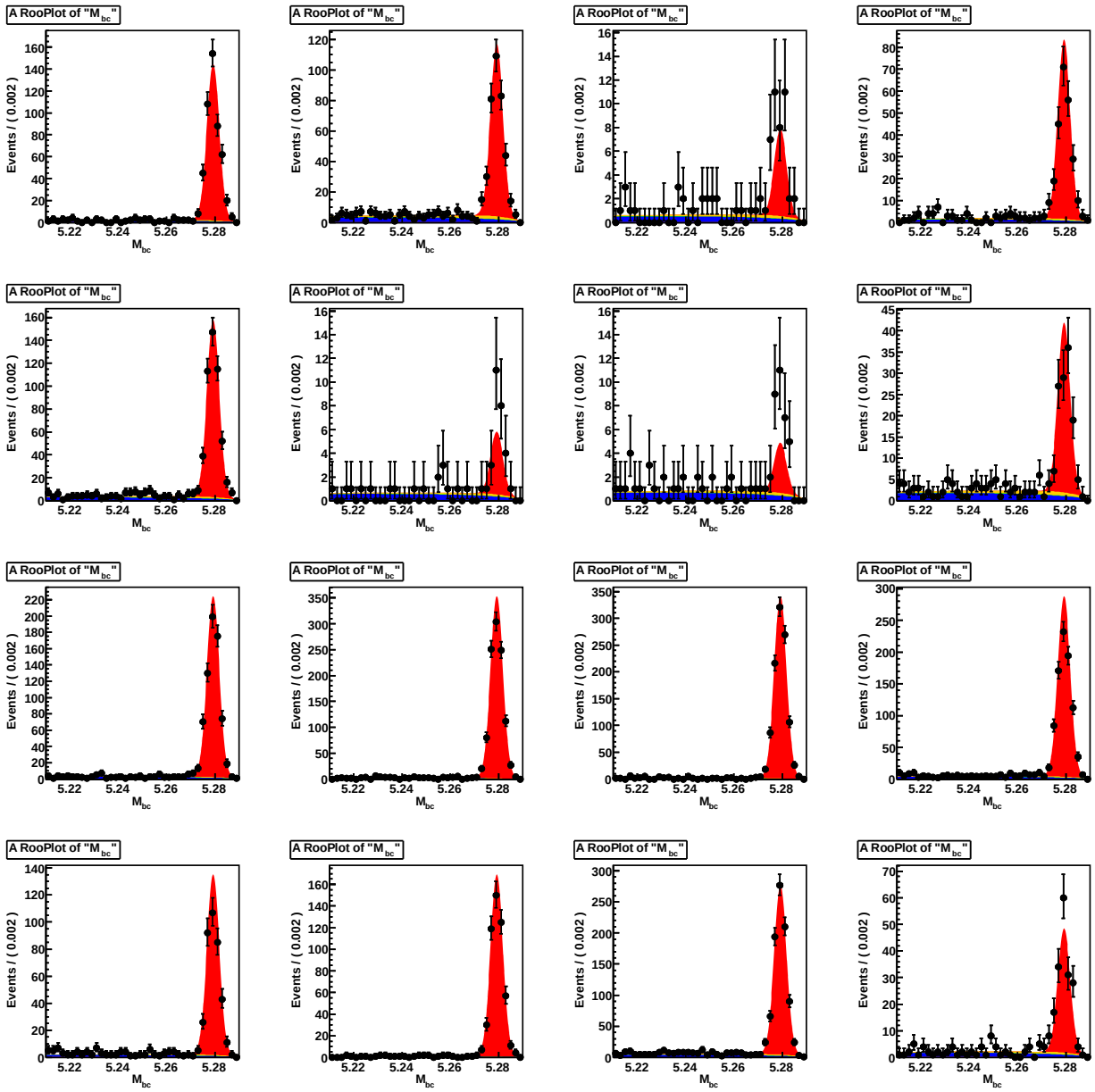

Figure 3.23: $D\pi$ 3D-fit each Dalitz bin region, projection for $m_{\rm bc}$ in signal region on B^-. Red is signal. Magenta is $q\bar{q}$. Yellow is $D^{*0}\pi^{\pm}$. Green is $D^{*\pm}\pi^{\mp}$. Blue is $B\bar{B}$.

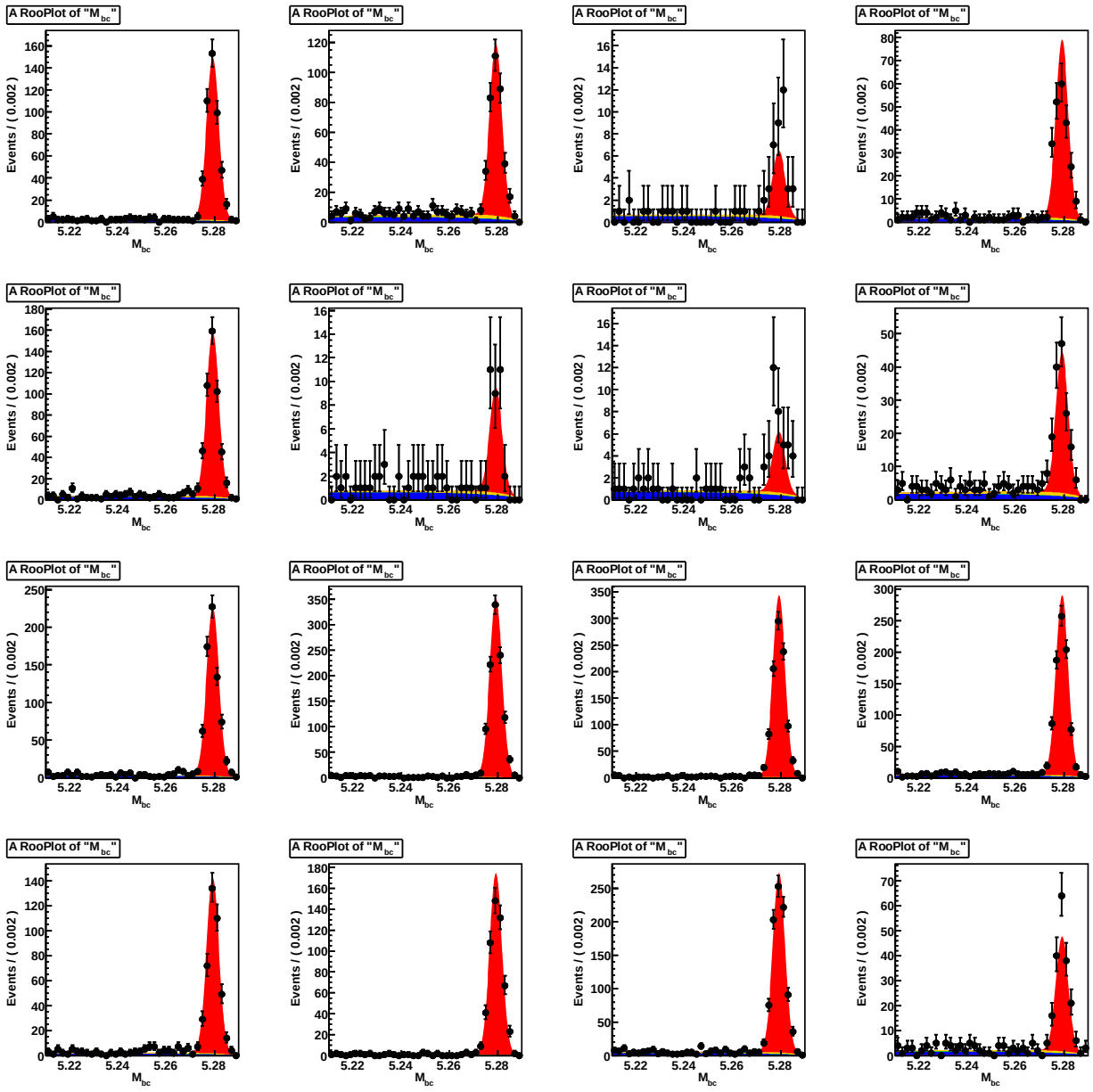

Figure 3.24: $D\pi$ 3D-fit each Dalitz bin region, projection for $m_{\rm bc}$ in signal region on B^+. Red is signal. Magenta is $q\bar{q}$. Yellow is $D^{*0}\pi^{\pm}$. Green is $D^{*\pm}\pi^{\mp}$. Blue is $B\bar{B}$.

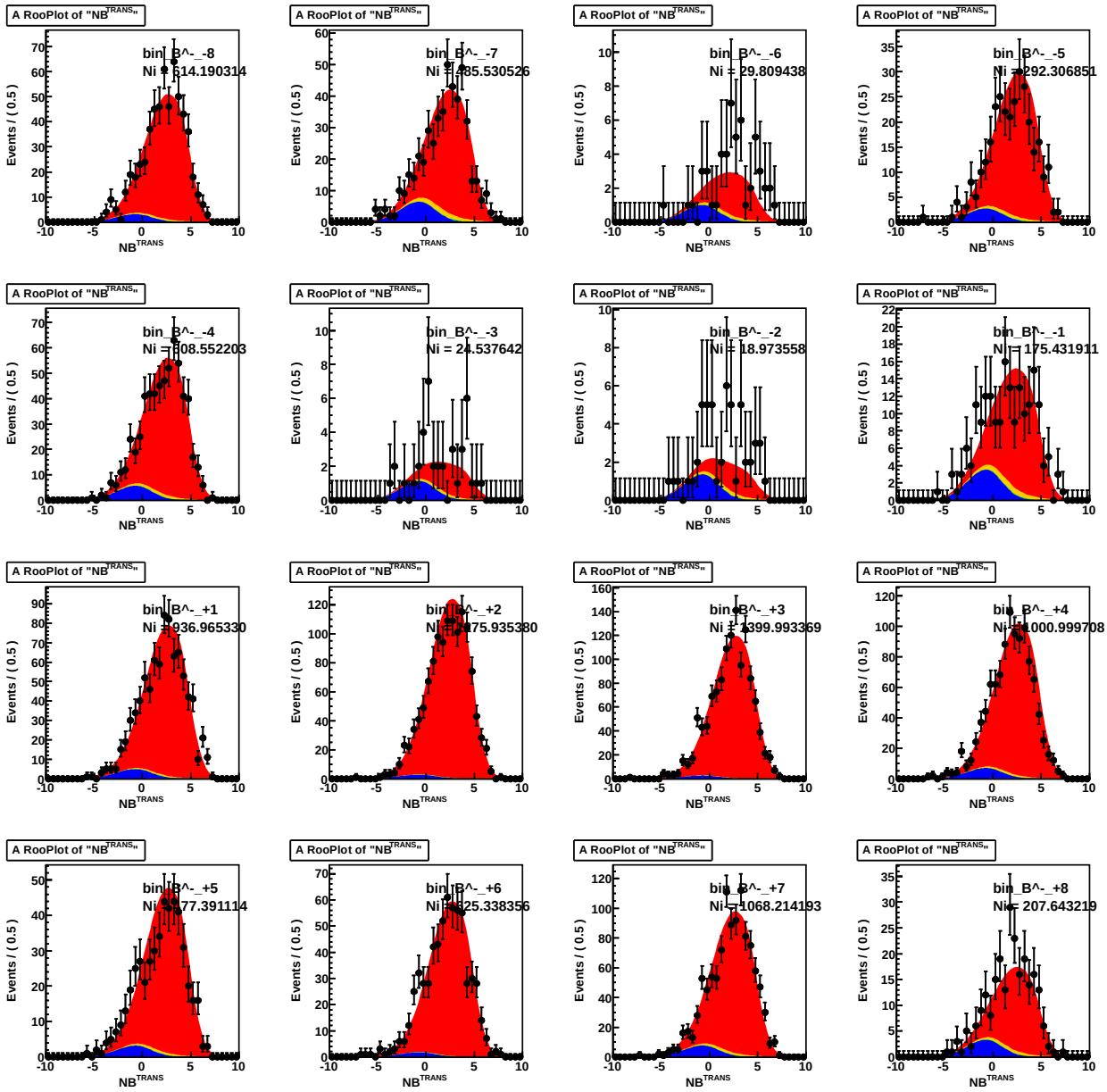

Figure 3.25: $D\pi$ 3D-fit each Dalitz bin region, projection for $\mathcal{NB}^{\mathrm{TRANS}}$ in signal region on B^-. Red is signal. Magenta is $q\bar{q}$. Yellow is $D^{*0}\pi^{\pm}$. Green is $D^{*\pm}\pi^{\mp}$. Blue is $B\bar{B}$.

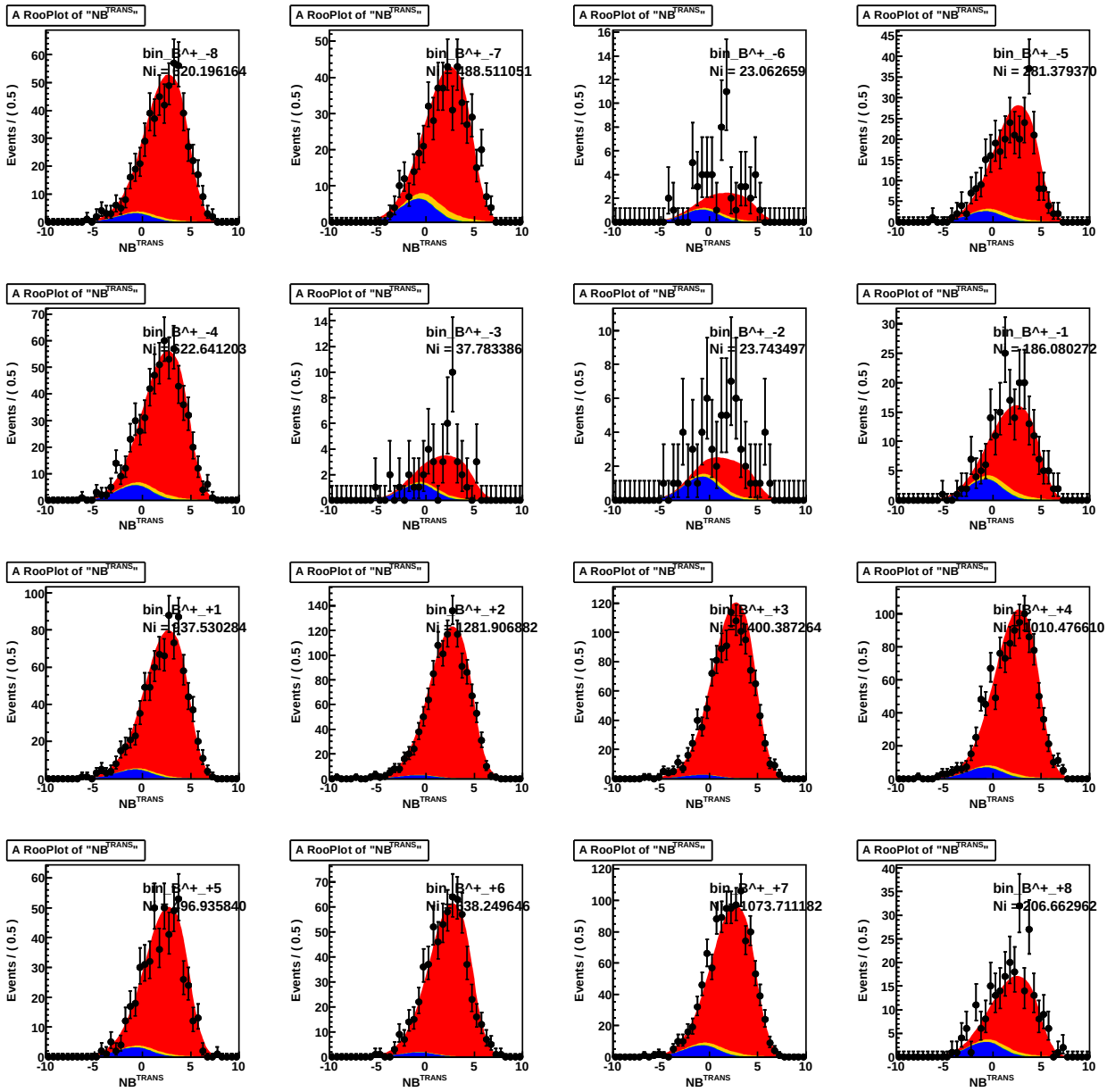

Figure 3.26: $D\pi$ 3D-fit each Dalitz bin region, projection for $\mathcal{NB}^{\mathrm{TRANS}}$ in signal region on B^+. Red is signal. Magenta is $q\bar{q}$. Yellow is $D^{*0}\pi^{\pm}$. Green is $D^{*\pm}\pi^{\mp}$. Blue is $B\bar{B}$.

	$D\pi$ result	Belle charged B 605 fb^{-1} model-independent result [18]
x_-	-0.0142 ± 0.0077	$-0.0045 \pm 0.0087 \pm 0.0056$
y_-	$+0.0010 \pm 0.0076$	$-0.0231 \pm 0.0107 \pm 0.0077$
x_+	-0.0169 ± 0.0083	$-0.0172 \pm 0.0089 \pm 0.0065$
y_+	$+0.0225 \pm 0.0076$	$+0.0129 \pm 0.0103 \pm 0.0088$

Table 3.7: Comparison of $(x,\, y)$ of $D\pi$ result

origin of this difference are

- K_S selection : we employ new K_S finder based on 20 kinematic and detector variables Neurobayes method, previous study used flight length in plane of vertical from beam axis, angle between K_S momentum and direction and K_S invariant mass with cut based.
- $q\bar{q}$ suppression : we employ 12 kinematic variables summarized by neurobayes method, previous study used Fisher discriminant composed of 11 parameters and $\cos\theta_{\rm thr.}$.

Other possibility of difference between my and previous study are

- D^0 mass selection
- Backgrounds distribution in Dalitz plane
- Cross-feed between bins
- Efficiency correction.

However those effect can not explain $(x_-,\, y_-)$ difference. Total signal number is different, our total signal number is $\sum_i N_i = 18571.1 \pm 141.3$, previous one is 19106.2 ± 147.3 events.

We check $D\pi$ $(x,\, y)$ fit validity with 10000 pseudo-experiments which is generated by binned 3D-PDF with random number according to statistical uncertainty. Pseudo-experiments generated as $(x_-,\, y_-,\, x_+,\, y_+) = (0,\, 0,\, 0,\, 0)$. We check two distributions. One is mean distribution of $(x,\, y)$ which is distribution of obtained $(x_{\rm obt.},\, y_{\rm obt.})$ from fit, if fit has no bias, it will have a peak at $(x_{\rm true},\, y_{\rm true})$. Other is pull distribution, it is distribution of

$$\frac{x_{\rm true} - x_{\rm obt.}}{\sigma x_{\rm obt.}}, \tag{3.8}$$

here $\sigma x_{\rm obt.}$ means uncertainty obtained from fit. If fit has no bias, it will be normal standard distribution. For $(x_-,\, y_-,\, x_+,\, y_+)$ each mean and pull distribution are shown in Fig. 3.27. The pull distributions are almost normal standard distribution, so we take the

error of (x, y) as one dimension from likelihood distribution. It seems to be seen small biases on x_- and y_-. In addition that, our $D\pi$ result (statistical uncertainty only) is

$$x_- = -0.0130 \pm 0.0077 \quad (3.9)$$
$$y_- = +0.0018 \pm 0.0076 \quad (3.10)$$
$$x_+ = -0.0169 \pm 0.0083 \quad (3.11)$$
$$y_+ = +0.0225 \pm 0.0076. \quad (3.12)$$

We obtained (x, y) mean value and statistical uncertainty only (did not obtained systematic uncertainty). We have checked the evaluation of this (x, y) fitter.

3.7 (x, y) Fit on DK^{*0} Pseudo-Experiments Sample

To obtain ($x_\pm$, $y_\pm$), binned fit on Dalitz plane is needed. I check two fit strategies, Combined Fit and Separate Fit with pseudo-experiments, generated by PDF with a random number. We check validation of this fitter with toy MC study using pseudo-experiments, from Separate and Combined Fit respectively. Both fit approaches described in Sec. 3.6.1 are used. We check the evaluation, comparison of (x, y) fits and fitter bias.

We generate the events (ϕ_3, r_S, δ_S) = (68°, 0.4, 111°) and $\sum_i (N_i + \bar{N}_i) = 44.2$ situation pesudo-experiments 500 times. Here, (x_-, y_-, x_+, y_+) = (0.293, 0.273, -0.400, 0.007).

3.7.1 Separate Fit

Fig. 3.29 shows mean and pull distribution on $x_\pm$ and $y_\pm$ on $\sum_i (N_i + \bar{N}_i) = 44.2$ statistics situation. Fig. 3.30 shows mean and pull distribution on $x_\pm$ and $y_\pm$ on $\sum_i (N_i + \bar{N}_i) = 1176.5$ (the same as Belle charged $B^\pm \to DK^\pm$ 605 fb^{-1} model-independent result [18]) statistics situation.

3.7.2 Combined Fit

Fig. 3.31 shows mean and pull distribution on $x_\pm$ and $y_\pm$ on $\sum_i (N_i + \bar{N}_i) = 44.2$ statistics situation. Fig. 3.32 shows mean and pull distribution on $x_\pm$ and $y_\pm$ on $\sum_i (N_i + \bar{N}_i) = 1176.5$ statistics situation. We'll adopt the Combined Fit to obtain ($x_\pm$, $y_\pm$) on DK^{*0} data, because it has statistical advantage in small number of signals and many background components than Separate Fit.

3.8 Statistical Uncertainty

We'll adopt the Combine Fit to obtain ($x_\pm$, $y_\pm$) on DK^{*0} data. However Figure 3.31 show that ($x_\pm$, $y_\pm$) error obtained from likelihood fit can not represent statistical uncertainty. If (x, y) fitter can return error which can represent statistical uncertainty, pull distribution should be standard normal distribution. To evaluate statistical uncertainty in (x, y) plane, we make confidence level surface on (x, y) plane with Feldman-Cousins frequentist method. In next section, strategy of this method is described.

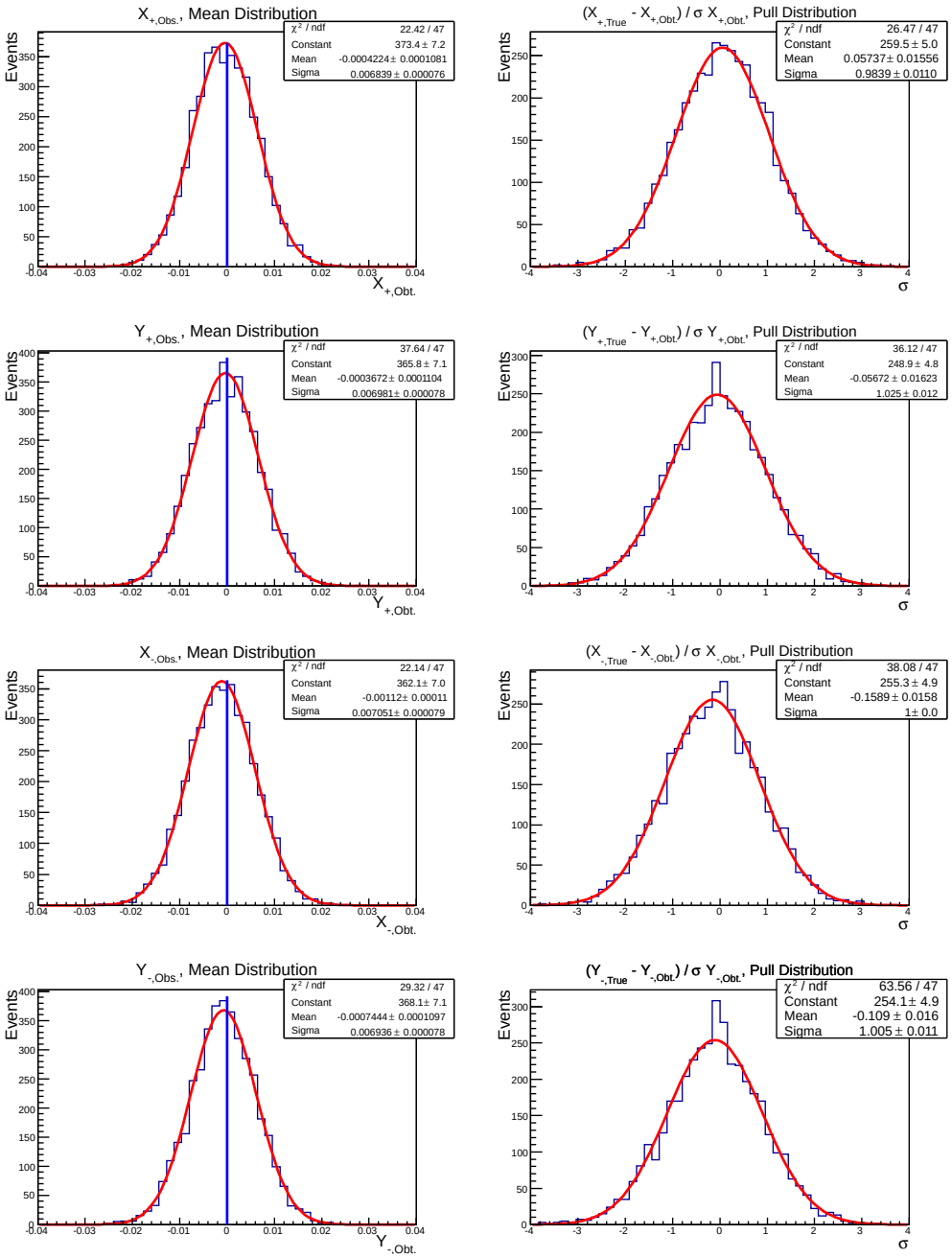

Figure 3.27: (x, y) fit on $D\pi$ 10000 pesudo-experiments mean and pull distributions. Left column are mean and right is pull distributions. Up to down, x_+, y_+, x_- and y_-.

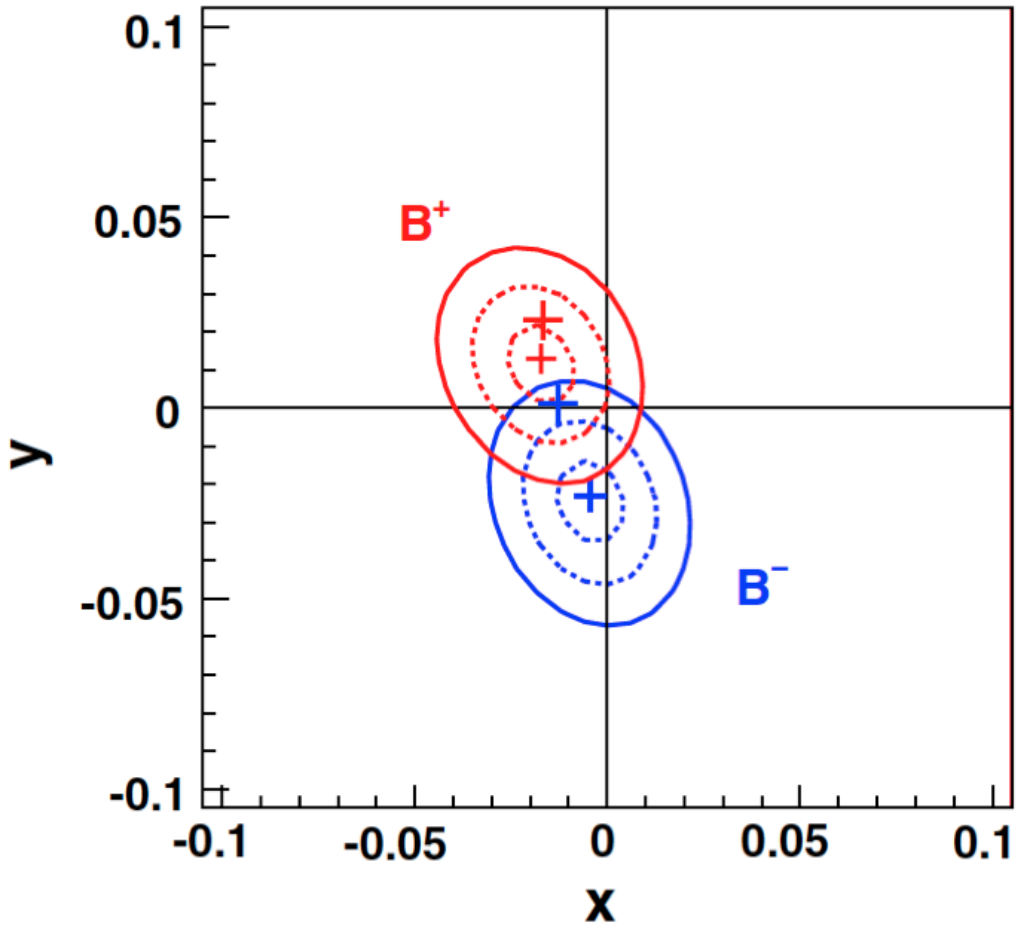

Figure 3.28: (x, y) result (mean value only). error region are previous (x, y) statistical errors (1, 2, 3 σ).

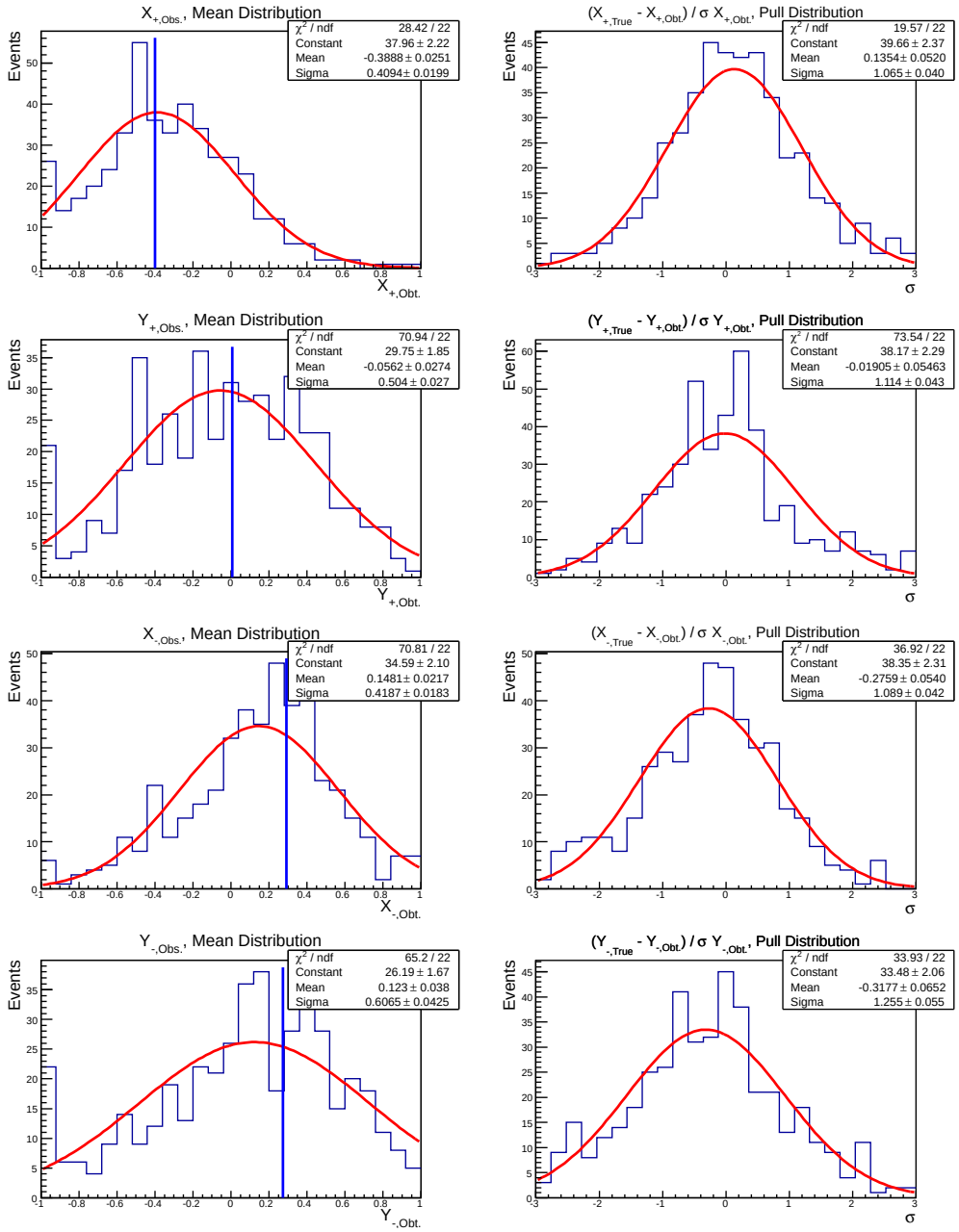

Figure 3.29: Separate Fit on pseudo-experiments results at $\sum_i (N_i + \bar{N}_i) = 44.2$. Left column is mean distributions. Right is pull distributions. Up to down are x_+, y_+, x_- and y_-.

3.8.1 Feldman-Cousin Method

To obtain statistical uncertainty on (x, y), Feldman-Cousins method is applied. If (x, y) has some biases, it can be also evaluated by this method. We adopt the Feldman-Cousins frequentist approach which is based on the likelihood-ratio ordering principle to obtain

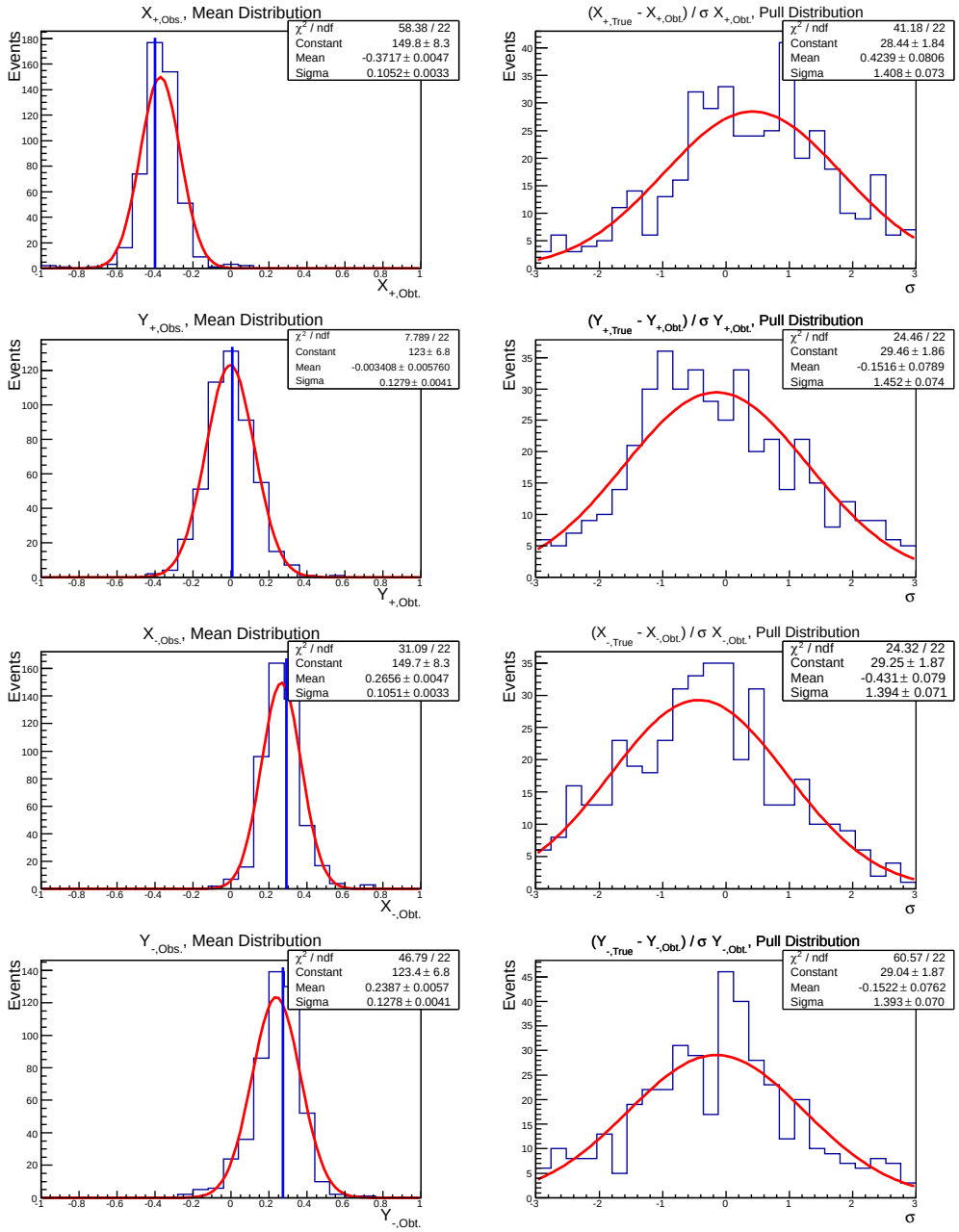

Figure 3.30: Separate Fit on pseudo-experiments results at $\sum_i (N_i + \bar{N}_i) = 1176.5$. Left column is mean distributions. Right is pull distributions. Up to down are x_+, y_+, x_- and y_-.

the confidence regions x[-2., 2.], y[-2., 2.]. Detail explanation is below.

The method, used for the determination of the two-dimensional confidence regions x and y, is an extension of that for the one-dimensional case. Therefore we first explain how we obtain the confidence intervals for x; the intervals for y are obtained in a similar

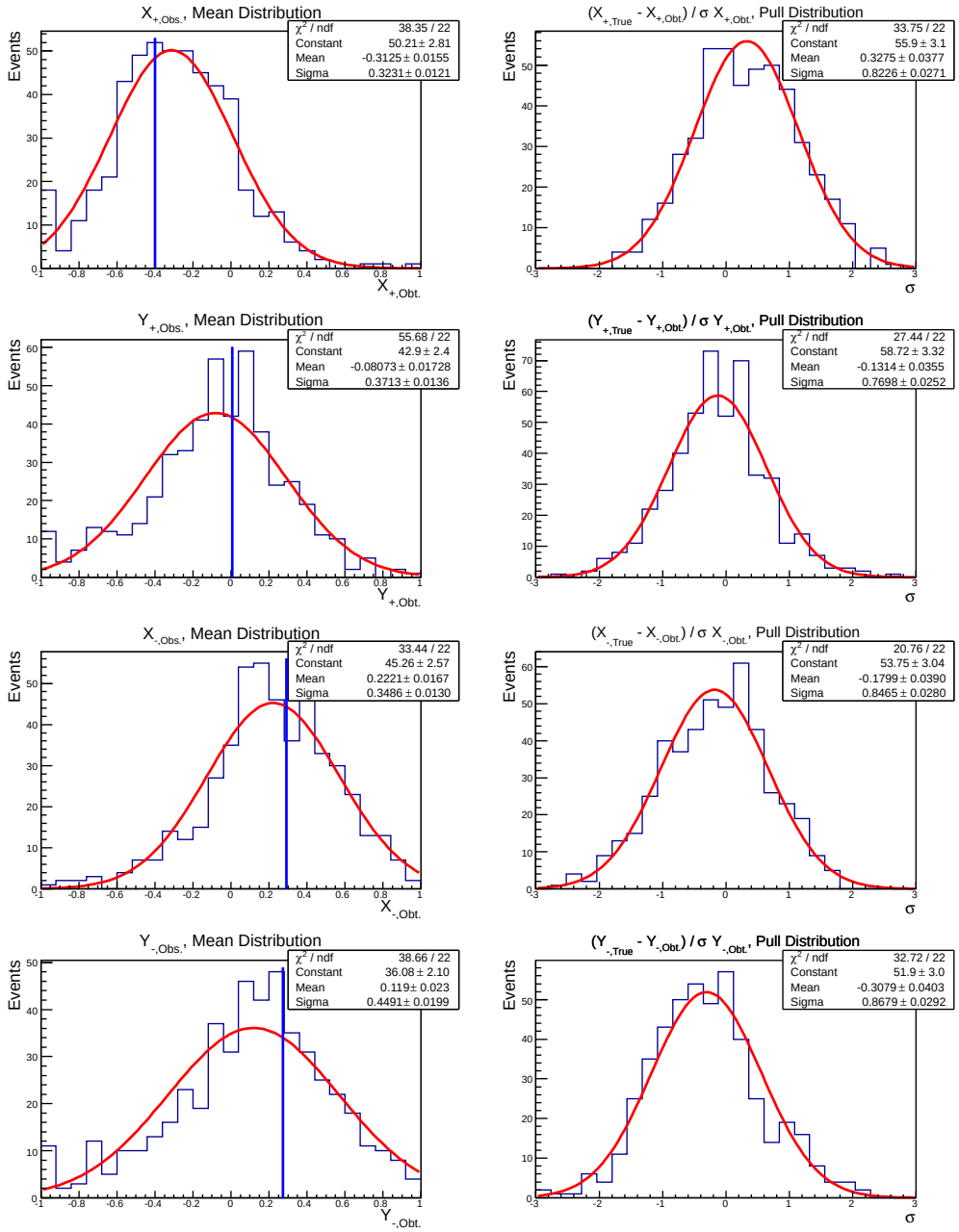

Figure 3.31: Combine fit on pseudo-experiments results at $\sum_i (N_i + \bar{N}_i) = 44.2$. Left column is mean distributions. Right is pull distributions. Up to down are x_+, y_+, x_- and y_-.

way.

We generate > 20000 pseudo-experiments generated from binned-3D-PDF using random number according to statistical uncertainty, for 1681 sets of (x_{true}, y_{true}) values that cover the entire regions x_{true}[-2., 2.], y_{true}[-2., 2.]. The fit to each set of experiments distri-

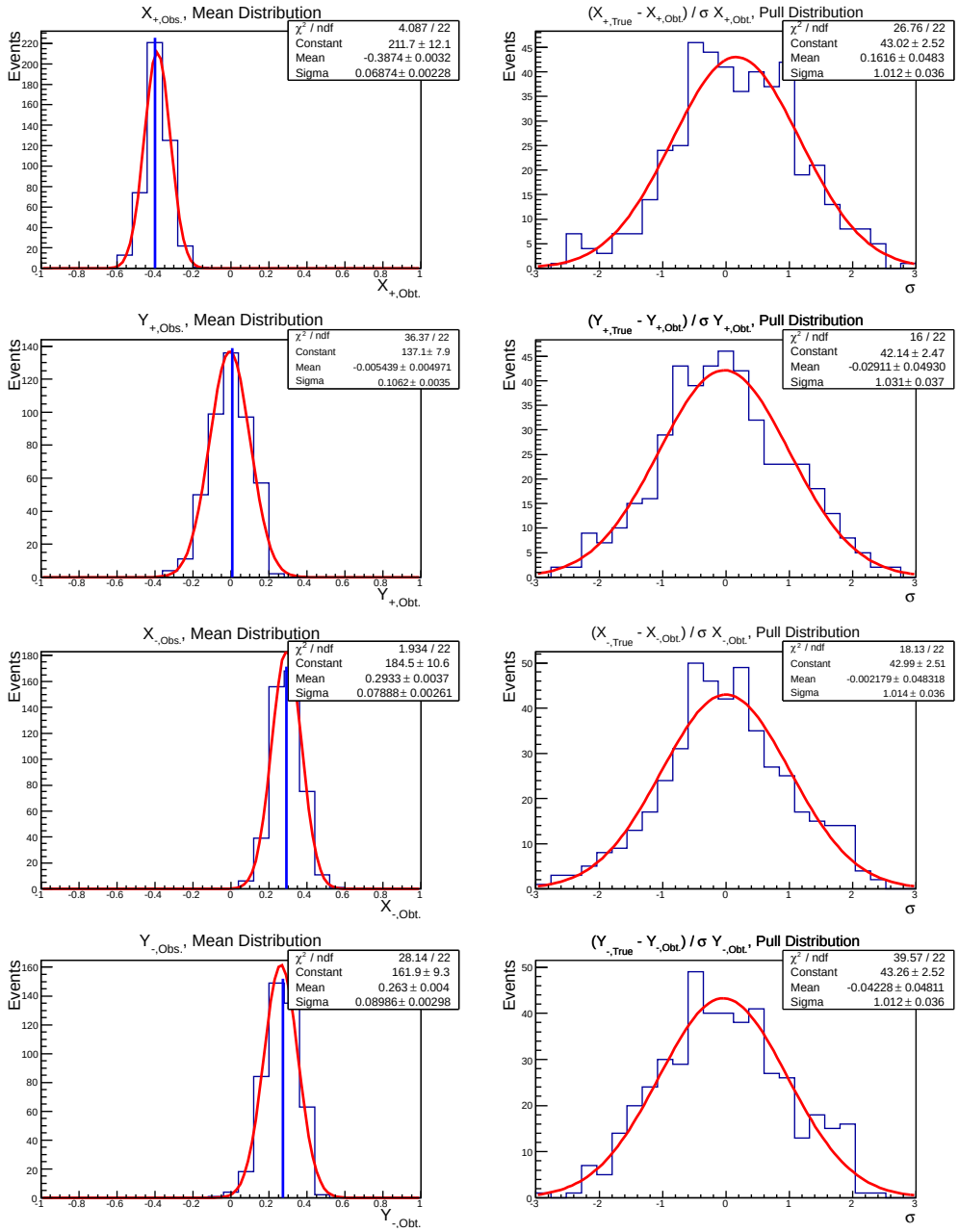

Figure 3.32: Combine fit on pseudo-experiments results at $\sum_i (N_i + \bar{N}_i) = 1176.5$. Left column is mean distributions. Right is pull distributions. Up to down are x_+, y_+, x_- and y_-.

bution an $x_{\text{obt.}}$ that depends on input x_{true} value. To account for this dependence, we use a smoothed histogram PDF for $x_{\text{obt.}}$ by Kernel estimation [40] which is way of evaluation

of distribution from n sets obtained observables,

$$PDF(x_{\rm obt.}) = \frac{1}{nh}\sum_{i=1}^{n} K(\frac{x_{\rm obt.} - x_{{\rm obt.}i}}{\rho}), \tag{3.13}$$

here

$$K(x) = \frac{1}{\sqrt{2\pi}} e^{-\frac{1}{2}x^2}, \tag{3.14}$$

ρ is called scaled kernel, the parameter of smoothing. Figure 3.33 show the distributions and the $x_{\rm obt.}$ PDF for the cases $(x_{\rm true}, y_{\rm true}) = (-0.4, 0.0)$ and $(x_{\rm true}, y_{\rm true}) = (0.3, 0.3)$, respectively. When $(x, y)_{\rm obt.}$ are smoothed, the parameters ρ is selected by $(x, y)_{\rm obt.}$ RMS. The PDFs are in good agreement with the distribution of the pseudo-experiments in both case.

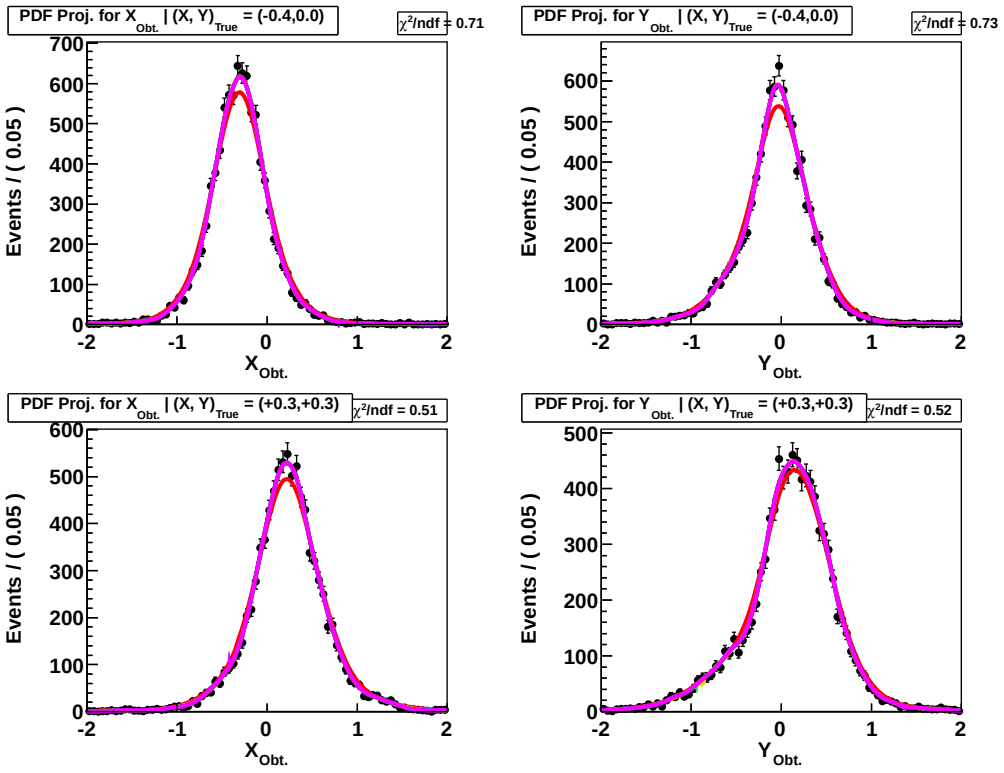

Figure 3.33: $(x, y)_{\rm obt.}$ distributions (dot) and smoothed histogram PDF(solid lines (red, orange, green, blue, magenta : $\rho = 1, 0.5, 0.25, 0.01, 0.001$)) projected for x (left) and y (right). However $\rho < 0.5$ lines are overlapping because in those distributions ρ value is enough small at 0.5. In this study, smoothing parameter is selected by $(x, y)_{\rm obt.}$ RMS. Upper(lower) are $(x, y)_{\rm true}$ = (-0.4, 0.0)(0.3, 0.3).

The acceptance region $[x_{\rm obt.1}, x_{\rm obt.2}]$ for a given x and a confidence level $\alpha(x)$ is defined by:

$$\alpha(x) = \int_{x_{\rm obt.1}}^{x_{\rm obt.2}} dx_{\rm obt.} PDF(x_{\rm obt.}|x_{\rm true}) \tag{3.15}$$

Upon performing an experiment to measure x and obtaining a value x_0, we can determine the region in which the condition $x_1 < x_0 < x_2$ is satisfied

$$PDF(x|x_{\text{true}}) > PDF(x_0|x_{\text{true}}) \tag{3.16}$$

in x_{true} space. The region is confidence interval that has a confidence level equal to α. Figure 3.34 shows the confidence interval surface when $(x, y)_0 = (0., 0.), (-0.4, 0.)$ is obtained from data fit. From this method, we can obtain the statistical uncertainty of (x, y) including fit bias which include $(x,\ y)$ data fit.

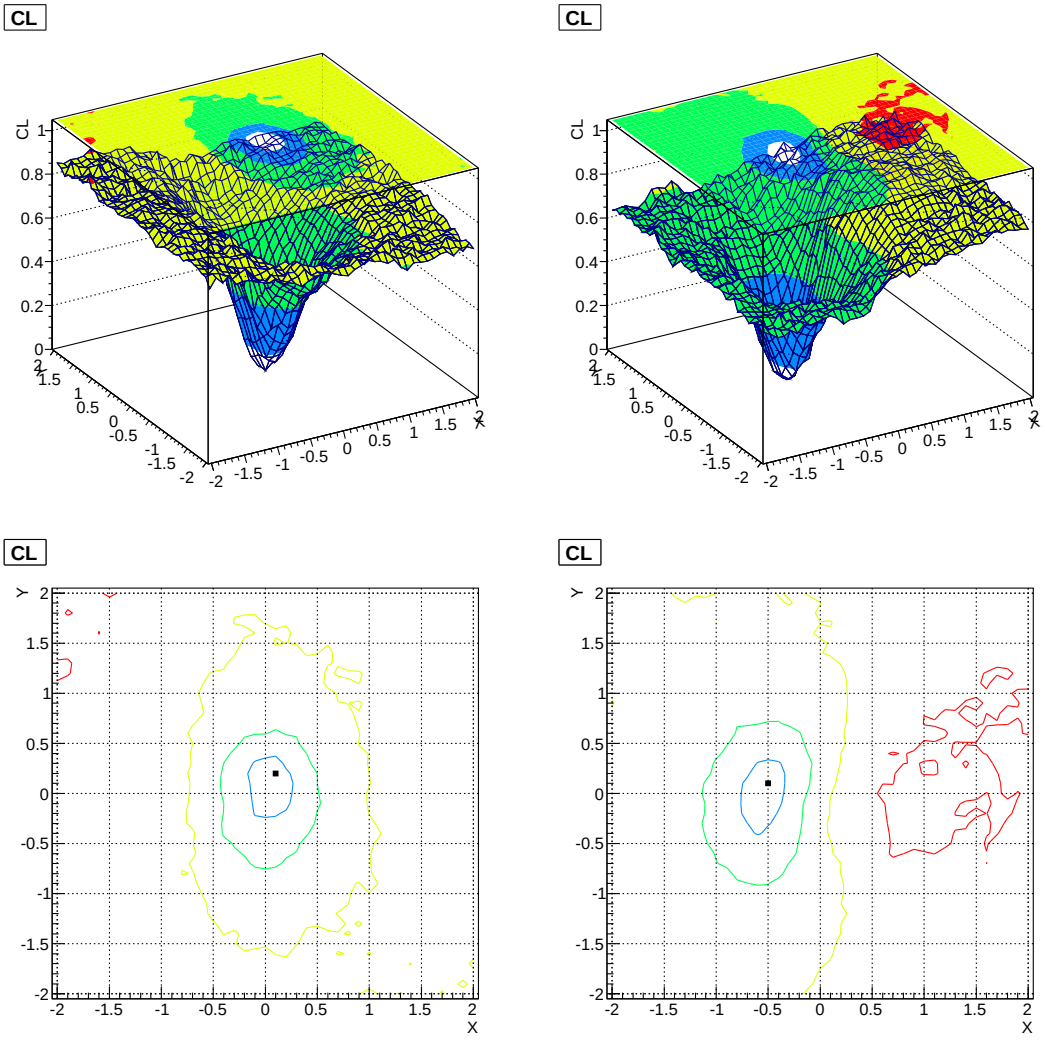

Figure 3.34: Confidence level surface at $(x, y)_{\mathrm{data}}$ = (0., 0.)(left), (-0.4, 0.)(right). For upper surface figures,

- white region shows C.L. $<$ 11.8 % ($<$ 0.5 σ, σ means 2D-standard-deviation),
- blue region shows C.L. $<$ 39.3 % ($<$ 1.0 σ),
- green region shows C.L. $<$ 67.5 % ($<$ 1.5 σ),
- yellow region shows C.L. $<$ 86.5 % ($<$ 2.0 σ),
- red region shows C.L. $>$ 86.5 % ($>$ 2.0 σ).

For lower lines figures,

- dot shows most probably (x, y),
- dark blue line shows C.L. = 11.8 % (0.5 σ),
- green line shows C.L. = 39.3 % (1.0 σ),
- yellow line shows C.L. = 67.5 % (1.5 σ),
- red line shows C.L. = 86.5 % (2.0 σ).

Chapter 4

Result

4.1 (x, y) Fit on DK^{*0} Real Data

We performed (x, y) fit on real data DK^{*0}. The fit strategy is same as on $D\pi$ control samples one. We obtained (x, y) as

$$
\begin{aligned}
x_- &= +0.29^{+0.45}_{-0.42} && (4.1)\\
y_- &= -0.33^{+0.51}_{-0.54} && (4.2)\\
\mathrm{corr.}(x_-, y_-) &= +7.0\% && (4.3)\\
x_+ &= +0.07^{+0.55}_{0.40} && (4.4)\\
y_+ &= +0.05^{+0.51}_{0.63} && (4.5)\\
\mathrm{corr.}(x_+, y_+) &= -7.5\% && (4.6)
\end{aligned}
$$

however we use Feldman-Cousin method to obtain statistical uncertainty, instead of this uncertainty as described in Sec.3.8. Projection for each parameter of binned-3D-fit are shown as Fig. 4.2 - 4.7. We obtain statistical uncertainty as shown Fig. 4.8.

4.2 Systematic Uncertainty

Systematic errors in the (x, y) on $B^0 \to DK^{*0}$ real data are obtained for the default procedure of the Combined Fit with fluctuation according to uncertainty. The systematic uncertainties are summarized in Table 4.1.

1) The uncertainty due to the efficiency variations are treated by smearing the numbers of events in the flavor sample K_i by 1.5 % [18] (the amount of difference between the $B^+ \to D\pi^+$ and flavor samples) and preforming the (x, y) fits. The uncertainty is obtained from the maximum of two quantities:

   - RMS of x and y from smearing the numbers of events in the flavor sample K_i by 1.5%.
   - Bias of x and y between the fits with and without efficiency correction for K_i obtained from signal MC,

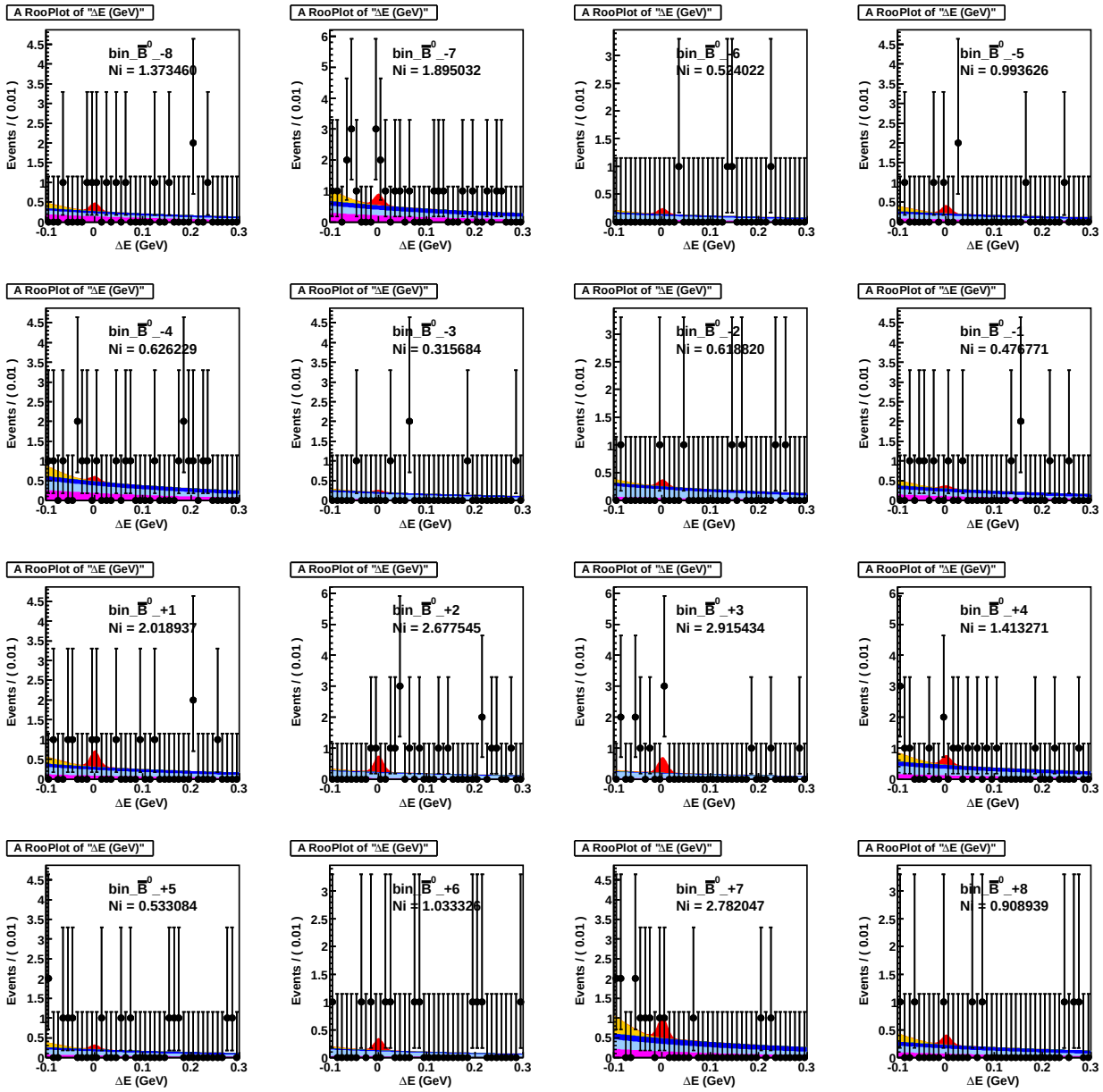

Figure 4.1: 3D fit with Dalitz binning $\bar{B}^0$ ΔE

Figure 4.2: DK^{*0} 3D-fit each Dalitz bin region, projection for ΔE in signal region on $\bar{B}^0$. Red is signal. Dark blue is $B\bar{B}$ real D. Light blue is $B\bar{B}$ fake D. Magenta is $q\bar{q}$. Yellow is $D^0\rho^0$. Green is $D^0a_1^+$.

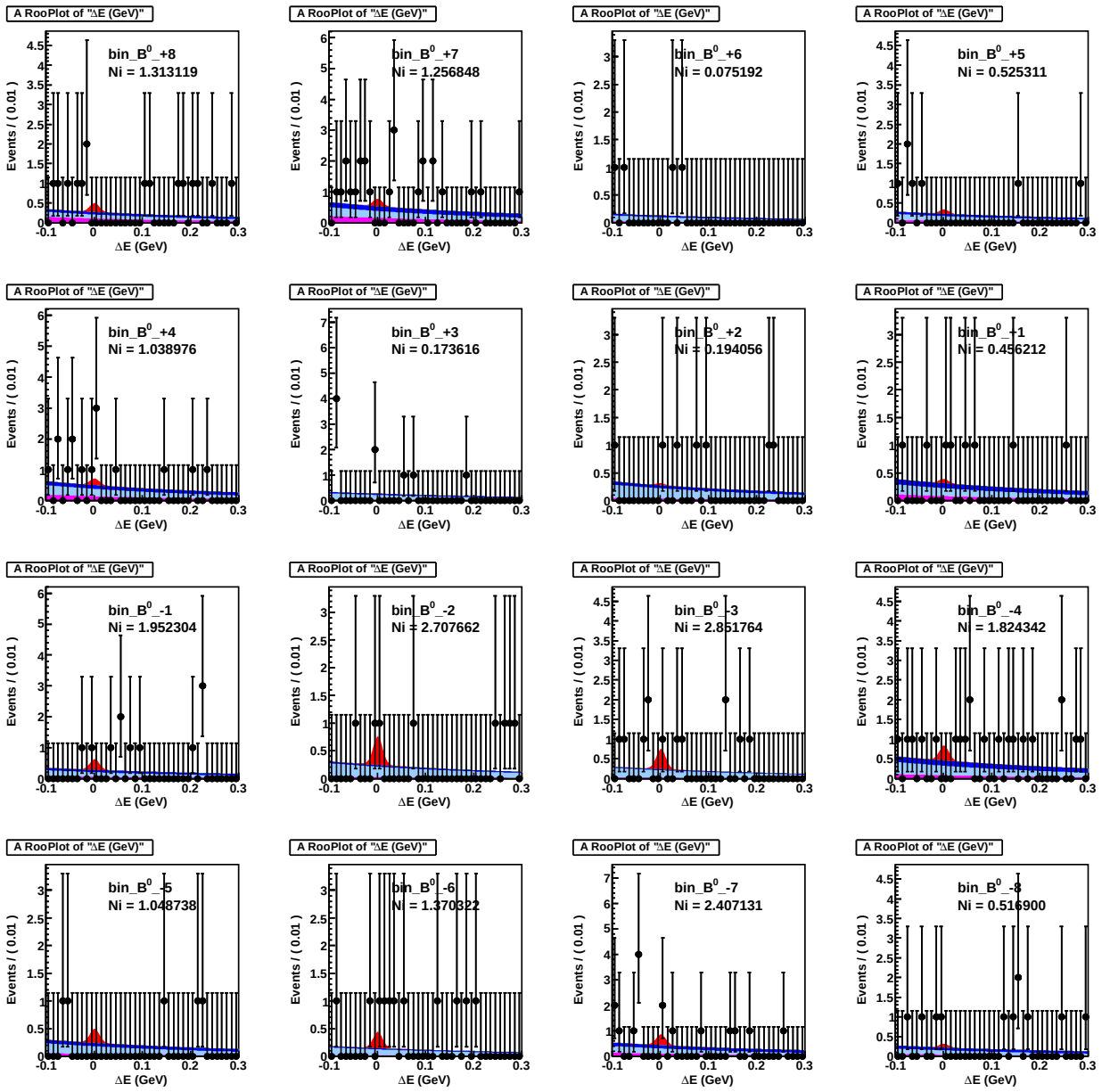

Figure 4.3: DK^{*0} 3D-fit each Dalitz bin region, projection for ΔE in signal region on B^0. Red is signal. Dark blue is $B\bar{B}$ real D. Light blue is $B\bar{B}$ fake D. Magenta is $q\bar{q}$. Yellow is $D^0\rho^0$. Green is $D^0a_1^+$.

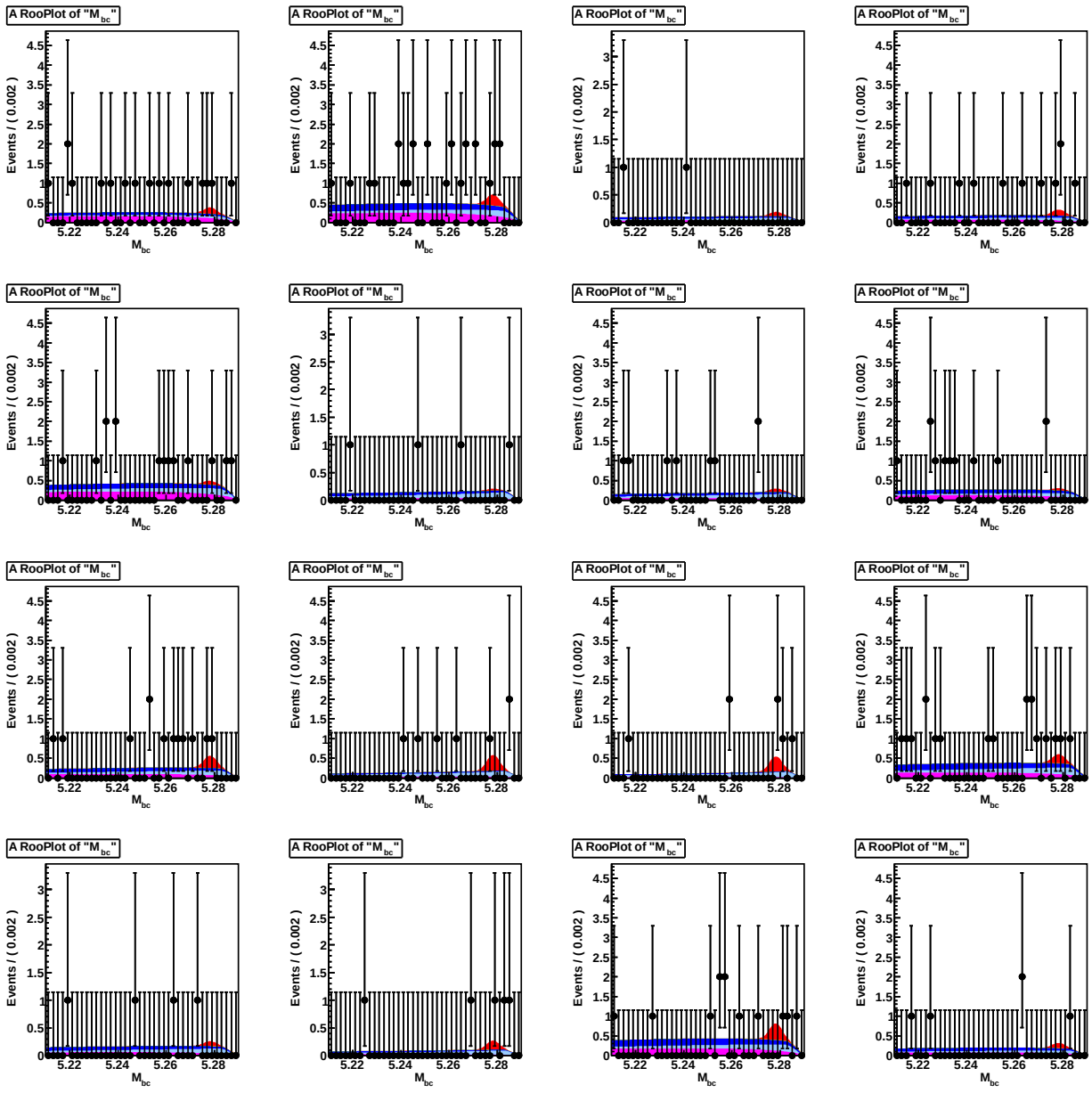

Figure 4.4: DK^{*0} 3D-fit each Dalitz bin region, projection for $m_{\rm bc}$ in signal region on $\bar{B}^0$. Red is signal. Dark blue is $B\bar{B}$ real D. Light blue is $B\bar{B}$ fake D. Magenta is $q\bar{q}$. Yellow is $D^0\rho^0$. Green is $D^0a_1^+$.

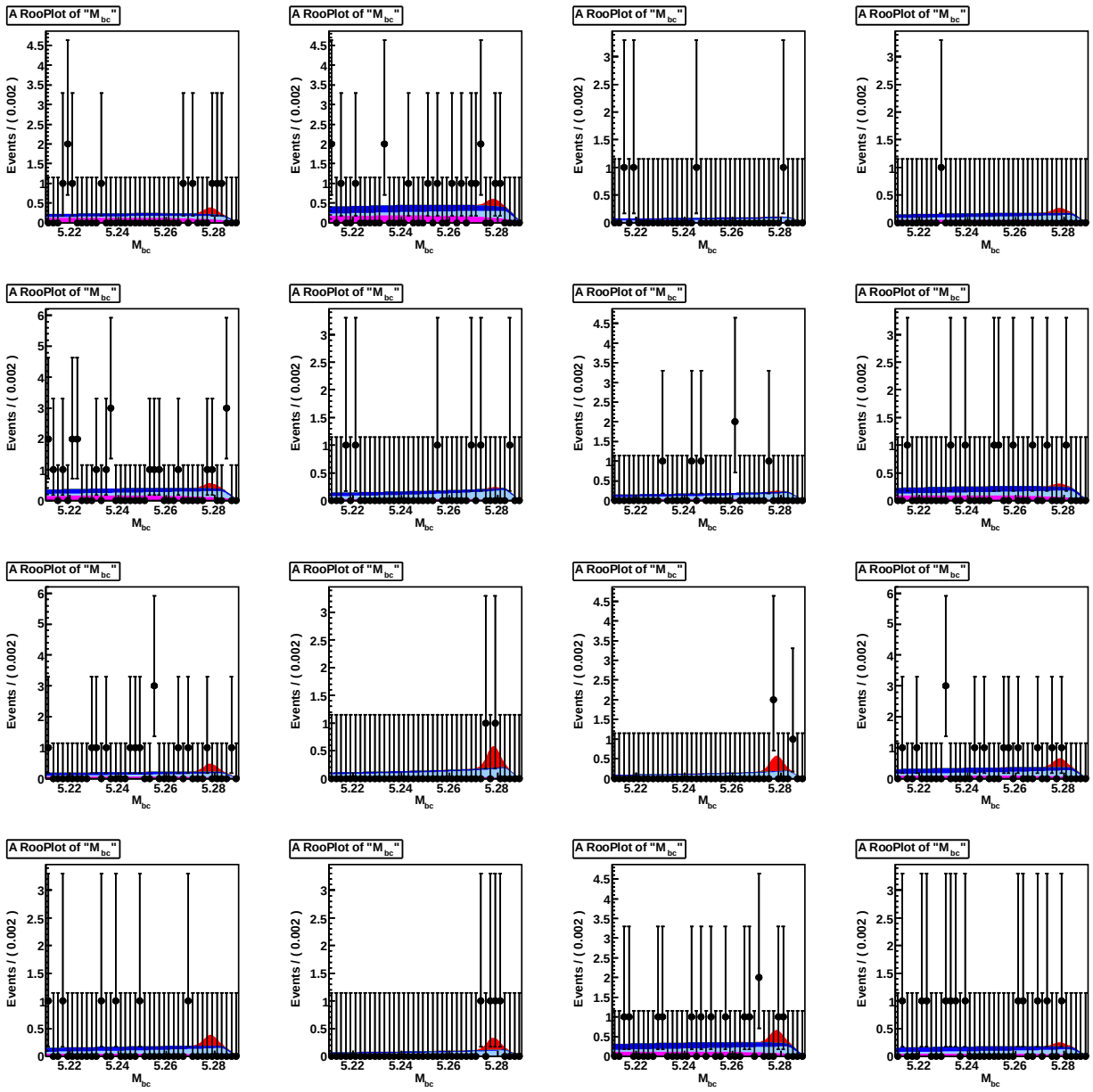

Figure 4.5: DK^{*0} 3D-fit each Dalitz bin region, projection for $m_{\rm bc}$ in signal region on B^0. Red is signal. Dark blue is $B\bar{B}$ real D. Light blue is $B\bar{B}$ fake D. Magenta is $q\bar{q}$. Yellow is $D^0\rho^0$. Green is $D^0a_1^+$.

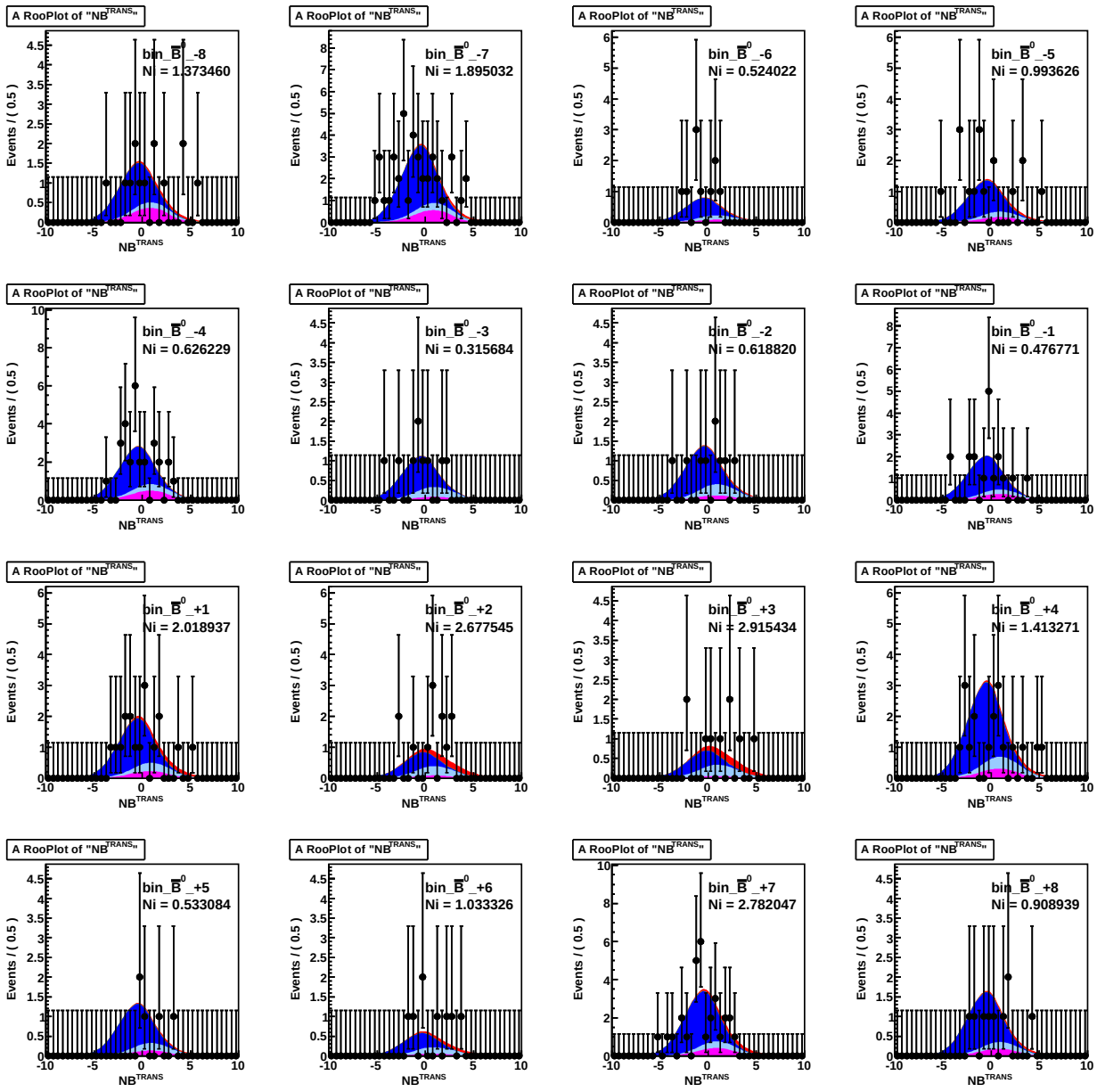

Figure 4.6: DK^{*0} 3D-fit each Dalitz bin region, projection for $\mathcal{NB}^{\mathrm{TRANS}}$ in signal region on $\bar{B}^0$. Red is signal. Dark blue is $B\bar{B}$ real D. Light blue is $B\bar{B}$ fake D. Magenta is $q\bar{q}$. Yellow is $D^0\rho^0$. Green is $D^0a_1^+$.

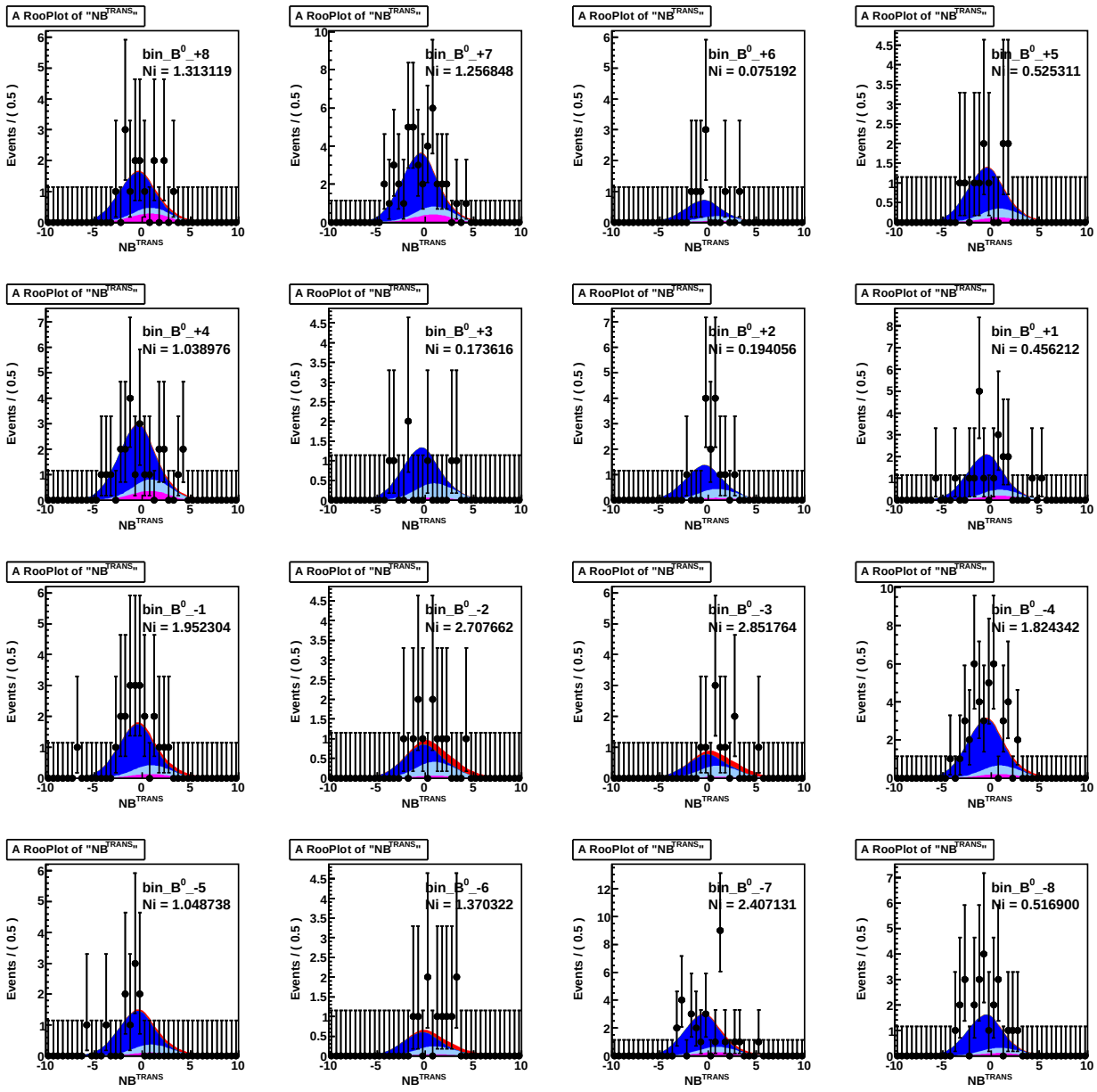

Figure 4.7: DK^{*0} 3D-fit each Dalitz bin region, projection for $\mathcal{NB}^{\mathrm{TRANS}}$ in signal region on B^0. Red is signal. Dark blue is $B\bar{B}$ real D. Light blue is $B\bar{B}$ fake D. Magenta is $q\bar{q}$. Yellow is $D^0\rho^0$. Green is $D^0a_1^+$.

Source of uncertainty	Δx_-	Δy_-	Δx_+	Δy_+
1) Dalitz plots efficiency	± 0.00	$^{+0.01}_{-0.00}$	± 0.01	$^{+0.00}_{-0.01}$
2) Crossfeed between bins	± 0.00	$^{+0.01}_{-0.00}$	$^{+0.01}_{-0.00}$	± 0.00
3) PDF shape	$^{+0.01}_{-0.07}$	$^{+0.07}_{-0.01}$	$^{+0.01}_{-0.10}$	$^{+0.04}_{-0.06}$
Signal shape	± 0.00	± 0.00	± 0.00	± 0.00
$B\bar{B}$ shape	$^{+0.01}_{-0.07}$	$^{+0.07}_{-0.01}$	$^{+0.01}_{-0.10}$	$^{+0.04}_{-0.06}$
$q\bar{q}$	± 0.00	± 0.00	± 0.00	$^{+0.00}_{-0.01}$
$D^0\rho^0$ shape	± 0.00	± 0.00	± 0.00	$^{+0.00}_{-0.01}$
$D^0 a_1^+$ shape	± 0.00	$^{+0.00}_{-0.01}$	± 0.00	± 0.00
4) Fit bias	± 0.00	± 0.00	± 0.00	± 0.00
5) Flavor-tagged statistics	± 0.00	± 0.00	± 0.00	$^{+0.00}_{-0.01}$
6) c_i, s_i precision	± 0.03	$^{+0.09}_{-0.08}$	± 0.05	$^{+0.08}_{-0.10}$
7) k precision	± 0.00	± 0.01	± 0.00	± 0.00
Total without c_i, s_i precision	$^{+0.01}_{-0.07}$	$^{+0.07}_{-0.02}$	$^{+0.02}_{-0.10}$	$^{+0.04}_{-0.06}$
Total	$^{+0.03}_{-0.08}$	$^{+0.12}_{-0.08}$	$^{+0.05}_{-0.11}$	$^{+0.09}_{-0.12}$

Table 4.1: Systematic uncertainties in the (x, y) measurement for $B^0 \to DK^{*0}$ mode.

and obtained (± 0.00, $^{+0.01}_{-0.00}$, ± 0.01, $^{+0.00}_{-0.01}$) for (x_-, y_-, x_+, y_+).

2) The uncertainty due to cross-feed between bins is estimated by the bias of x and y between the fits with and without cross-feed correction. We obtain the uncertainty due to it as (± 0.00, $^{+0.01}_{-0.00}$, $^{+0.01}_{-0.00}$, ± 0.00).

3) The uncertainties due to fixed parametrization of the signal and background PDFs are estimated by varying them by $\pm 1\sigma$. The uncertainty of $\mathcal{NB}^{\rm TRANS}$ PDF distributions for $B\bar{B}$ are estimated by replacing signal $\mathcal{NB}^{\rm TRANS}$ PDF. It is largest uncertainty except for c_i and s_i. The uncertainty due to real D and fake D $B\bar{B}$ fraction is estimated by varying then from 0 to 1. Obtained uncertainties due to signal, $B\bar{B}$, $q\bar{q}$, $D^0\rho^0$ and $D^0 a_1^+$ PDFs are (± 0.00, ± 0.00, ± 0.00, ± 0.00), ($^{+0.01}_{-0.07}$, $^{+0.07}_{-0.01}$, $^{+0.01}_{-0.10}$, $^{+0.04}_{-0.06}$), (± 0.00, ± 0.00, ± 0.00, $^{+0.00}_{-0.01}$), (± 0.00, ± 0.00, ± 0.00, $^{+0.00}_{-0.01}$) and (± 0.00, $^{+0.00}_{-0.01}$, ± 0.00, ± 0.00) respectively.

4) The uncertainty due to errors of K_i from tagged $D \to K_S\pi\pi$ statistics is obtained by smearing the K_i value within their errors. For now, we do not take correlations into account. Obtained uncertainty due to K_i is (± 0.00, ± 0.00, ± 0.00, $^{+0.00}_{-0.01}$).

5) The uncertainty due to errors of c_i and s_i parameters is obtained by smearing the c_i and s_i values within their total errors. For now, we do not take correlations into account. Obtained uncertainty due to c_i and s_i is (± 0.03, $^{+0.09}_{-0.08}$, ± 0.05, $^{+0.08}_{-0.10}$).

6) The uncertainty due to errors of k from BaBar MC study is obtained by smearing the k value within their errors. BaBar reported in [19], k should be 0.95 ± 0.03. Obtained uncertainty due to k is (± 0.00, ± 0.01, ± 0.00, ± 0.00).

misc.) The uncertainty due to the bias of (x, y) fit are zero in this analysis. Those detail are in Sec. 3.8.1. statistical uncertainty of (x, y) are included fit bias.

We obtain the systematic uncertainty for ($x_\pm$, $y_\pm$) as shown as Table 4.2. Fig. 4.9

	Mean value	Stat.	Syst. w/o c_i, s_i	c_i,s_i
x_-	$+0.4$	$^{+1.0}_{-0.6}$	$^{+0.0}_{-0.1}$	± 0.0
y_-	-0.6	$^{+0.8}_{-1.0}$	$^{+0.1}_{-0.0}$	± 0.1
x_+	$+0.1$	$^{+0.7}_{-0.4}$	$^{+0.0}_{-0.1}$	± 0.1
y_+	$+0.3$	$^{+0.5}_{-0.8}$	$^{+0.0}_{-0.1}$	± 0.1

Table 4.2: Result of ($x_\pm$, $y_\pm$).

show C.L. surface uncertainty combined statistic and systematics. Here we assume that statistical uncertainties are 2D Gaussian that width is according to statistical uncertainty values.

4.3 Physical Parameter Extraction

We obtain the confidence level projected for r_S direction with frequentist method. It is almost similar to one dimensional Feldman-Cousin method. We assume the ($x_{\rm obt.}$, $y_{\rm obt.}|x_{\rm true}$, $y_{\rm true}$) distribution as the probability distribution $p(z_{\rm obt.}|z_{\rm ture})$. Here $z = (x_-$, y_-, x_+, $y_+)$, the observed parameters. We can obtain the confidence level $\alpha(\mu)$ as,

$$\alpha(\mu) = \frac{\int_{\mathcal{D}(\mu)} p(z|\mu)dz}{\int_\infty p(z|\mu)dz} \tag{4.7}$$

here $p(z|\mu)$ is the probability density to obtain the measurement result z given the set of physics parameters μ. The integration domain $\mathcal{D}(\mu)$ is given by the Feldman-Cousins ordering:

$$\frac{p(z|\mu)}{p(z|\mu_{\rm best}(z))} > \frac{p(z_0|\mu)}{p(z_0|\mu_{\rm best}(z_0))} \tag{4.8}$$

here $\mu_{\rm best}(z)$ is μ that maximizes $p(z|\mu)$ for the given z, and z_0 is the result of the data fit. As a result of this procedure, we obtain the C.L. for the physical parameter r_S as shown in Fig. 4.10.

Systematic uncertainties are included with convolution to $p(z)$ distribution as Gaussian (its width are according to systematic uncertainty). In this calculation we assume that the systematic uncertainties are uncorrelated. The final results are:

$$r_S \ < \ 0.87 \quad (\text{at } 68\ \%\ \text{C.L.}). \tag{4.9}$$

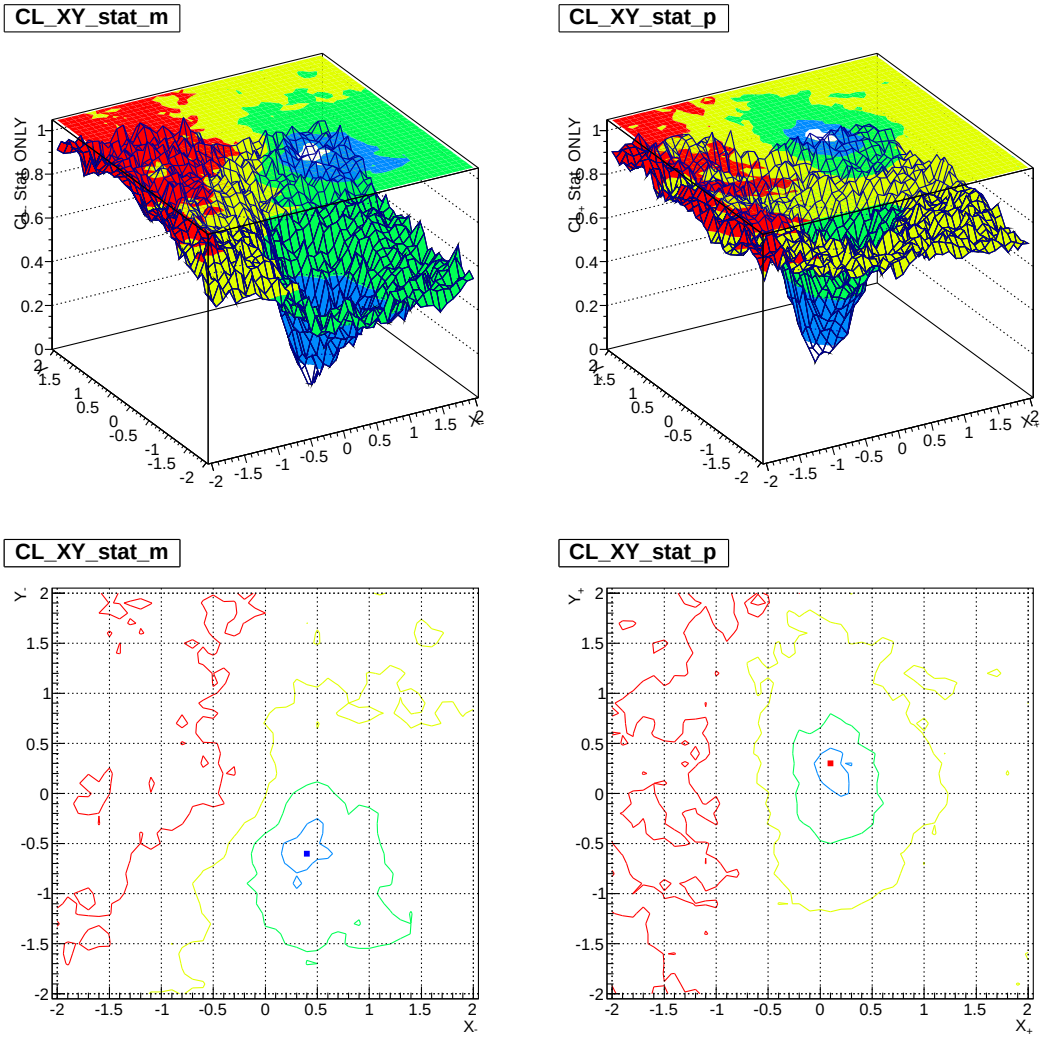

Figure 4.8: Confidence level surface at $(x, y)_-$ ($\bar{B}^0$, left) and $(x, y)_+$ (B^0, right). For upper surface figures,

- white region shows C.L. < 11.8 % ($< 0.5\ \sigma$, σ means 2D-standard-deviation),
- blue region shows C.L. < 39.3 % ($< 1.0\ \sigma$),
- green region shows C.L. < 67.5 % ($< 1.5\ \sigma$),
- yellow region shows C.L. < 86.5 % ($< 2.0\ \sigma$),
- red region shows C.L. > 86.5 % ($> 2.0\ \sigma$).

For lower lines figures,

- dot shows most probably (x, y),
- dark blue line shows C.L. $= 11.8$ % ($0.5\ \sigma$),
- green line shows C.L. $= 39.3$ % ($1.0\ \sigma$),
- yellow line shows C.L. $= 67.5$ % ($1.5\ \sigma$),
- red line shows C.L. $= 86.5$ % ($2.0\ \sigma$).

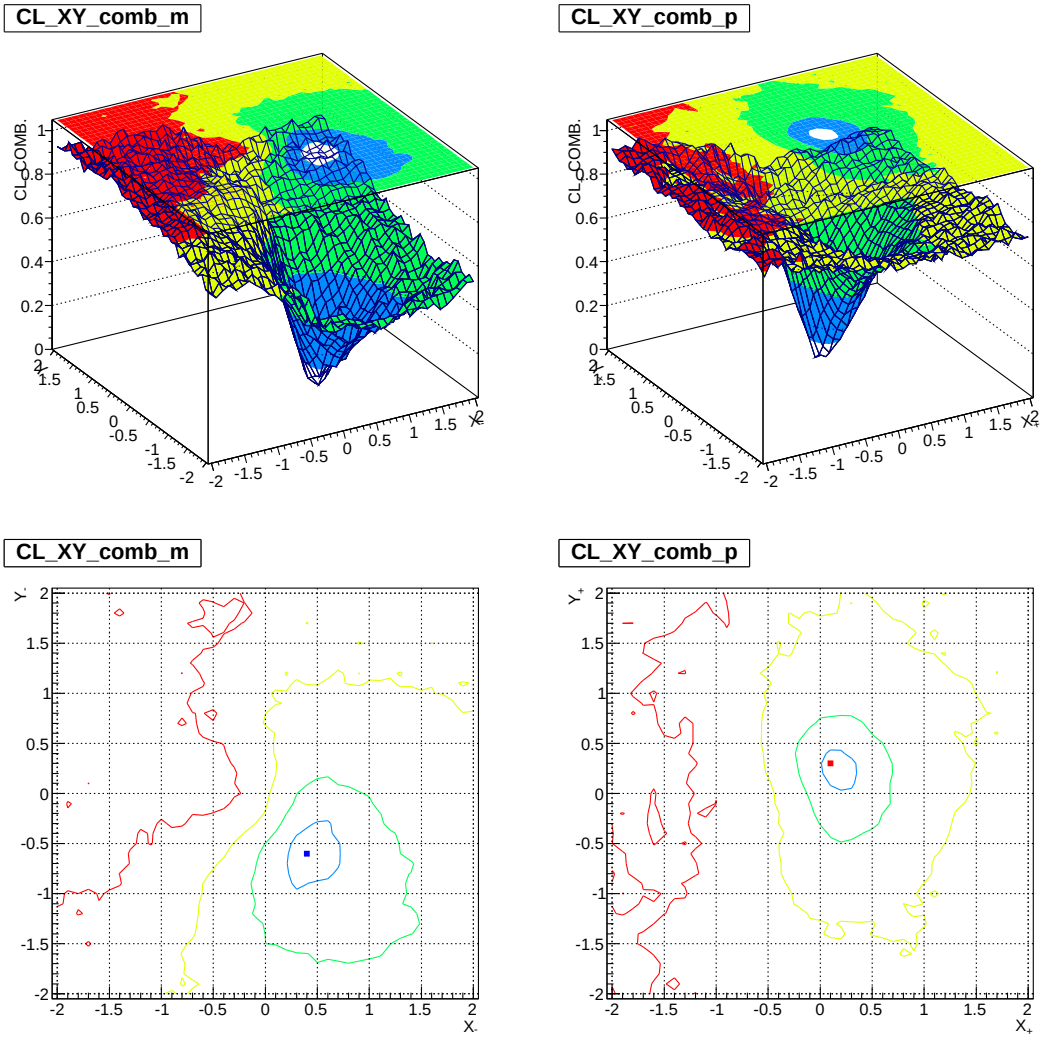

Figure 4.9: Confidence level surface including statistic and systematic uncertainty at (x, y)$_-$ ($\bar{B}^0$, left) and (x, y)$_+$ (B^0, right).
For upper surface figures,

- white region shows C.L. $<$ 11.8 % ($<$ 0.5 σ, σ means 2D-standard-deviation),
- blue region shows C.L. $<$ 39.3 % ($<$ 1.0 σ),
- green region shows C.L. $<$ 67.5 % ($<$ 1.5 σ),
- yellow region shows C.L. $<$ 86.5 % ($<$ 2.0 σ),
- red region shows C.L. $>$ 86.5 % ($>$ 2.0 σ).

For lower lines figures,

- dot shows most probably (x, y),
- dark blue line shows C.L. = 11.8 % (0.5 σ),
- green line shows C.L. = 39.3 % (1.0 σ),
- yellow line shows C.L. = 67.5 % (1.5 σ),
- red line shows C.L. = 86.5 % (2.0 σ).

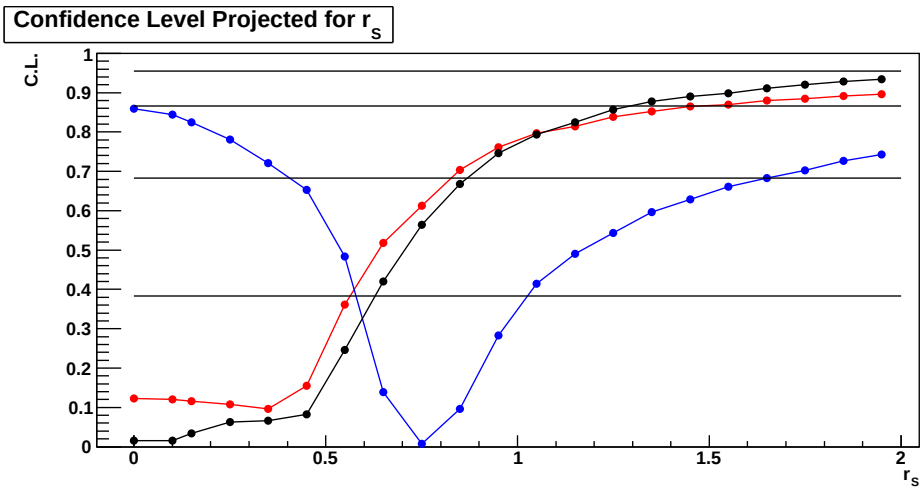

Figure 4.10: Confidence level value on r_S. Red plots are B^0 (x_+, y_+). Blue plots are $\bar{B}^0$ (x_-, y_-). Black plots are combined. Horizontal black lines mean 38 % (according to 0.5 standard deviation), 68 % (1.0 σ), 86 % (1.5 σ), 95 % (2.0 σ).

Chapter 5

Discussion

This study is performed for the purpose of the measurement of ϕ_3. There is no ϕ_3 measurement from neutral B only. When the ϕ_3 is extracted, we simultaneously extract r_S and δ_S, here r_S is the ratio of amplitudes $B^0 \to D^0 K^{*0}$ suppressed decay and $B^0 \to \bar{D}^0 K^{*0}$ favored decay. $B^0 \to D^0 K^{*0}$ suppressed mode decays through $b \to u$ transition. So suppressed decay has ϕ_3 information. Neutral B decay modes are expected to have larger r_S value than r_B in charged B. ϕ_3 precision capped as $1/r$ (r is r_B or r_S). r_S value has not been measured non-zero value due to $B^0 \to DK^{*0}$ small statistics and large background contribution, including this study. (Hoever $\bar{B}^0$ mode indicates non-zero r_S.) One of its causes is small statistics of $B^0 \to DK^{*0}$ decay. In this study, $B^0 \to DK^{*0}$ statistical significance is 2.8 σ as $44.2^{+13.3}_{-12.1}$ events are observed. It is less than expectation from BaBar 371×10^6 $B\bar{B}$ result [41] (39 ± 9) or world average, we expect that signal number from BaBar and W.A. are

- (From BaBar) 78 events
  (This value includs interference effect $B^0 \to D^0 K^{*0}$ and $B^0 \to \bar{D}^0 K^{*0}$.
  Backgrounds events are expected larger than BaBar due to PID.)

- (From W.A.) 64 events
  (This value does not include interference.).

However those signal numbers are consistent within statistical uncertainty. Especially largest systematic uncertainty (except for c_i and s_i) come from $B\bar{B}$ backgrounds PDF shape. It is almost caused as a result of miss-particle-identification.

In future next Super-B-Factory era, ϕ_3 measurements with neutral B will be possible. For example, Belle II experiment has planned 50 times large $B\bar{B}$ as Belle's one. And also, particle identification will be improved. It will allow us to distinguish signal and backgrounds more clearly. My study showed large uncertainties come from statistics, $B\bar{B}$ backgrounds and D decay strong phase c_i, s_i. Adding one more assumption of next Super-D-Factory, also uncertainty from c_i, s_i can be decreased.

In summary, this study indicates possibility of ϕ_3 measurement with neutral B in not-so-distant future.

Chapter 6

Conclusion

In summary, we report study of the ratio of amplitude $B^0 \to D^0 K^{*0}$ and $B^0 \to \bar{D}^0 K^{*0}$ r_S, as shown in Fig. 4.10, using 772×10^6 $B\bar{B}$ pairs collected with the Belle detector.

$$r_S \quad < \quad 0.87 \quad \text{(at 68 \% C.L.)}. \tag{6.1}$$

A new model-independent Dalitz analysis method is used to observe $(x_\pm, y_\pm)$ which enable us to avoid the modeling uncertainty on Dalitz plane. This is first r_S measurement on neutral B with model-independent Dalitz analysis.

Appendix A

Details on NeuroBayes Training

This appendix presents the details about the training result. Table A.1 shows the summary table for input variables. The rank in importance for network output (rank), the identification number of the input (node), the name of variable (name), and the preprocessing flag (preprocess) are listed. The preprocessing flags correspond to the explanations below.

- 12: transform to Gaussian with no delta-function
- 14: regularized spline fit with no delta-function
- 15: regularized monotonous spline fit with no delta-function
- 34: regularized spline fit with delta-function

In the following pages, we put important figures related to the training. For the explanations, see the captions.

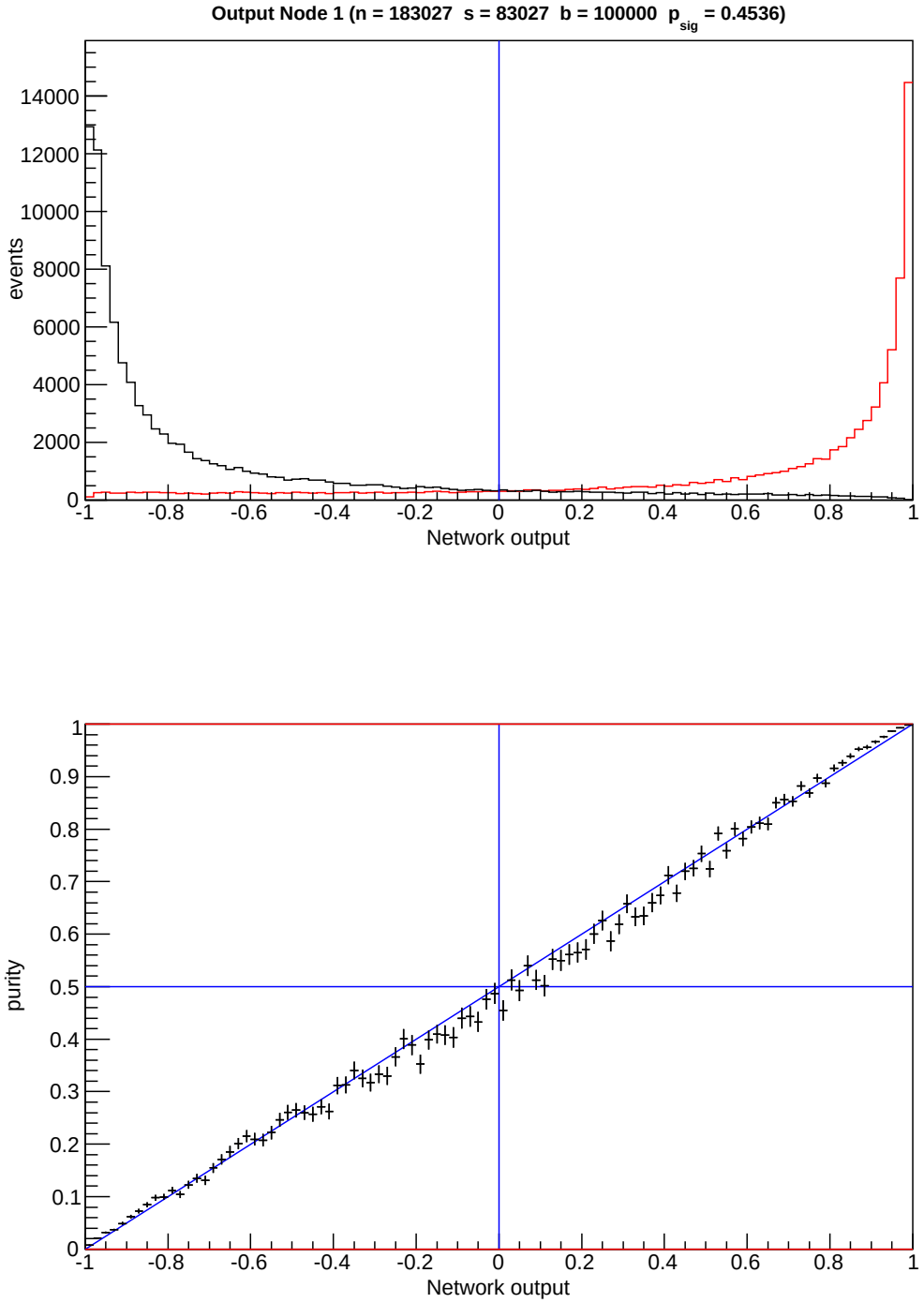

Figure A.1: The distributions of network output for signal MC (red) and for $q\bar{q}$ MC (black) are shown (upper). The purity is plotted over the network output (lower). For both, the figures given behind correspond to the output before the iteration training.

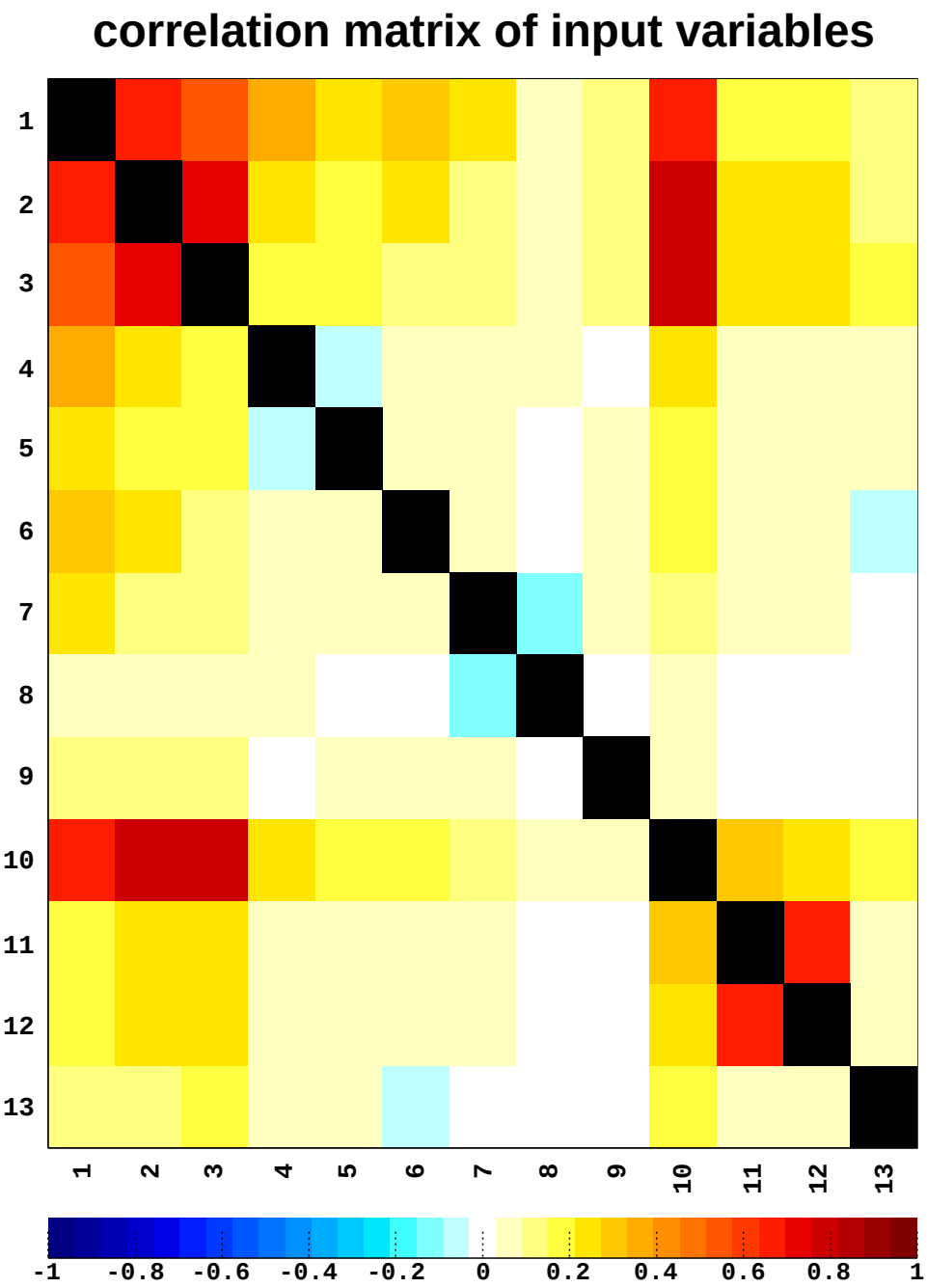

Figure A.2: The correlation matrix of input variables. The column- and row- numbers are the node numbers.

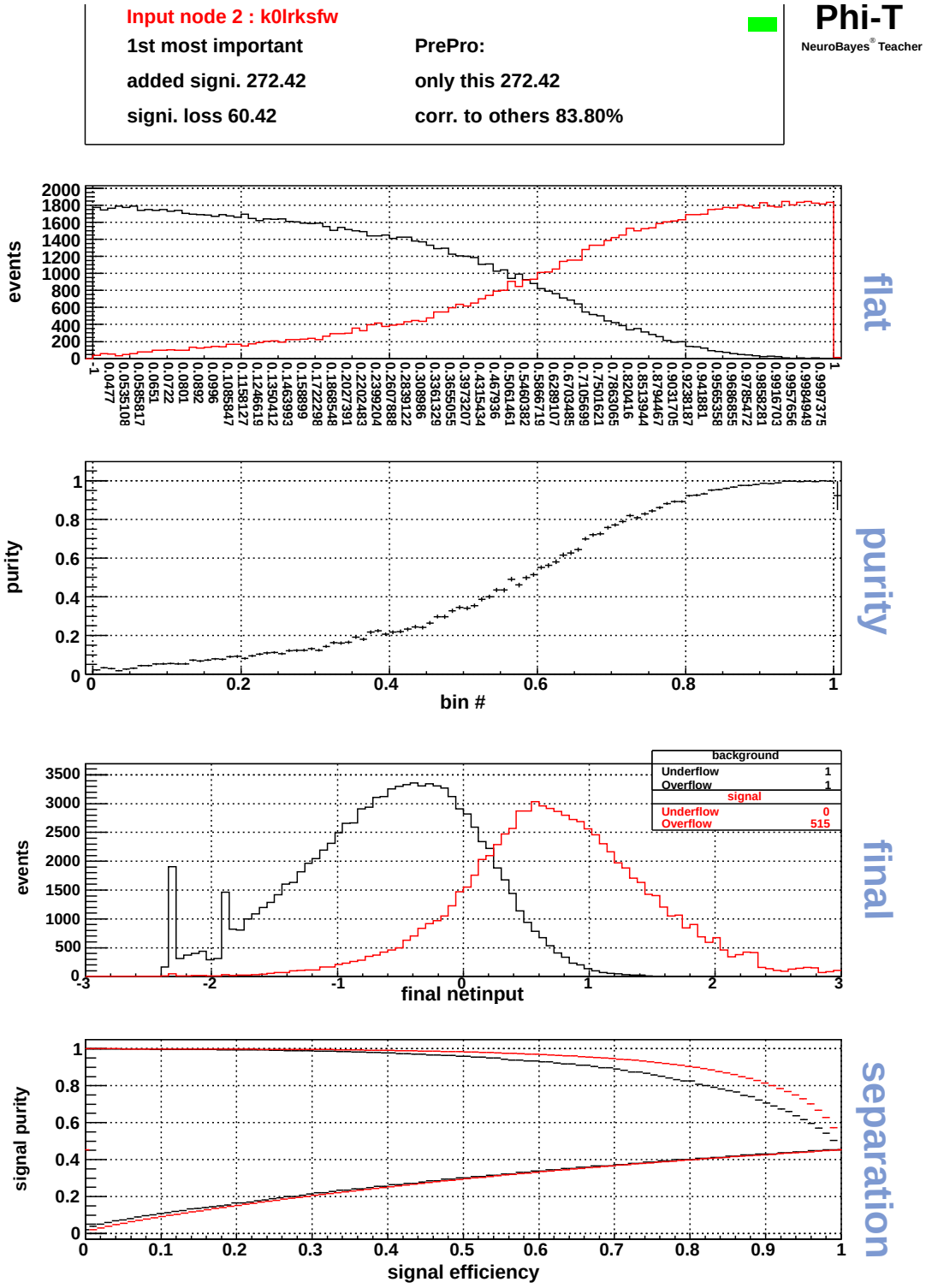

Figure A.3: The equalized distributions for the input variable (1st), the signal purity (2nd), the distributions after the preprocessing (3rd), and the purity curve on the efficiency (4th) for LR(KSFW). In the 1st and 3rd figures, the red corresponds to the signal while the black corresponds to the background. In the 4th figure, the red corresponds to the result after the training using all variables and the black corresponds to the one for single parameter.

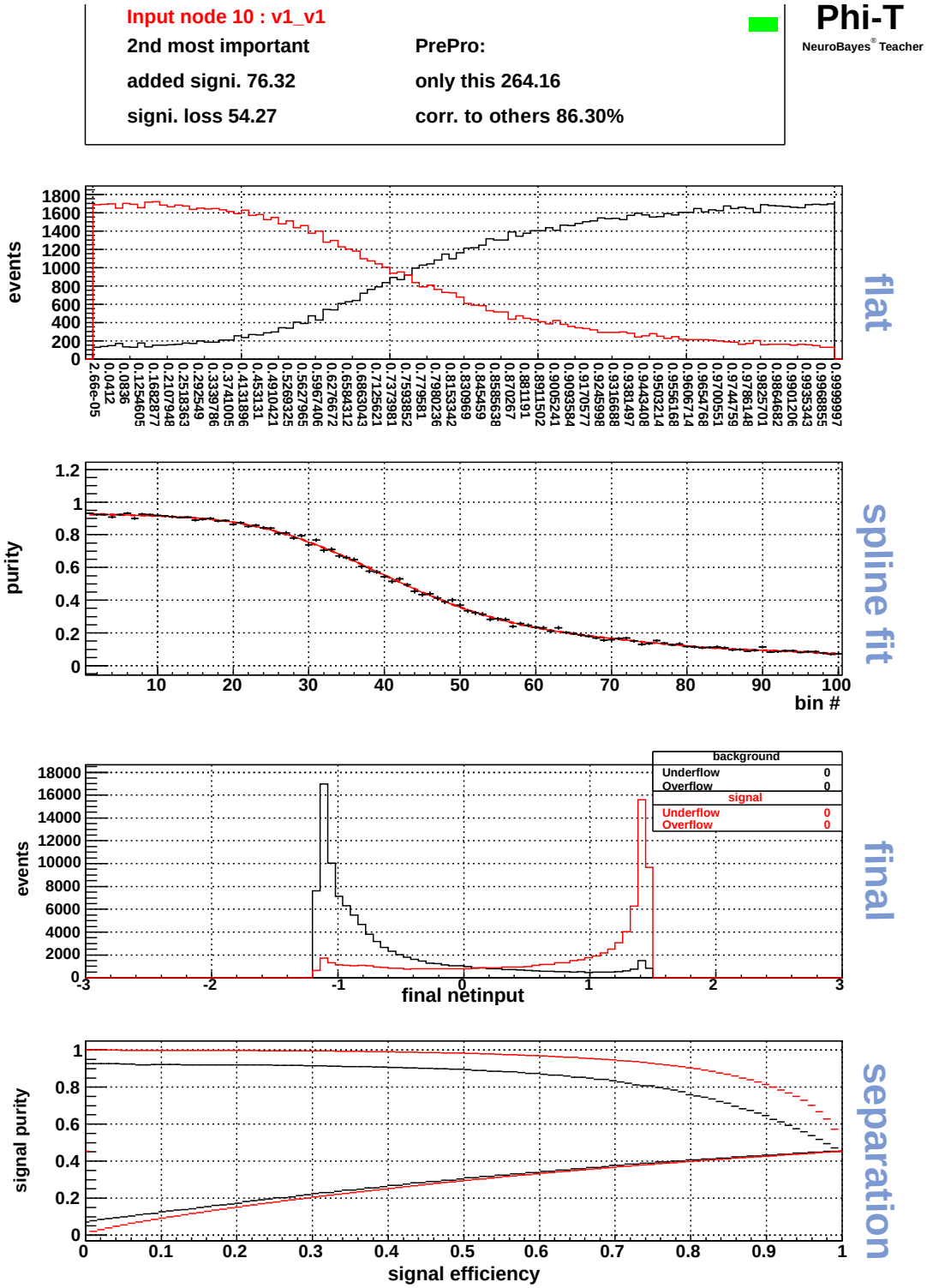

Figure A.4: The equalized distributions for the input variable (1st), the signal purity with a spline fit (2nd), the distributions after the preprocessing (3rd), and the purity curve on the efficiency (4th) for Cosine of $V_{\mathrm{sig},1}$ and $V_{\mathrm{oth.},1}$. In the 1st and 3rd figures, the red corresponds to the signal while the black corresponds to the background. In the 4th figure, the red corresponds to the result after the training using all variables and the black corresponds to the one for single parameter.

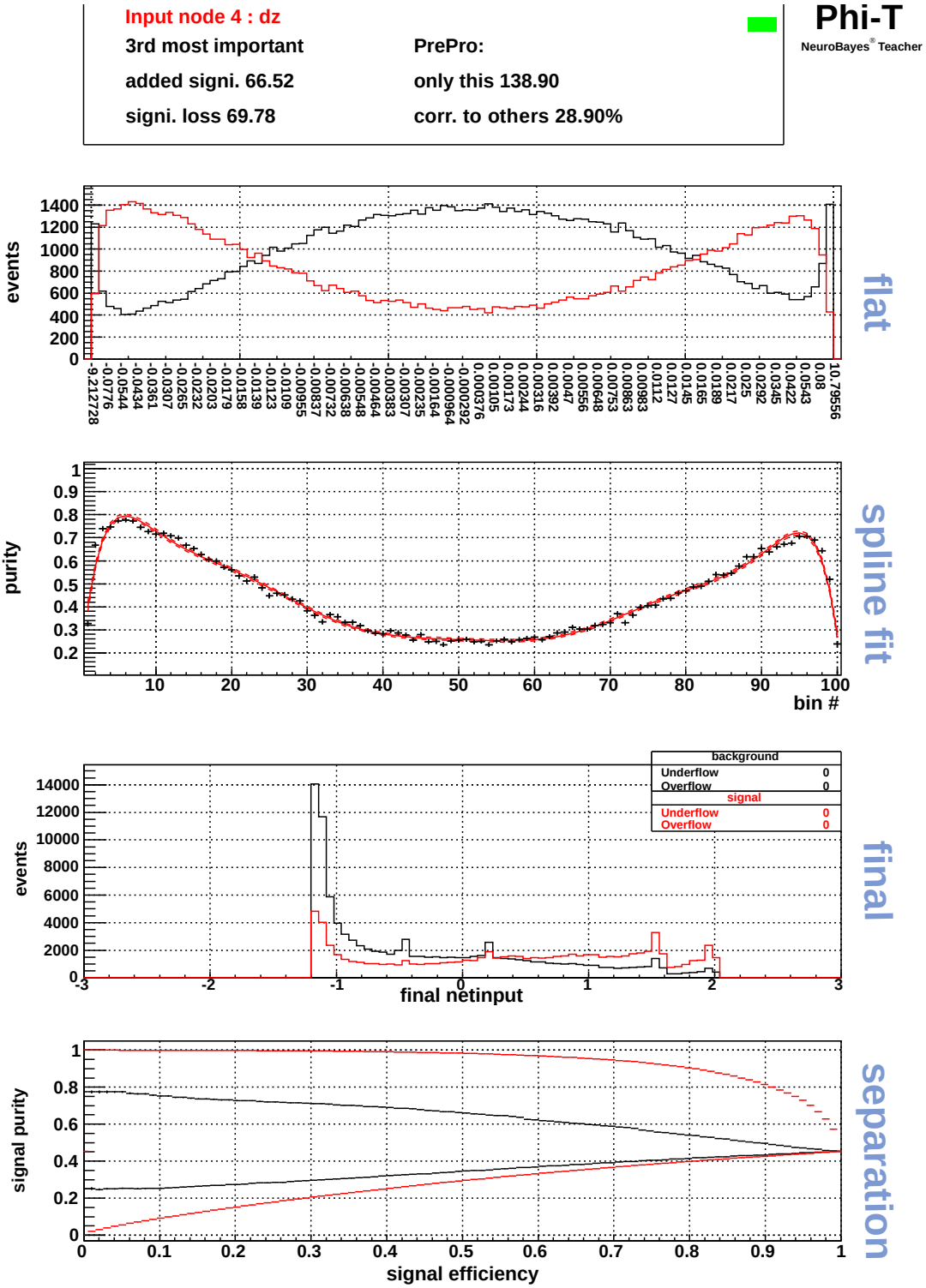

Figure A.5: The equalized distributions for the input variable (1st), the signal purity with a spline fit (2nd), the distributions after the preprocessing (3rd), and the purity curve on the efficiency (4th) for Δz. In the 1st and 3rd figures, the red corresponds to the signal while the black corresponds to the background. In the 4th figure, the red corresponds to the result after the training using all variables and the black corresponds to the one for single parameter. We use a delta-function for the case that the tag-side vertex cannot be obtained.

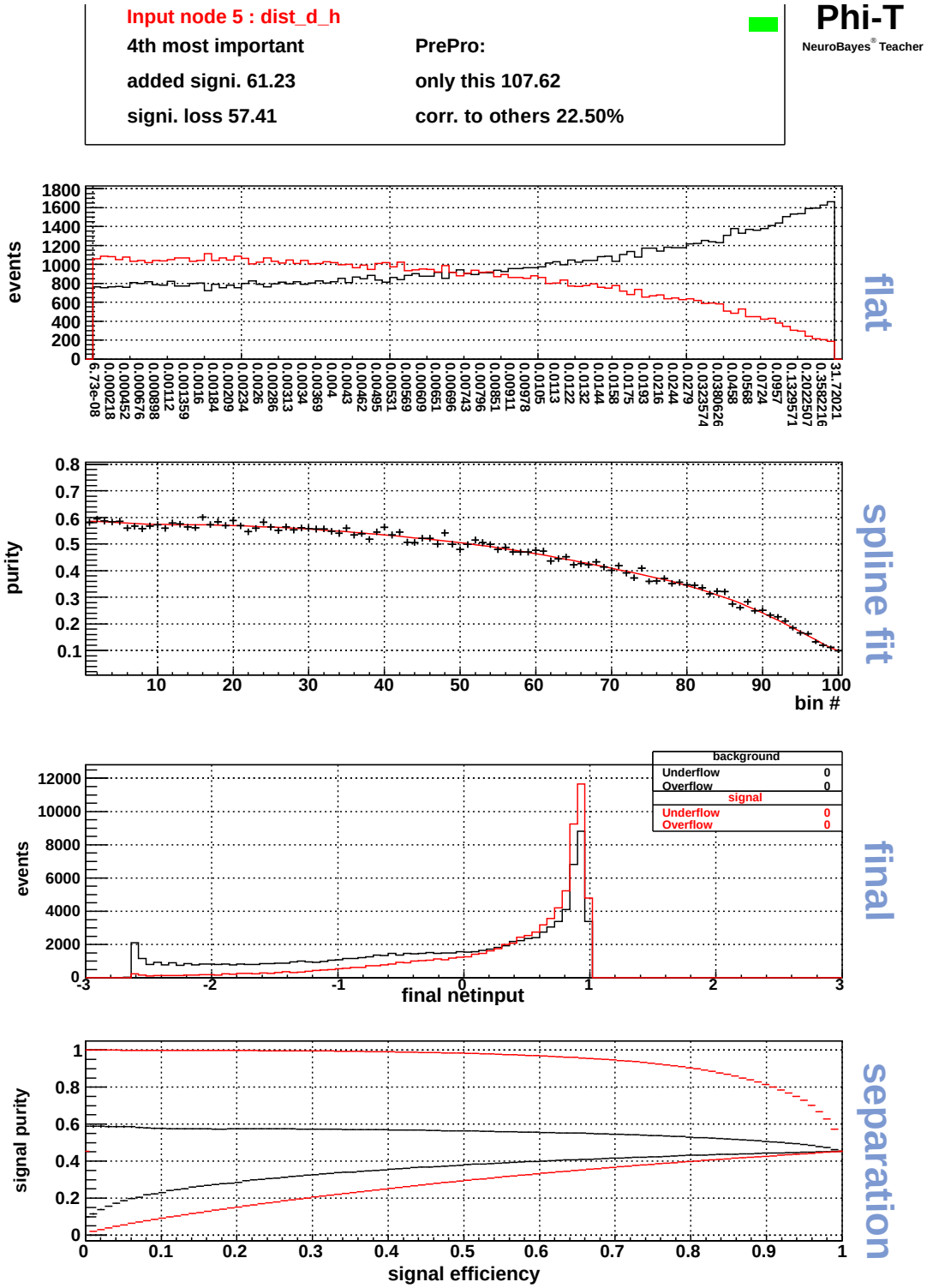

Figure A.6: The equalized distributions for the input variable (1st), the signal purity with a spline fit (2nd), the distributions after the preprocessing (3rd), and the purity curve on the efficiency (4th) for Distance of D and K^{*0}. In the 1st and 3rd figures, the red corresponds to the signal while the black corresponds to the background. In the 4th figure, the red corresponds to the result after the training using all variables and the black corresponds to the one for single parameter.

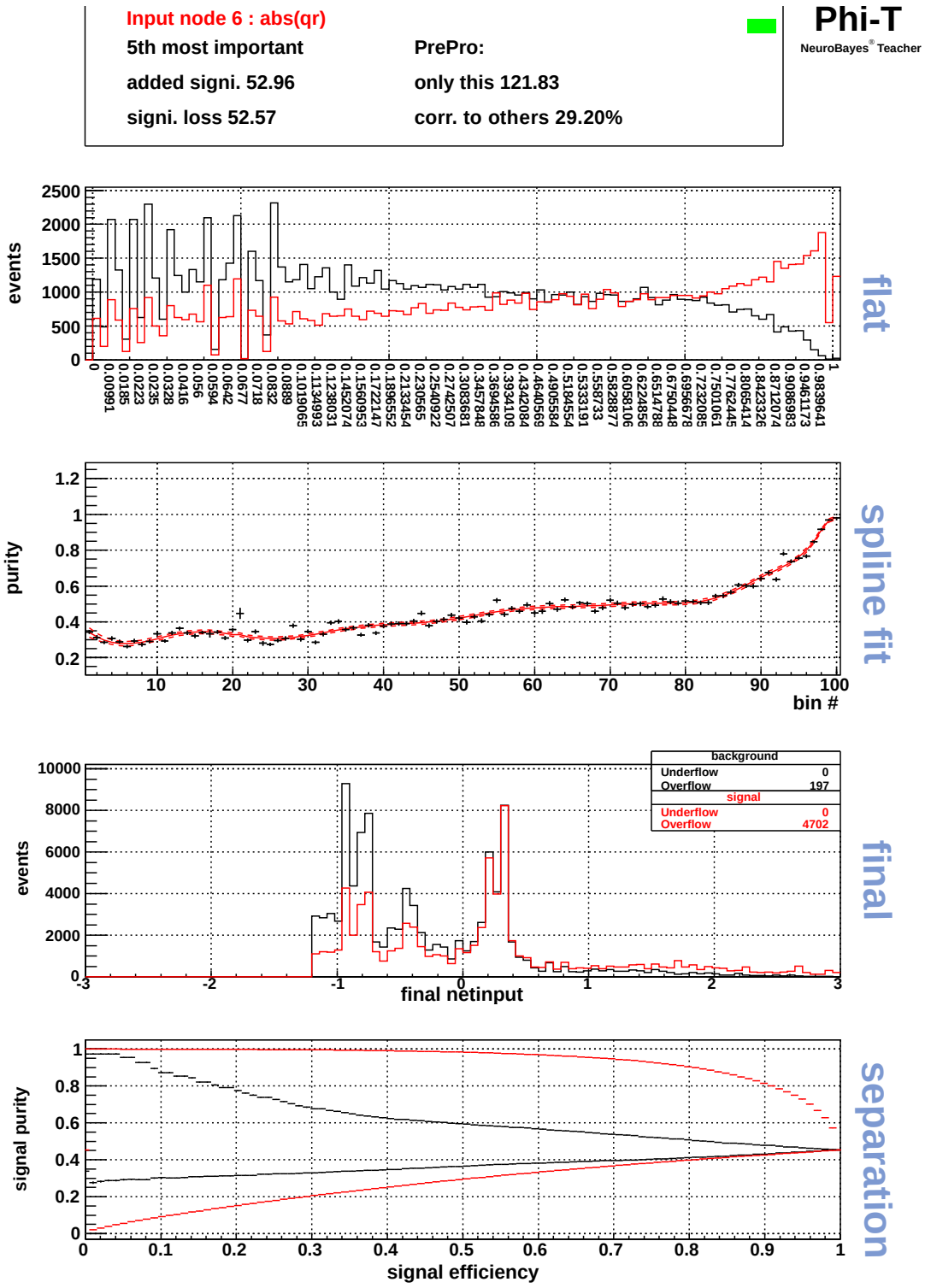

Figure A.7: The equalized distributions for the input variable (1st), the signal purity with a spline fit (2nd), the distributions after the preprocessing (3rd), and the purity curve on the efficiency (4th) for $|qr|$. In the 1st and 3rd figures, the red corresponds to the signal while the black corresponds to the background. In the 4th figure, the red corresponds to the result after the training using all variables and the black corresponds to the one for single parameter.

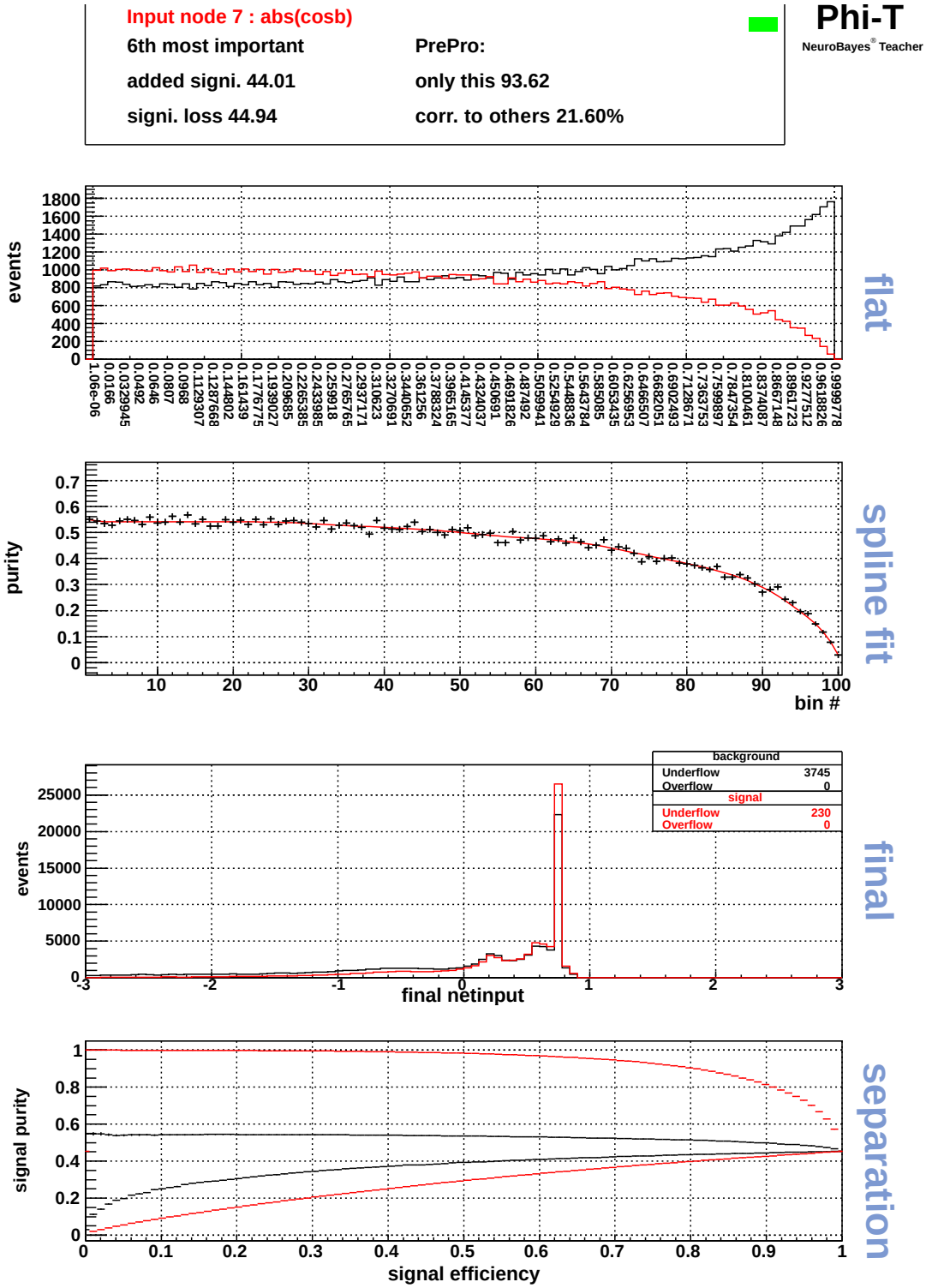

Figure A.8: The equalized distributions for the input variable (1st), the signal purity with a spline fit (2nd), the distributions after the preprocessing (3rd), and the purity curve on the efficiency (4th) for $|\cos\theta_B|$. In the 1st and 3rd figures, the red corresponds to the signal while the black corresponds to the background. In the 4th figure, the red corresponds to the result after the training using all variables and the black corresponds to the one for single parameter.

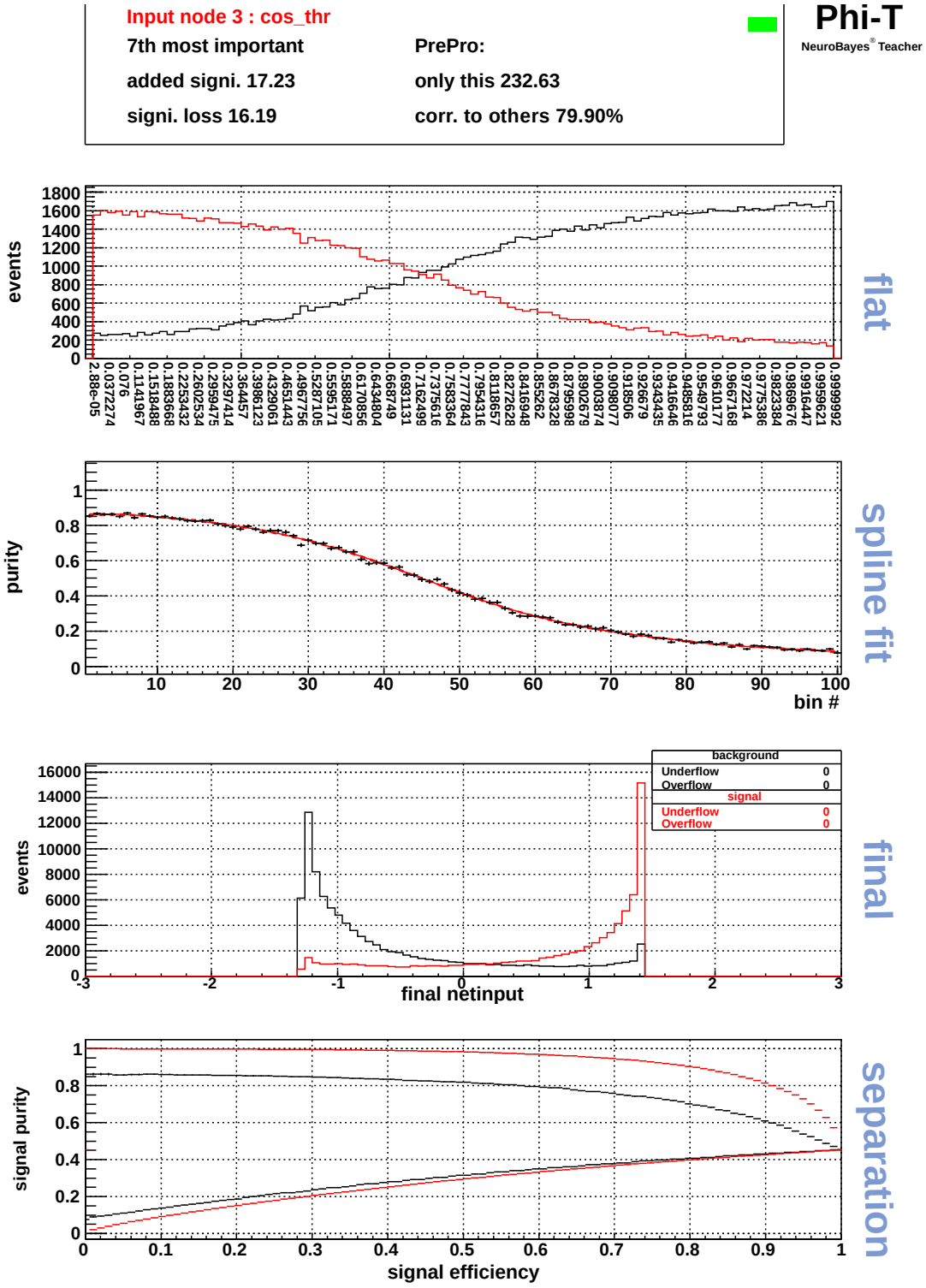

Figure A.9: The equalized distributions for the input variable (1st), the signal purity with a spline fit (2nd), the distributions after the preprocessing (3rd), and the purity curve on the efficiency (4th) for $\cos\theta_{\rm thu}$. In the 1st and 3rd figures, the red corresponds to the signal while the black corresponds to the background. In the 4th figure, the red corresponds to the result after the training using all variables and the black corresponds to the one for single parameter.

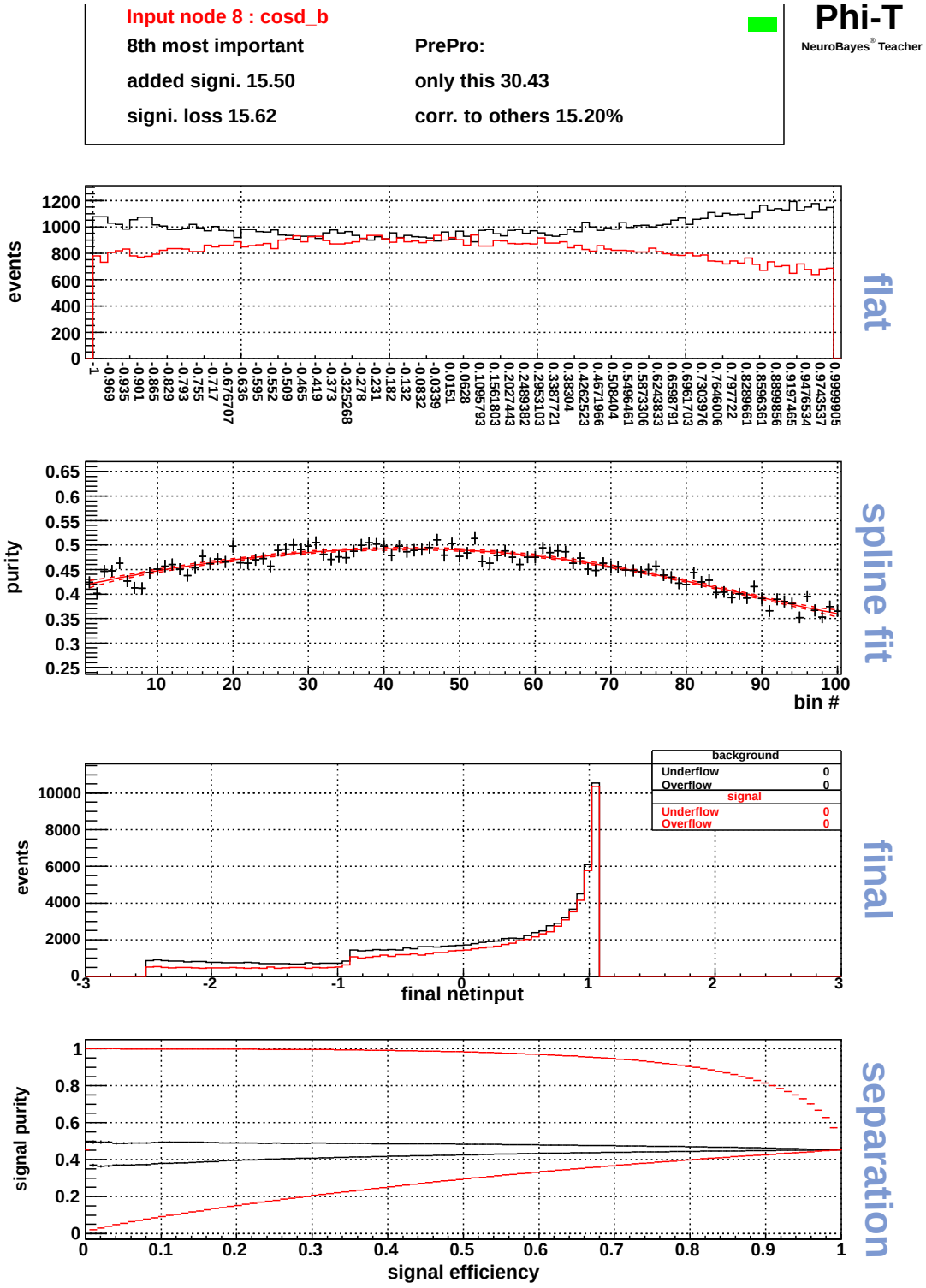

Figure A.10: The equalized distributions for the input variable (1st), the signal purity with a spline fit (2nd), the distributions after the preprocessing (3rd), and the purity curve on the efficiency (4th) for $\cos\theta_B^D$. In the 1st and 3rd figures, the red corresponds to the signal while the black corresponds to the background. In the 4th figure, the red corresponds to the result after the training using all variables and the black corresponds to the one for single parameter.

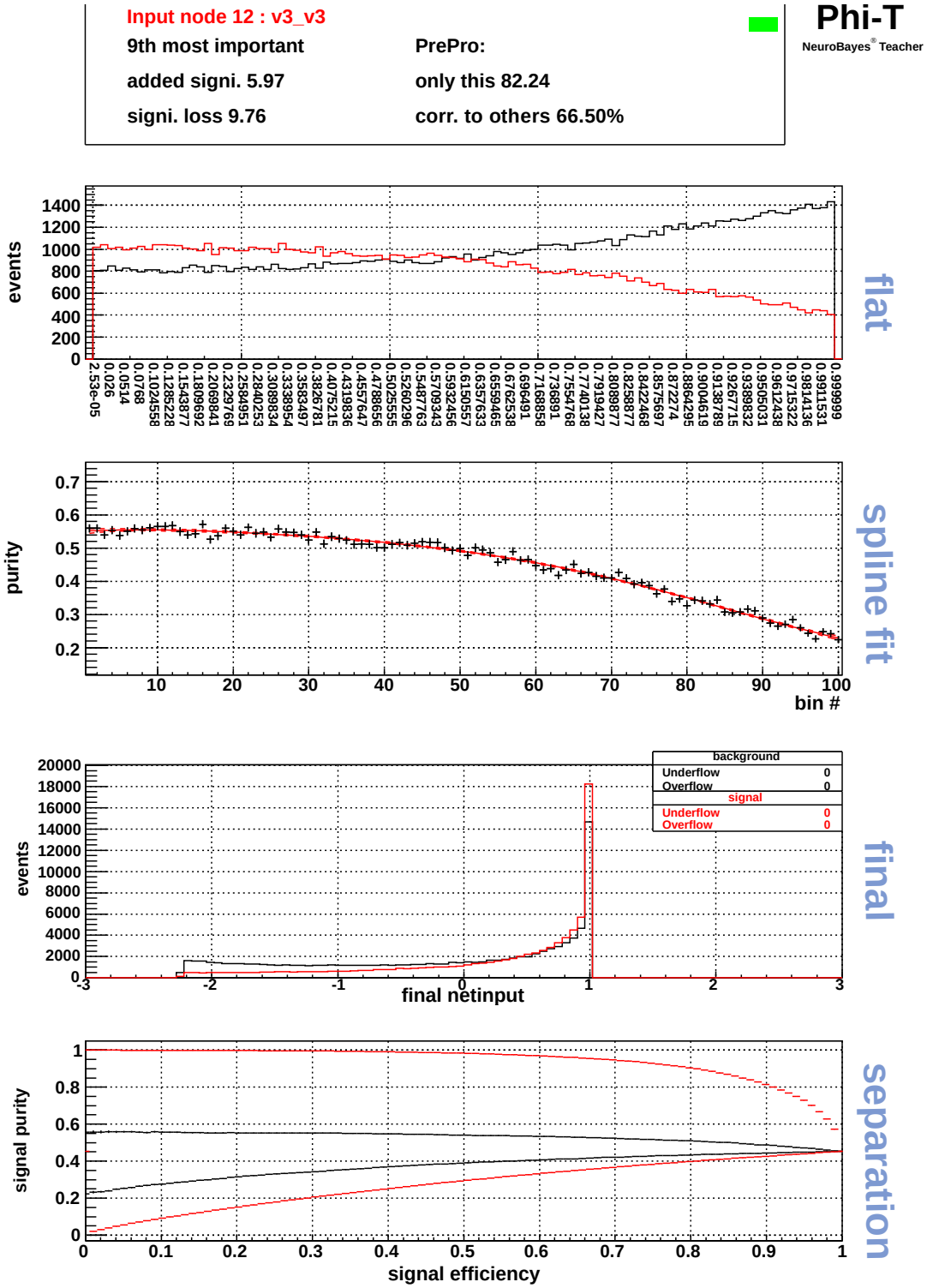

Figure A.11: The equalized distributions for the input variable (1st), the signal purity with a spline fit (2nd), the distributions after the preprocessing (3rd), and the purity curve on the efficiency (4th) for Cosine of $V_{\mathrm{sig},3}$ and $V_{\mathrm{oth.},3}$. In the 1st and 3rd figures, the red corresponds to the signal while the black corresponds to the background. In the 4th figure, the red corresponds to the result after the training using all variables and the black corresponds to the one for single parameter.

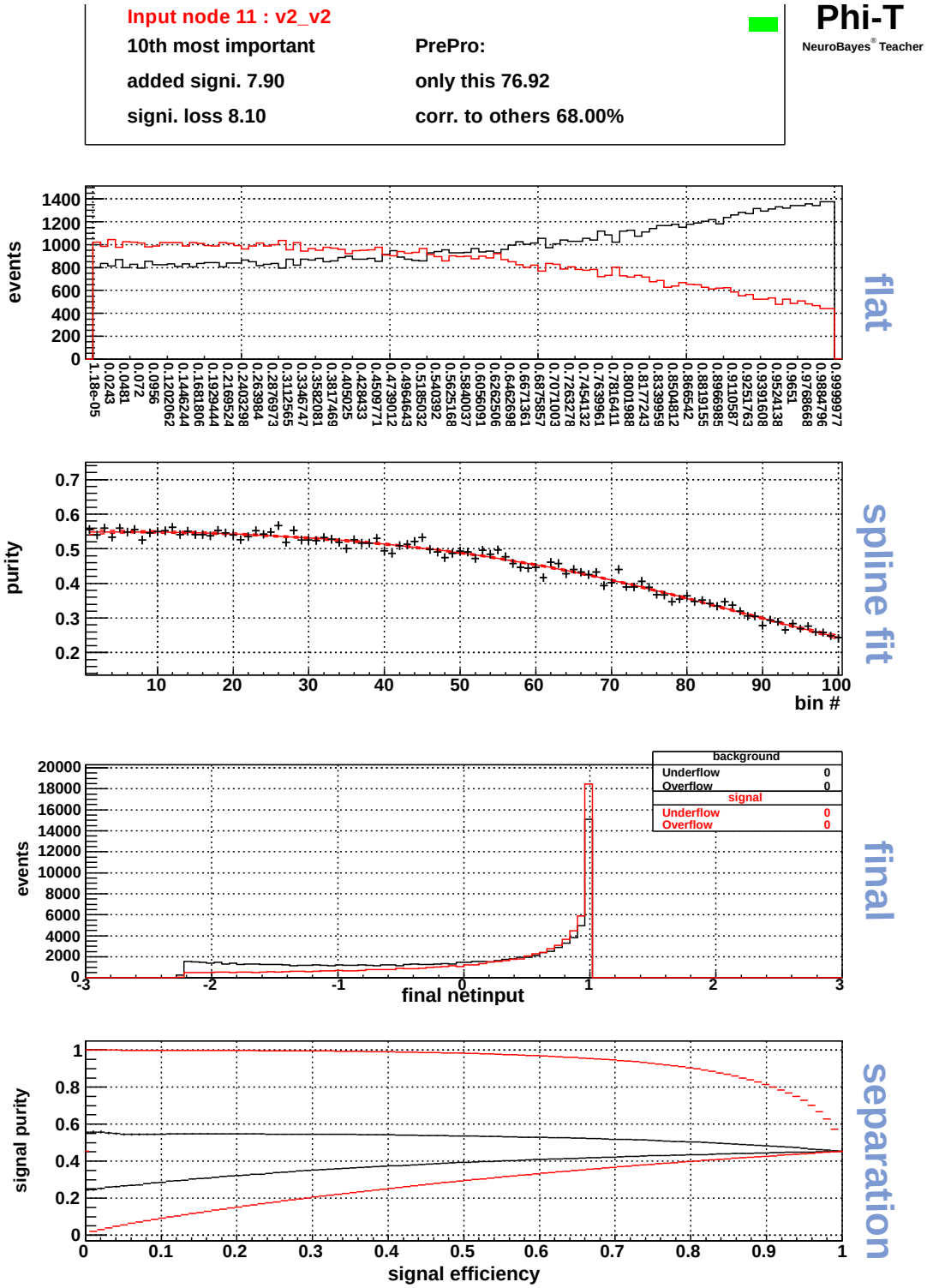

Figure A.12: The equalized distributions for the input variable (1st), the signal purity with a spline fit (2nd), the distributions after the preprocessing (3rd), and the purity curve on the efficiency (4th) for Cosine of $V_{\mathrm{sig},2}$ and $V_{\mathrm{oth.},2}$. In the 1st and 3rd figures, the red corresponds to the signal while the black corresponds to the background. In the 4th figure, the red corresponds to the result after the training using all variables and the black corresponds to the one for single parameter.

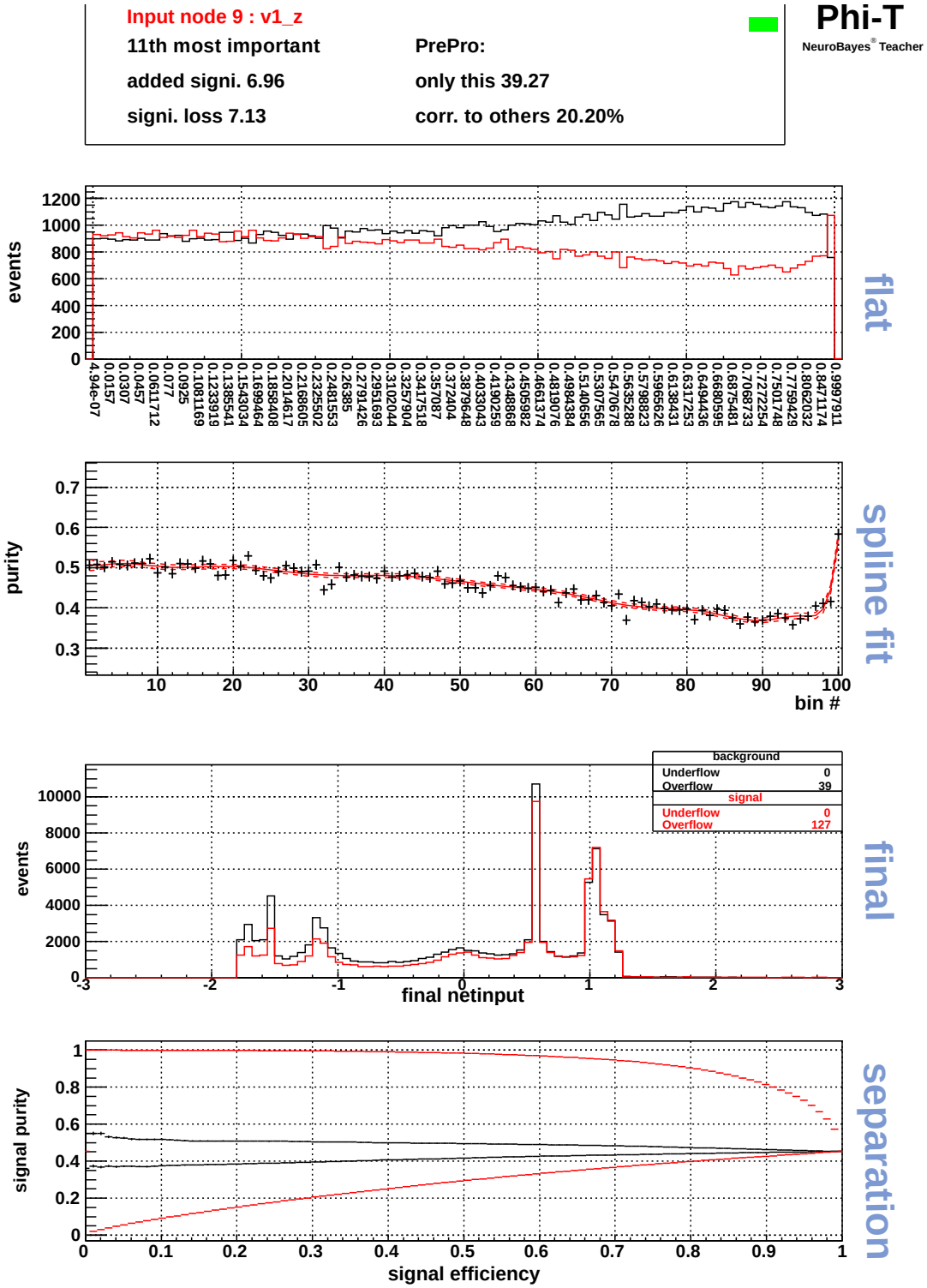

Figure A.13: The equalized distributions for the input variable (1st), the signal purity with a spline fit (2nd), the distributions after the preprocessing (3rd), and the purity curve on the efficiency (4th) for Z of $V_{\mathrm{all},1}$. In the 1st and 3rd figures, the red corresponds to the signal while the black corresponds to the background. In the 4th figure, the red corresponds to the result after the training using all variables and the black corresponds to the one for single parameter.

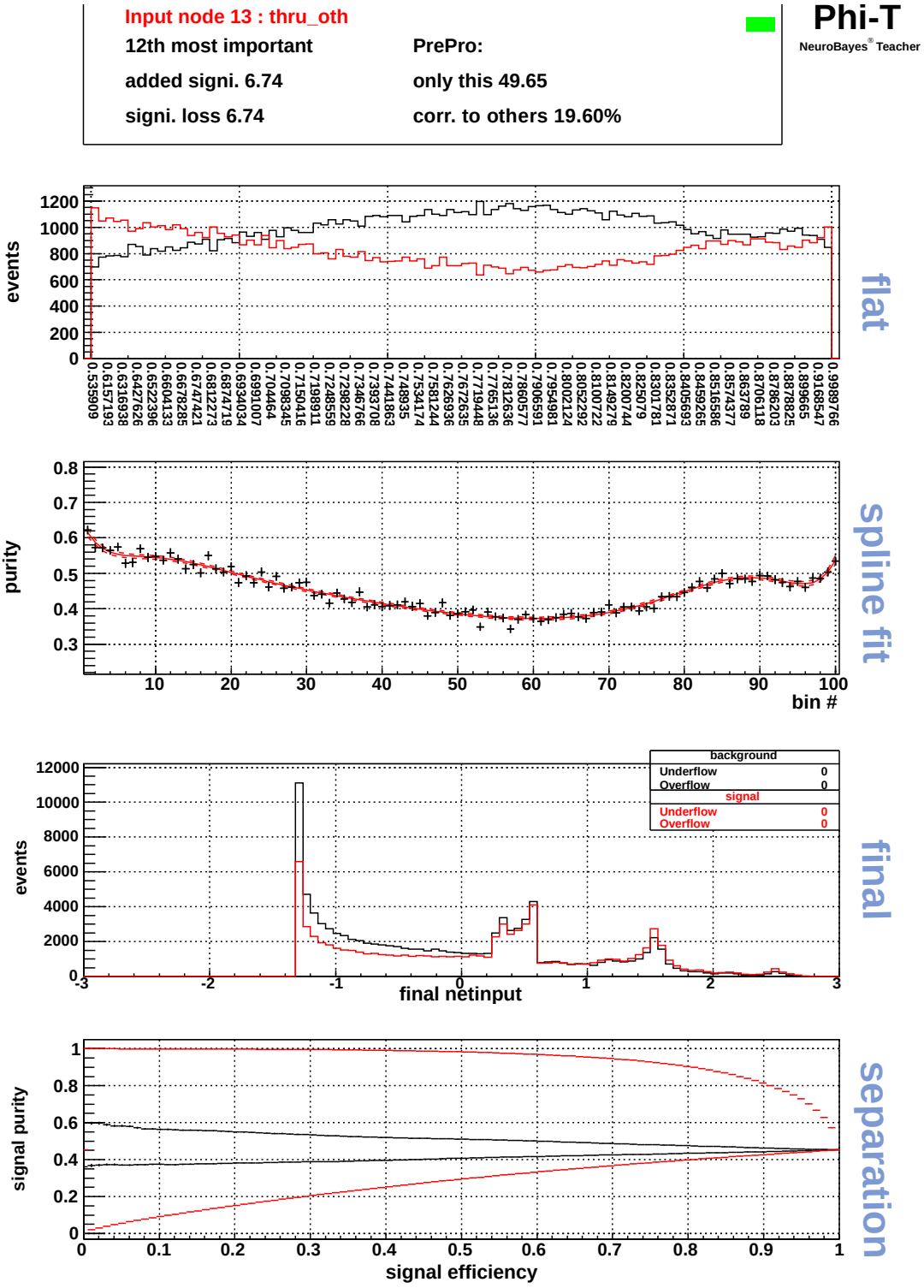

Figure A.14: The equalized distributions for the input variable (1st), the signal purity with a spline fit (2nd), the distributions after the preprocessing (3rd), and the purity curve on the efficiency (4th) for Magnitude of Thrust_oth. In the 1st and 3rd figures, the red corresponds to the signal while the black corresponds to the background. In the 4th figure, the red corresponds to the result after the training using all variables and the black corresponds to the one for single parameter.

rank	node	name	preprocess
1	2	LR(KSFW)	12
2	10	Cosine of $V_{\mathrm{sig},1}$ and $V_{\mathrm{oth.},1}$	14
3	4	Δz	34
4	5	distance of D and K^{*0}	15
5	6	$\lvert qr \rvert$	14
6	7	$\lvert \cos\theta_B \rvert$	15
7	3	$\lvert \cos\theta_{\mathrm{thr}} \rvert$	14
8	8	$\cos\theta_B^D$	14
9	12	Cosine of $V_{\mathrm{sig},3}$ and $V_{\mathrm{oth.},3}$	14
10	11	Cosine of $V_{\mathrm{sig},2}$ and $V_{\mathrm{oth.},2}$	14
11	9	Z of $V_{\mathrm{all},1}$	14
12	13	Magnitude of $\mathrm{Thrust}_{\mathrm{oth.}}$	14

Table A.1: The rank in importance for network output (rank), the identification number of the input (node), the name of variable (name), and the preprocessing flag (preprocess) are listed.

Bibliography

[1] Nicola Cabibbo. Unitary Symmetry and Leptonic Decays. *Phys.Rev.Lett.*, 10:531–533, (1963).

[2] Makoto Kobayashi and Toshihide Maskawa. CP Violation in the Renormalizable Theory of Weak Interaction. *Prog.Theor.Phys.*, 49:652–657, (1973).

[3] Lincoln Wolfenstein. Parametrization of the Kobayashi-Maskawa Matrix. *Phys.Rev.Lett.*, 51:1945, (1983).

[4] J. Charles *et al.* (CKMfitter Collaboration). CP Violation and the CKM Matrix: Assessing the Impact of the Asymmetric B Factories. *Eur. Phys. J. C.*, 41:1, (2005). arXiv:hep-ph/0406184, updated results available at http://ckmfitter.in2p3.fr.

[5] Michael Gronau and David London. How to determine all the angles of the unitarity triangle from $B(d)^0 \to DK(s)$ and $B(s)^0 \to D^0$. *Phys.Lett.*, B253:483–488, (1991).

[6] Michael Gronau and Daniel Wyler. On determining a weak phase from CP asymmetries in charged B decays. *Phys.Lett.*, B265:172–176, (1991).

[7] David Atwood, Isard Dunietz, and Amarjit Soni. Enhanced CP violation with $B \to KD^0$ (anti-D^0) modes and extraction of the CKM angle gamma. *Phys.Rev.Lett.*, 78:3257–3260, (1997).

[8] David Atwood, Isard Dunietz, and Amarjit Soni. Improved methods for observing CP violation in $B^\pm \to DK$ and measuring the CKM phase gamma. *Phys.Rev.*, D63:036005, (2001).

[9] A. Soffer A. Giri, Y. Grossman and J. Zupan. Determining γ using $B^\pm \to DK^\pm$ with multibody D decay. *Phys. Rev. D*, 68:054018, (2003).

[10] A. Bondar. Proceedings of BINP Special Analysis Meeting on Dalitz Analysis. 24-26 Sep. (2002). unpublished.

[11] K. Abe *et al.* (Belle Collaboration). Measurement of $D^0 - \bar{D}^0$ Mixing Parameters in $D^0 \to K_S\pi^+\pi^-$ Decays. *Phys. Rev. Lett.*, 99:131803, (2007).

[12] P. del Amo Sanchez *et al.* (The BaBar Collaboration). Measurement of D^0-antiD^0 mixing parameters using $D^0 \to K^0_S\pi^+\pi^-$ and $D^0 \to K^0_S K^+K^-$ decays. *Phys. Rev. Lett.*, 105:081803, (2010).

[13] P. Krokovny A. Bondar, T. Gershon. A Method to Measure ϕ_1 Using $\bar{B}^0 \to Dh^0$ With Multibody D Decay. *Phys. Lett. B.*, 624:1–10, (2005).

[14] P. Krokovny *et al.* (Belle Collaboration). Measurement of the quark mixing parameter $\cos(2\phi_1)$ using time-dependent Dalitz analysis of anti-$B^0 \to D[K^0_S\pi^+\pi^-]h^0$. *Phys. Rev. Lett.*, 97:081801, (2006).

[15] K. Abe *et al.* (Belle Collaboration). Updated Measurement of ϕ_3 with a Dalitz Plot Analysis of $B \to D^{(*)}K$ Decay. In *43rd Rencontres de Moriond on QCD and High Energy Interactions*, (2008). arXiv:hep-ex/0803.3375.

[16] B. Aubert *et al.* (BABAR Collaboration). Improved measurement of the CKM angle gamma in $B^\mp \to D^{(*)}K^{(*)\mp}$ decays with a Dalitz plot analysis of D decays to $K^0_S\pi^+\pi^-$ and $K^0_SK^+K^-$. *Phys. Rev. D.*, 78:034023, (2008).

[17] R. A. Briere *et al.* (CLEO Collaboration). First model-independent determination of the relative strong phase between D^0 and anti-$D^0 \to K^0_S\pi^+\pi^-$ and its impact on the CKM Angle γ/ϕ_3 measurement. *Phys. Rev. D.*, 80:032002, (2009).

[18] A. Bondar and A. Poluektov. Feasibility study of model-independent approach to ϕ_3 measurement using Dalitz plot analysis. *Eur. Phys. J. C.*, 47:347, (2006).

[19] M. Gronau. Improving bounds on γ in $B^\pm \to DK^\pm$ and $B^{\pm,0} \to DX^{\pm,0}_s$. *Phys. Lett. B.*, 557:198, (2003).

[20] *et al.* (UTfit Collaboration) M. Bona. The 2004 UTfit collaboration report on the status of the unitarity triangle in the standard model. *J. High Energy Phys.*, 0507:028, (2005). arXiv:hep-ph/0501199, updated results available at http://www.utfit.org/.

[21] B. Aubert *et al.* (BaBar Collaboration). Measurement of $\bar{B}^0 \to D^{(*)0}K^{(*)0}$ branching fractions. *Phys. Rev. D.*, 74:031101, (2006).

[22] G. Cavoto *et al.* Angles from B Decays with Charm. *Proceedings of the CKM 2005 Workshop (WG5)*, (2005).

[23] Kurokawa, S. Overview of the KEKB accelerators. *Nucl.Instrum.Meth.A*, 499:1–7, (2003).

[24] A. Abashian, K. Gotow, N. Morgan, L. Piilonen, S. Schrenk, et al. The Belle Detector. *Nucl.Instrum.Meth.*, A479:117–232, (2002).

[25] G. Alimonti, *et al.* (Belle Collaboration). The BELLE silicon vertex detector. *Nucl. Instr. Meth. A*, 453:71, (2000).

[26] Y. Ushiroda, *et al.* (Belle Collaboration). BELLE silicon vertex detector. *Nucl. Instr. Meth. A*, 551:6, (2003).

[27] H. Hirano, M. Akatsu, Y. Fujita, K. Fujimoto, M. Hirose, et al. A high resolution cylindrical drift chamber for the KEK B factory. *Nucl.Instrum.Meth.*, A455:294–304, (2000).

[28] T. Iijima, I. Adachi, R. Enomoto, R. Suda, T. Sumiyoshi, et al. Aerogel Cherenkov counter for the BELLE detector. *Nucl.Instrum.Meth.*, A453:321–325, (2000).

[29] H. Kichimi, Y. Yoshimura, T. Browder, B. Casey, M. Jones, et al. The BELLE TOF system. *Nucl.Instrum.Meth.*, A453:315–320, (2000).

[30] H. Ikeda et al. A detailed test of the CsI(Tl) calorimeter for BELLE with photon beams of energy between 20-MeV and 5.4-GeV. *Nucl.Instrum.Meth.*, A441:401–426, (2000).

[31] A. Abashian et al. The K_L/μ detector subsystem for the BELLE experiment at the KEK B factory. *Nucl.Instrum.Meth.*, A449:112–124, (2000).

[32] R. Akhmetshin et al. Survey of the properties of BGO crystals for the extreme forward calorimeter at BELLE. *Nucl.Instrum.Meth.*, A455:324–328, (2000).

[33] Y. Ushiroda et al. Development of the central trigger system for the BELLE detector at the KEK B factory. *Nucl.Instrum.Meth.*, A438:460–471, (1999).

[34] Asish Satpathy. Particle identification with BELLE. (1999).

[35] E. Nakano. Belle PID. *Nucl.Instrum.Meth.*, A494:402–408, (2002).

[36] S. Pruvot, M.H. Schune, V. Sordini, and A. Stocchi. Measuring gamma with $B^0 \to D^0 K^{*0}$ decays at BaBar. (2007).

[37] G. C. Fox and S. Wolfram. Observables for the Analysis of Event Shapes in e^+e^- Annihilation and Other Processes. *Phys. Rev. Lett.*, 41:1581, (1978).

[38] H. Kakuno et al. Neutral B Flavor Tagging for the Measurement of Mixing-induced CP Violation at Belle. arXiv:hep-ex/0403022v1, (2004).

[39] M. Feindt and U. Kerzel. The NeuroBayes neural network package. *Nucl.Instrum.Meth.*, A559:190–194, (2006).

[40] Kyle S. Cranmer. Kernel estimation in high-energy physics. *Comput.Phys.Commun.*, 136:198–207, 2001.

[41] B. Aubert. Branching Fractions and CP-Violating Asymmetries in Radiative B Decays to eta K gamma. *Phys. Rev. D*, 79:01102, (2009).